

Search for dark matter annual modulation  
in XMASS-I detector

Keishi HOSOKAWA  
Kobe University Department of Physics

January 12<sup>th</sup>, 2016

# Abstract

In modern physics, Dark Matter is one of the most important problems. Dark matter is expected to be new particle(s) beyond the standard model and be closely related to the large-scale structure of our universe. One of strong candidates of dark matter is Weakly Interacting Massive Particle(WIMP). The revolution of the Earth around the Sun causes annual modulation in the recoil energy spectrum of dark matter. This phenomenon is a characteristic of the dark matter signal. So far DAMA/LIBRA and some other experiments claim to have observed the annual modulation in their observed data, but other more sensitive experiments do not. More experiments to verify DAMA/LIBRA result are strongly required. The XMASS-I experiment is a direct dark matter search experiment in Kamioka underground observatory in Japan. A search for dark matter by means of the annual modulation was conducted using liquid xenon detector XMASS-I. For analysis, observed data between November 2013 and March 2015 were used. The first energy calibration below 5.9 keV in XMASS-I detector was conducted using 1.5 (1.8) escape peak of 4.1 (4.4) keV characteristic X-ray in  $^{55}\text{Fe}$  calibration. After simple event selections, model independent and model dependent analyses were conducted. In the model independent analysis, only interaction via electronic recoil was assumed. The result showed a weak negative modulation effect, but this result could be explained by a fluctuation of the background since the p-value was 17.7 %. In the model dependent case, the WIMP dark matter model was assumed. The greater part of the allowed region by DAMA/LIBRA was excluded from this modulation analysis.

# Contents

<b>1</b>	<b>Introduction</b>	<b>3</b>
<b>2</b>	<b>WIMP dark matter searches</b>	<b>6</b>
2.1	Direct search experiments . . . . .	7
2.1.1	Cryogenic detectors . . . . .	7
2.1.2	Solid scintillator detectors . . . . .	8
2.1.3	Liquid noble gas detectors . . . . .	8
2.1.4	Directional detectors . . . . .	8
2.2	Indirect search experiments . . . . .	8
2.3	Collider searches . . . . .	8
2.4	Annual modulation . . . . .	9
2.5	Expected WIMP spectrum . . . . .	9
2.6	Current status of WIMP dark matter searches . . . . .	9
<b>3</b>	<b>XMASS experiment</b>	<b>14</b>
3.1	XMASS-I detector . . . . .	14
3.1.1	Xenon circulation system . . . . .	16
3.1.2	Data acquisition system . . . . .	16
3.2	Detector simulation . . . . .	17
3.3	Xenon . . . . .	19
3.3.1	Isotopes of xenon . . . . .	22
3.3.2	Optical characteristics of liquid xenon . . . . .	23
3.3.3	Scintillation mechanism of xenon . . . . .	23
3.4	Environmental backgrounds . . . . .	26
3.4.1	Background from outside of Xe . . . . .	26
3.4.2	Background from inside of Xe . . . . .	28
3.5	Background from ID surface . . . . .	30
<b>4</b>	<b>Calibration</b>	<b>33</b>
4.1	LED calibration . . . . .	33
4.2	Inner calibration system . . . . .	33
4.3	Energy calibration . . . . .	33
4.3.1	Non-linearity of energy scale . . . . .	33
4.3.2	5.9 keV . . . . .	34
4.3.3	1.5 and 1.8 keV . . . . .	35
4.4	Energy scale . . . . .	39
4.4.1	keV <sub>57Co</sub> . . . . .	39

4.4.2	keV <sub>ee</sub> . . . . .	39
4.5	Development of a low-energy X-ray source . . . . .	41
4.6	Xe absorption length . . . . .	43
<b>5</b>	<b>Dataset and event selection</b>	<b>44</b>
5.1	Dataset . . . . .	44
5.2	WIMP signal simulation . . . . .	44
5.3	Event selection . . . . .	45
<b>6</b>	<b>Systematic uncertainties</b>	<b>58</b>
6.1	P.E. yield change . . . . .	58
6.2	Uncertainty of energy scale . . . . .	58
6.3	FADC self calibration . . . . .	61
6.4	Livetime calculation . . . . .	61
6.5	External parameters . . . . .	61
6.6	Background . . . . .	61
6.6.1	Cosmic-ray muon . . . . .	61
6.6.2	Rn in water . . . . .	62
6.6.3	Rn in LXe . . . . .	62
6.7	Other systematic errors . . . . .	63
<b>7</b>	<b>Result</b>	<b>65</b>
7.1	Definition of $\chi^2$ . . . . .	65
7.2	Model-independent modulation search . . . . .	66
7.2.1	Dummy samples . . . . .	66
7.2.2	Result . . . . .	71
7.2.3	p-value . . . . .	71
7.3	WIMP model dependent search . . . . .	81
<b>8</b>	<b>Discussion</b>	<b>83</b>
8.1	WIMP search result . . . . .	83
8.2	Model independent result . . . . .	84
8.3	Summary and future prospects . . . . .	85

# Chapter 1

## Introduction

There is a standard model in particle physics. The Standard Model(SM) had been established in 1970's. It consist of Quantum ChromoDynamics(QCD) and electro-weak theory [1]. SM can explain almost all the phenomena of elementary particles which are observed up to now. SM classify elementary particles into fermions and bosons. Fermions compose materials. Bosons mediate the force between particles except for higgs boson. Figure 1.1 introduces elementary particles in SM. All elementary particles which are predicted by SM had been discovered. Higgs boson discovered by ATLAS[2] and CMS[3] experiments was the last one.

Many experiments are conducted to study phenomena or new particles beyond SM. A few of such phenomena are observed. The representative one is existence of neutrino mass which is described to be zero in SM. However neutrino oscillation which can not occur without a finite neutrino mass had been observed experimentally [4]. This result was broadly recognized and received the Nobel Prize in Physics in 2015.

	Fermion	Boson
Quark	u    c    t	higgs
	d    s    b	photon
Lepton	e $\mu$ $\tau$	gluon
	$\nu_e$ $\nu_\mu$ $\nu_\tau$	W, Z

Figure 1.1: Elementary particles in Standard Model.

Dark matter would be a strong evidence of "beyond Standard Model" to follow neutrino oscillation. There are many indirect evidences of the existence of dark matter. Examples are "Rotation curves of spiral galaxies", "Bullet cluster", "Galactic

lensing effect” and so on. Dark matter is expected to be closely related to the large-scale structure of our universe. Dark matter also expected to be new particle(s) beyond SM, so dark matter detection will have a great impact on astro physics and particle physics. There are some candidates of particle dark matter as follows.

- Neutrino

Neutrino is a candidate of relativistic hot dark matter (HDM) particles. In SM, their masses are zero. Existence of their masses had been proved by observations of neutrino oscillation. They might be a source of missing mass in the Universe. However, their masses are too small ( $< 2$  eV [5]) to explain dark matter problems. Moreover, non-relativistic cold dark matter(CDM) is required to construct large-scale structure of the Universe [6]. They are no longer a strong candidate of dark matter and main component of missing mass in the Universe.

- Axion

Axion [7] is a hypothetical particle and had been proposed to resolve the strong CP problem of QCD. Axion is an undiscovered particle and is expected to be very light ( $\mu\text{eV} \sim \text{some eV}$ ). Although their mass is light, they can be CDM since they were produced non-thermally. If it exists, it could be a candidate of CDM.

- WIMP

Weakly Interacting Massive Particle(WIMP) is the most strong candidate of CDM. WIMP(s) is expected to be an undiscovered particle(s) with high mass roughly between 1 GeV and a few TeV. Neutralino in Super-symmetric theory (SUSY) is an example of WIMP [8]. They have neutral charge and are stable relative to age of the Universe. They are expected to interact nucleon of ordinary matters with cross section of approximately weak strength.

Assuming WIMP’s property to interact with nucleon, dark matter searches had been conducted. However, dark matter is not discovered, so far. There are some CDM models in which dark matter particles interact with electrons. Axion is one of such CDM candidates. In addition to axion, bosonic super-WIMP[9], mirror matter[10], axion like particles and so on are expected to interact with electrons, and there may be WIMP–electron interaction. Both searches for not only nuclear recoil but also electron recoil are required.

In this thesis, searches for dark matter annual modulation in XMASS–I dataset were conducted. In Chapter 2, the WIMP dark matter search situation in the world is introduced, and annual modulation of dark matter is explained. In Chapter 3, XMASS project and XMASS–I detector system are explained. In Chapter 4, calibration system for XMASS–I and energy calibration results are described. The results from  $^{55}\text{Fe}$  calibration are used for the model independent modulation analysis. In Chapter 5, observed dataset in XMASS–I detector and event selections are described. In Chapter 6, systematic error sources for modulation analysis are introduced. In Chapter 7, modulation analysis methods and the results are described. Model independent and WIMP model dependent analyses were conducted.

In Chapter 8, the results from this study are compared with other experiments' results.

## Chapter 2

### WIMP dark matter searches

There are three experimental methods to search WIMP dark matter. The three search methods are direct search, indirect search and collider experiment. Figure 2.1 shows a diagram of WIMP–ordinary matter interaction. X and N represent WIMP particle and ordinary matter (SM particle), respectively. Direct search experiments look for their scattering. Indirect search experiments look for secondary particles generated by dark matter pair annihilation. Collider experiments are trying to produce WIMP by a collision among SM particles in very high energy.

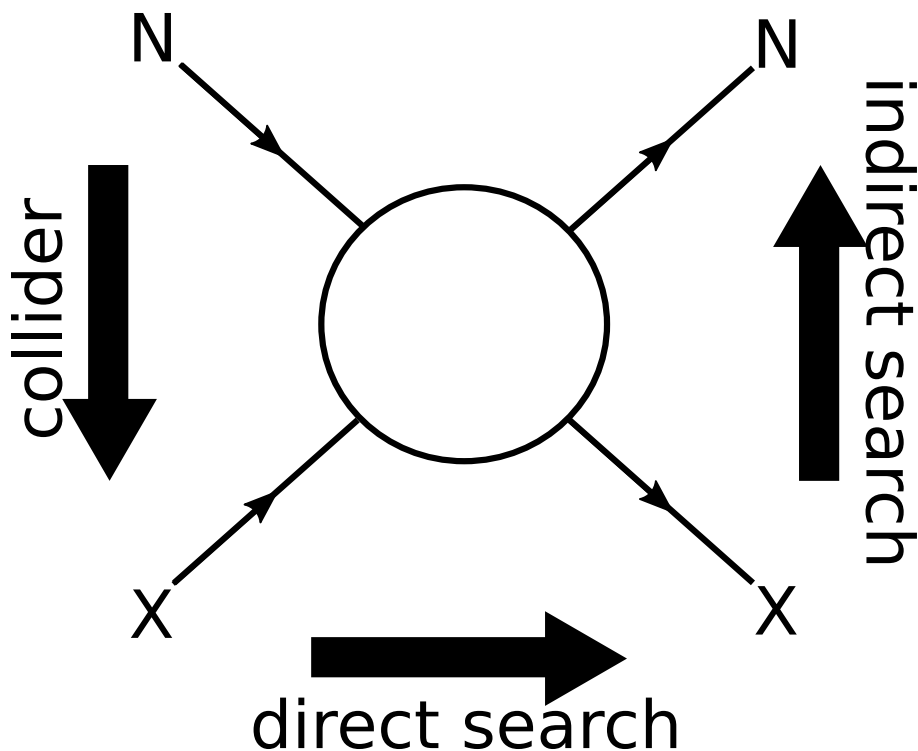


Figure 2.1: Three experimental methods to search WIMP dark matter.

## 2.1 Direct search experiments

There are three kinds of signals from WIMP–ordinary matter scattering. They are scintillation light, ionization and heat. Figure 2.2 shows a schematic view of the current ways to detect the reactions. There are experiments using two types of the signals. For example, LUX experiment uses scintillation light and ionized electron signals. Such experiments discriminate between nuclear recoil and gamma (electron recoil) events. Assuming that signals are nuclear recoils, they can reject gamma and electron events as background(BG). On the other hand, XMASS experiment, which detects only scintillation light, can achieve the highest scintillation light yield from liquid xenon in the world and has scalability by its simple geometry. Both of them have good points and bad points.

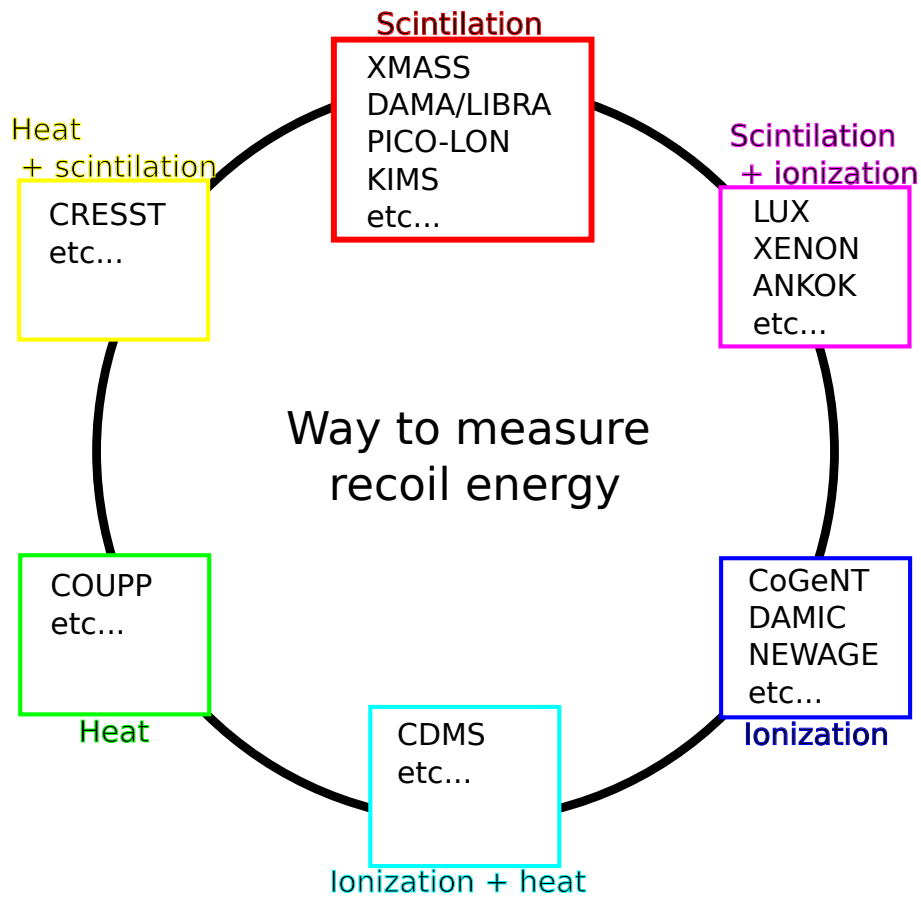


Figure 2.2: Experimental signals for direct dark matter detection.

### 2.1.1 Cryogenic detectors

CRESST[11], DAMIC[12], CDMS[13] and CoGeNT[14] experiments use cryogenic semiconductor detectors. Their targets are crystals of Si, Ge and so on. They detect ionized electrons, heat as phonons or both of them. CDMS experiment

had the highest sensitivity in the past [15]. However, due to their relatively small scalability, their sensitivity is lower than that of noble gas detectors at present.

### 2.1.2 Solid scintillator detectors

DAMA/LIBRA(DAMA)[16] and KIMS[17] experiments use solid scintillator. Their targets and detectors are NaI and CsI crystals, respectively. DAMA experiment had reported that they observe a dark matter annual modulation (See 2.4) with  $9\sigma$ . But other experiments did not observe WIMP in DAMA allowed region. To verify DAMA's result, as an example, PICO-LON[18] group is trying to make ultra-pure NaI crystals as DAMA.

### 2.1.3 Liquid noble gas detectors

Recently, dark matter search experiments using liquid noble gases, like Xe and Ar, as a target had increased and they reported more stringent limits for WIMP-Nucleon cross section compared with other experiments. These are due to high scintillation yield and scalability at low cost compared with other detectors. XMASS[19] and DEAP3600[20] experiments are single-phase liquid noble gas detectors which use Xe and Ar as targets, respectively. LUX[21], XENON[22], DarkSide[23] and ANKOK[24] are double-phase noble gas detectors. They use liquid and gas Xe or Ar, respectively. Observing scintillation signal(S1) and ionization signal(S2), nuclear and electron recoil events can be separated.

### 2.1.4 Directional detectors

NEWAGE[25], DRIFT[26] and NEWS[27] experiments are directional dark matter search experiments. As shown in Figure. 2.3, Solar system is moving to a certain direction with velocity 230 km/s in the Galaxy. Therefore, dark matter arrival direction would have a biased distribution to the Sun's moving direction. These detector aim to detect this remarkable signature. Moreover, directional detectors could separate dark matter events from solar and atmospheric neutrino events.

## 2.2 Indirect search experiments

If dark matter is WIMP, they are gravitationally captured to galaxy center etc. Besides, if WIMP is a Majorana particle, gamma-rays, anti-matters, neutrinos and so on are generated by WIMP-WIMP annihilation. As an example, Super-Kamiokande[28] and IceCube[29] experiments look for muon neutrinos generated by WIMP-WIMP annihilations at the Galactic center.

## 2.3 Collider searches

ATLAS[2] and CMS[3] experiments at Large Hadron Collider(LHC) are trying to generate SUSY particle neutralinos by high energy proton-proton collisions. Neutralino is a strong candidate of WIMP.

A summary of the first LHC results obtained with 13 TeV center of mass energy was presented on 15<sup>th</sup> December 2015. A  $3.6 \sigma$  bump was found at 750 GeV in ATLAS diphoton spectrum[30]. In CMS data, a coinciding  $2.6 \sigma$  excess was found[31]. Even if dark matter candidate particle like neutralino is discovered by collider experiments, it is independently important to identify what is cosmic dark matter directly. If dark matter was WIMP, it is not limited to be SUSY neutralino and there is possibility for a new particle discovery.

## 2.4 Annual modulation

Dark matters are thought to be gravitationally trapped by mass of the Galaxy spherically and called as "dark matter halo". They are also expected to exist around Earth. The expected local halo density is  $0.3 \text{ GeV/cm}^3$  [32]. In dark matter halo, the Solar-system moves with  $\sim 230 \text{ km/s}$  velocity. Earth is rotating around Sun with  $\sim 30 \text{ km/s}$  velocity. Earth rotation makes seasonal difference in relative velocity between dark matter and a detector on Earth. Maximum (minimum) velocity becomes  $\sim 245$  ( $\sim 215$ )  $\text{km/s}$  on Jun. 2<sup>nd</sup> (Dec. 4<sup>th</sup>). Therefore, energy spectrum of dark matter recoil has an annual modulation [33]. This phenomena is a special signature of dark matter. So far DAMA, CoGeNT and CDMS experiments claim to have observed the annual modulation in their observed data, but others do not.

## 2.5 Expected WIMP spectrum

Expected WIMP spectrum in liquid xenon is shown in Figure 2.4. Solid black line represents yearly averaged spectrum. Red and blue dotted lines show spectra on Jun. 2<sup>nd</sup> and Dec. 4<sup>th</sup>, respectively. WIMP mass and WIMP–nucleon cross section are assumed as  $20 \text{ [GeV]}$  and  $10^{-4}[\text{pb}^{-1}]$ . WIMP interaction is expected to be very small, then low-background environment and large amount of target mass are required. Moreover, WIMP-nucleon recoil energy spectrum decrease exponentially, then a low-energy threshold is also required. The residual plot is shown in Figure 2.5. Black line represents difference between the red and blue spectra in Figure 2.4. The blue one is subtracted from red one. In low-energy region around  $\sim 0.5 \text{ keV}_{ee}$ , the residual rate turns over. If a low-energy threshold was achieved, this turn over could be observed. A low-energy threshold is important for not only WIMP search but also annual modulation analysis.

## 2.6 Current status of WIMP dark matter searches

The WIMP dark matter is being searched around the world. Figure 2.6 and 2.7 show the current status of WIMP dark matter searches in high- and low-mass regions. In high-mass region, LUX(green line) and XENON(red line) experiments are leading the situation. DAMA, CDMS and CoGeNT experiments claim WIMP detection in low-mass region. Especially, DAMA experiment had reported that they observe a dark matter annual modulation (See section 2.4) with  $9 \sigma$  with total exposure  $1.33 \text{ ton}\cdot\text{year}$  at low-mass WIMP region. Their results seem inconsistent with other

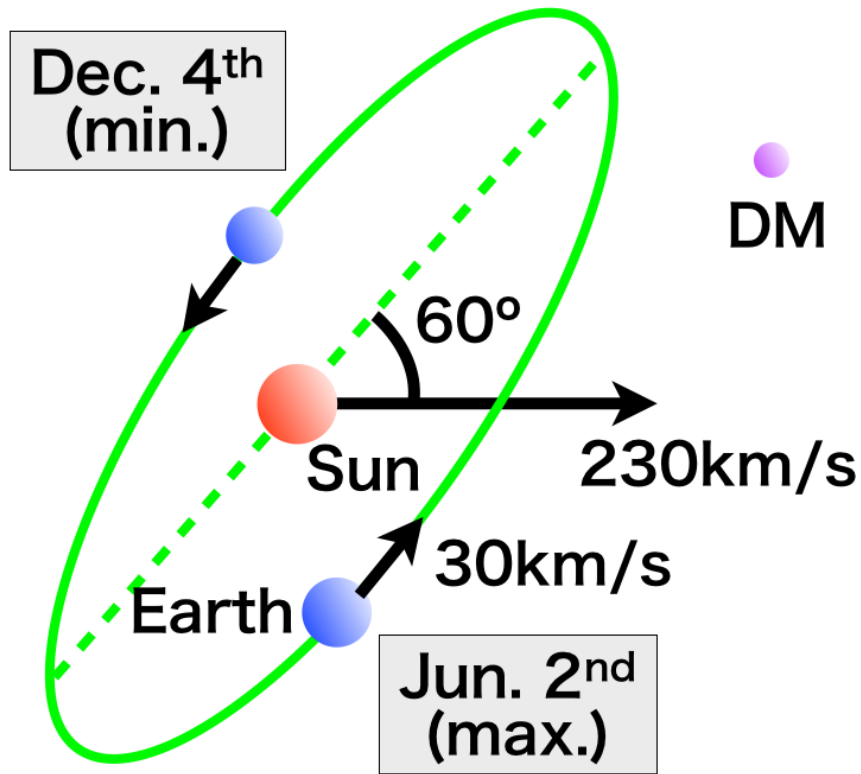


Figure 2.3: Schematic view of dark matter annual modulation. Detector on Earth revolves around the Sun. The revolution makes alteration of relative speed between dark matter and detector.

more sensitive experiments like LUX and XENON100 experiments. This situation continues over 10 years. More experiments to verify DAMA result are strongly required.

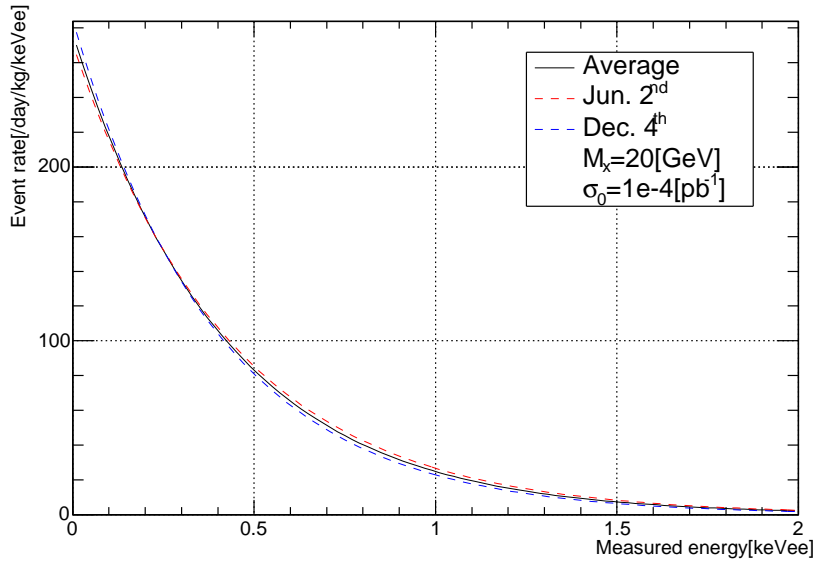


Figure 2.4: Expected WIMP spectrum in liquid xenon. Solid black line represents yearly average spectrum. Red and blue dotted lines show spectra on Jun. 2<sup>nd</sup> and Dec. 4<sup>th</sup>, respectively.

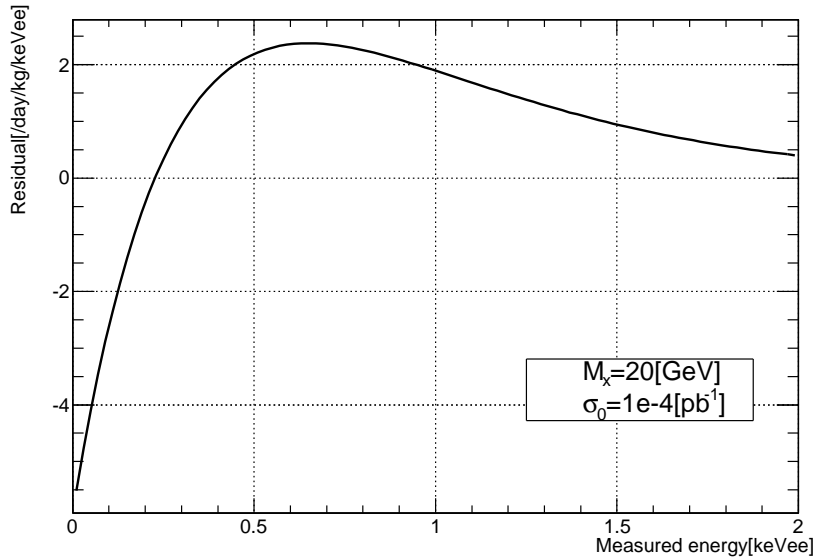


Figure 2.5: Difference between the red and blue spectra in Figure 2.4. The blue one is subtracted from red one.

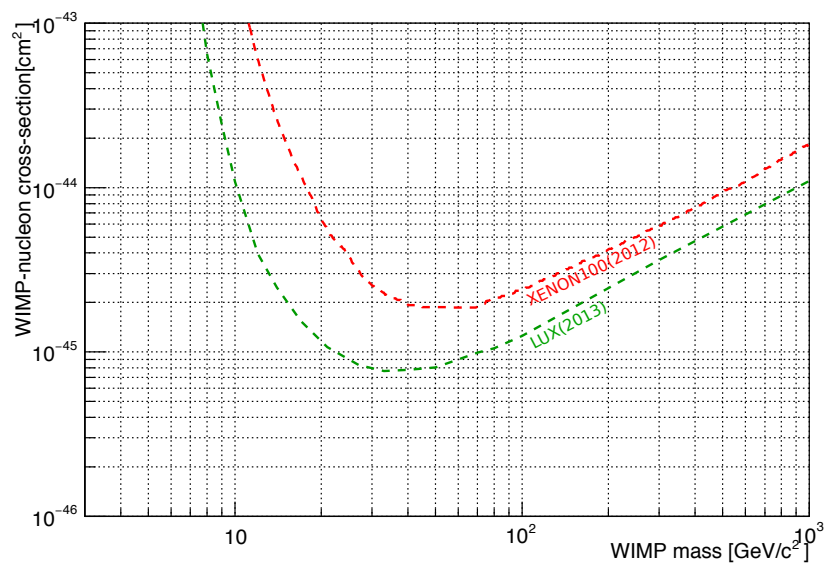


Figure 2.6: Current status of WIMP dark matter searches. LUX and XENON100 experiments using double phase xenon detectors lead the situation.

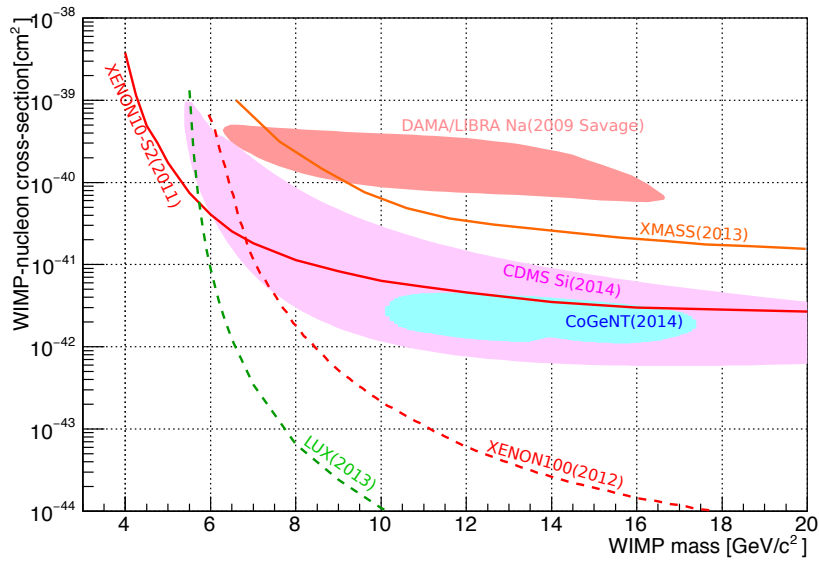


Figure 2.7: Current status of WIMP dark matter searches in low-mass region. The lines and filled regions represent 90 % C.L. upper limits and allowed region by other experiments, respectively. Orange solid line represents the result from XMASS-I dataset before refurbishment [34]. Red lines are 90 % C.L. upper limits by XENON experiments, dotted one is obtained from nuclear recoil search using both scintillation and ionization[22] and solid one is electron recoil search using only ionized electron signal [35]. Dotted Green line represents 90 % C.L. upper limits from LUX experiment [21]. Light red, magenta and light blue filled regions are allowed region by DAMA(Na target)[36], CDMS(Si target)[13] and CoGeNT[14] experiments, respectively.

# Chapter 3

## XMASS experiment

XMASS project is ongoing at Kamioka Observatory in Japan. XMASS stands for the followings.

- Xenon detector for weakly interactive MASSive particles
- Xenon MASSive detector for Solar neutrinos
- Xenon neutrino MASS detector

XMASS detector is a general-purpose detector using large amount of high-purity xenon and ultra-low background PMT(PhotoMultiplier Tube)s. XMASS-I experiment is being operated and mainly aims to detect dark matter directly. XMASS-1.5 is a next step of XMASS-I and consists of a new geometry detector and larger liquid xenon. Final goal of the current XMASS project is XMASS-II which uses 20 tons of liquid xenon. XMASS-II aims not only dark matter search but also solar neutrino study and neutrino-less double beta decay etc.

### 3.1 XMASS-I detector

XMASS-I detector is located in Kamioka Observatory (water equivalent depth 2700m) in Japan [19]. Figure 3.1 and 3.2 show schematic views of the XMASS-I detector. It consists of liquid xenon and 642 PMTs. The amount of the liquid xenon is 832 kg in the active region. 642 of 2-inch PMTs(630 of Hexagonal PMTs Hamamatsu R10789-11 and 12 of Round PMTs Hamamatsu R10789-11MOD ) are installed around the liquid xenon, and they detect the scintillation light from the liquid xenon. Oxygen-free copper is used for the PMT holder to reduce background from outside of xenon. XMASS-I detector is installed in purified water in a stainless steel tank. 72 of 20-inch PMTs(Hamamatsu R3600) are installed in the tank to detect Cherenkov light produced by cosmic-ray muon. The water tank works as an active veto for cosmic-ray muons as well as a shield for gamma-rays and fast neutrons from outside of the detector.

XMASS-I detector has high sensitivity for not only nuclear recoils but also electronic events. WIMP dark matter search results had been published by two methods. One is a search for low mass WIMP without particle discrimination between nuclear and electron recoil events. This study excluded part of DAMA/LIBRA favored

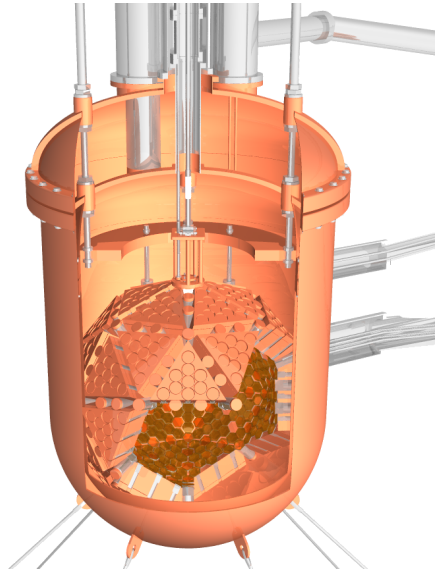


Figure 3.1: A schematic view of XMASS-I detector. Inner detector(ID) is installed in a vacuum insulating dual structure vessel.



Figure 3.2: Water tank for XMASS detector. Its height and diameter are 10 m and 11 m. 20 inch PMTs are installed in the tank and work as outer detector(OD).

region [34]. The other one is inelastic WIMP–nucleus scattering search on  $^{129}\text{Xe}$ . 40 keV gamma–ray from Xe nucleus excited by WIMP scattering had been looked for [37]. Thanks to high sensitivity for electron recoils, search for solar axion and bosonic super–WIMP dark matter had also been conducted [38, 39].

### 3.1.1 Xenon circulation system

Figure 3.3 shows a schematic view of xenon circulation system in XMASS–I detector. Before the observation, the liquid xenon was kept in a liquid xenon reservoir tank. The volume of the tank is  $\sim 700$  L. A refrigerator kept xenon in liquid phase. The liquid xenon can be evaporated by a rod heater in the tank. The evaporated gas xenon was purified by two getters and then monitored by frost point meter. After cooling the ID by liquid nitrogen, the gas xenon was liquefied by two refrigerators and filled into the ID. In emergency case like refrigerator failing, automatic safety system will be activated. The first one uses liquid nitrogen to cool down xenon in ID. The second one used two  $10\text{ m}^3$  gas xenon emergency tanks to collect xenon into the tank compressing gas xenon by a xenon gas compressor.

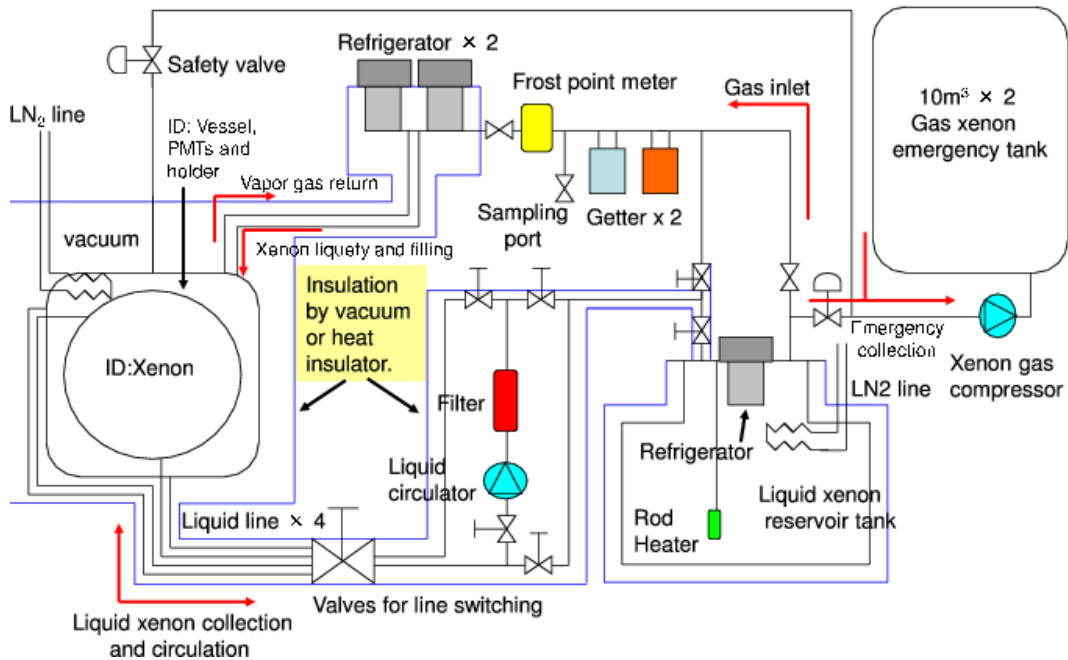


Figure 3.3: A schematic view of xenon circulation system in XMASS–I detector.

### 3.1.2 Data acquisition system

Figure 3.4 shows a schematic view of Data acquisition(DAQ) system in XMASS–I experiment. The signals from 642 of PMTs are amplified by preamplifiers. Then analog–timing–modules(ATMs) which are previously used in SK experiment [40] and flash analog–to–digital converters CAEN V1751(FADCs) receive the amplified signals. ATMs function as analog–to–digital converters(ADCs) and time–to–digital

converters(TDCs) and record charge integral and signal arrival time. The FADCs record waveforms of individual PMT signal with 10bit 1GS/s. Width of an acquisition window of FADC is 10  $\mu$ sec. When 4 PMT hits are observed in ATMs, a global trigger is issued to ATMs and FADCs. Then the event is recorded. OD PMT signals are sent to ATMs for OD. A separate trigger for OD is generated when OD signals were observed. The OD trigger threshold is 7 OD PMT hits.

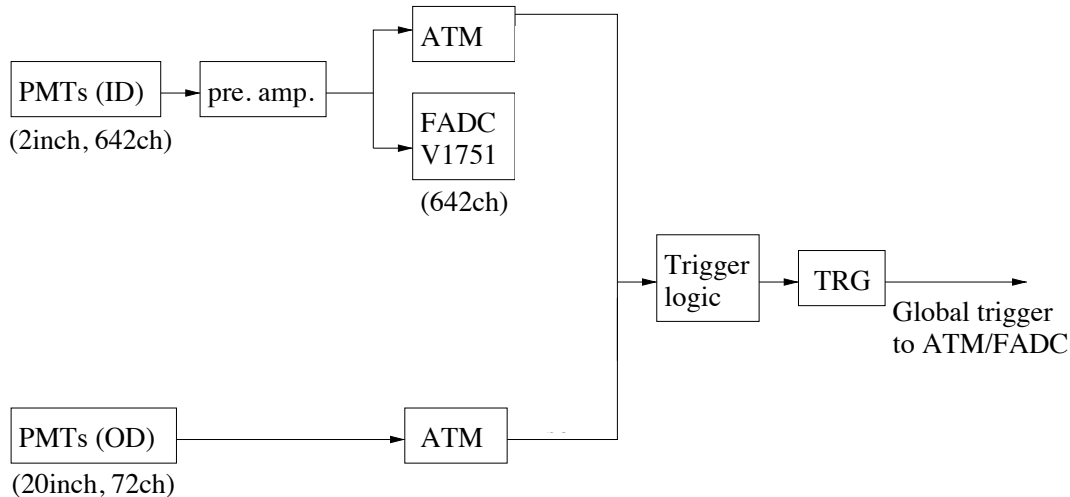


Figure 3.4: A schematic view of DAQ system in XMASS-I experiment.

## 3.2 Detector simulation

Using Geant4 simulation toolkit[41], Monte-Calro(MC) simulation program of XMASS detector had been developed. Figure 3.5 shows XMASS detector geometries constructed in XMASS MC. Geometries of PMTs and other parts in XMASS MC reproduce actual detector very well. In MC, scintillation lights are generated by incident particles and XMASS MC track all of generated photons. Parameters in MC like absorption/scattering length of the liquid xenon and reflectivity of geometries are determined to make MC results to agree calibration data [42].

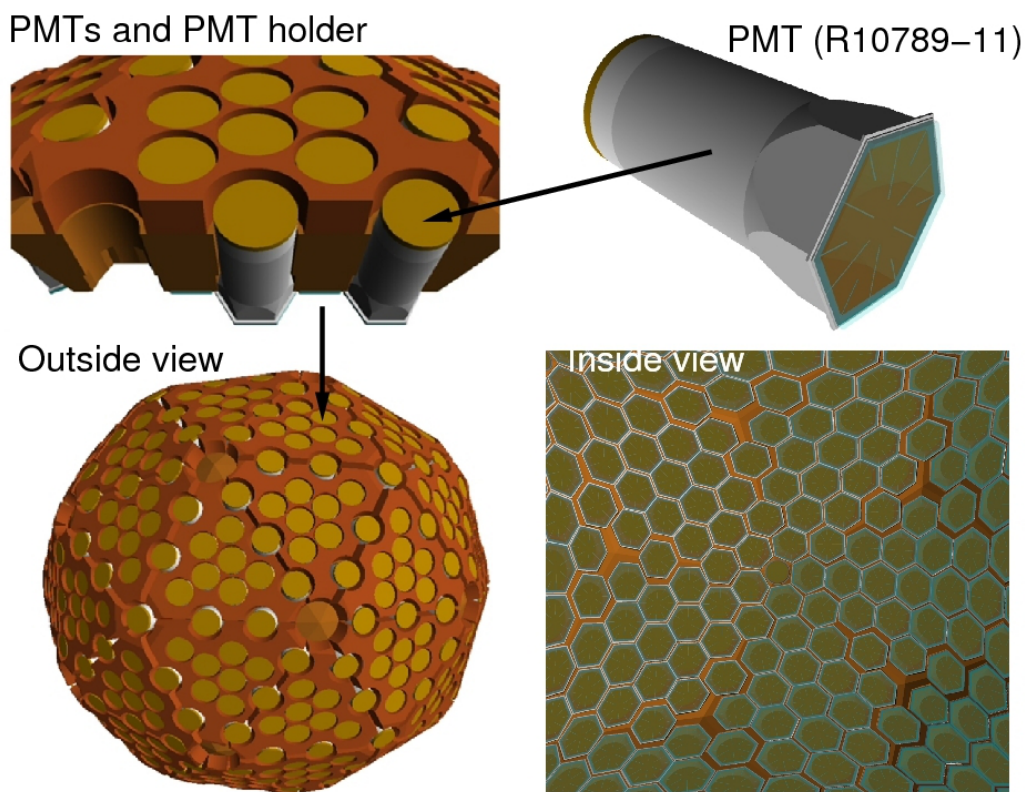


Figure 3.5: XMASS detector geometries constructed in XMASS MC.

### 3.3 Xenon

Xenon(Xe), which is used in XMASS experiment, is a noble gas which has many advantages for dark matter search experiment as follows. Properties of xenon are listed in Table 3.1. Figure 3.6 and 3.7 show phase diagram and attenuation coefficient for gamma-ray of xenon.

#### High mass number

Mass number(A) of xenon is around 132. The spin-independent WIMP-nucleon cross section is thought to be in proportion to  $A^2$ . Xenon is a suitable target for a WIMP search experiment.

#### High density

Xenon has high atomic number 54 and high density  $\sim 3 \text{ g/cm}^3$  in liquid phase. Thanks to high density, a compact and massive detector can be constructed. Moreover, gamma attenuation length in liquid xenon is short ( $\sim 5.7 \text{ cm}$  for 1 MeV gamma-ray). External high energy gamma-rays are attenuated rapidly upon entering LXe. Therefore, gamma-ray background(BG) rate around center of detector will be reduced. This BG reduction called as "self-shielding" of LXe is a main idea of the XMASS detector design.

#### Directly observable wavelength of scintillation photons

Scintillation light from xenon has  $\sim 178 \text{ nm}$  wavelength[43] and can be directly observed by photon detectors like PMT.

#### High scintillation yield

Scintillation yield of LXe is  $\sim 60$  photons/keV at 122keV [44]. This high yield enables low-energy threshold.

#### Easy phase change

The temperature of gas-liquid phase change is  $\sim 165 \text{ K}$  at 1 atm. Purification and distillation are relatively easily applied.

#### Isotope separation

Isotope separation is available. Separating isotopes, spin of dark matter can be studied. Enrichment of  $^{136}\text{Xe}$  can improve double beta decay search. On the other hand, depleting  $^{136}\text{Xe}$  can improve solar pp neutrino measurement.

#### Particle identification(PID)

By scintillation mechanism of liquid xenon, its scintillation light has variable waveforms according to interacting particles. Track length of nuclear recoil and  $\alpha$ -ray (electron recoil,  $\beta$  and gamma-ray) is relatively short(long) and then  $dE/dx$  will be high(low). Therefore, ionized electron density becomes high(low) and time for recombination will be short(long). PID using this property could be done.

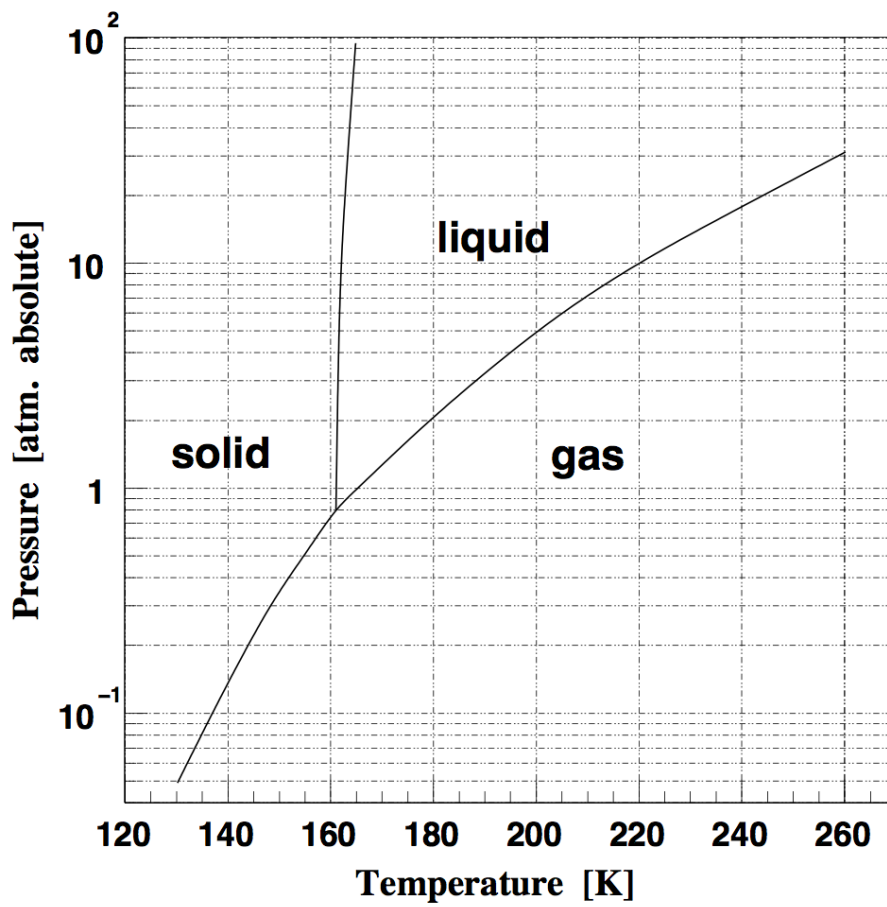


Figure 3.6: Phase diagram of xenon [48, 49]

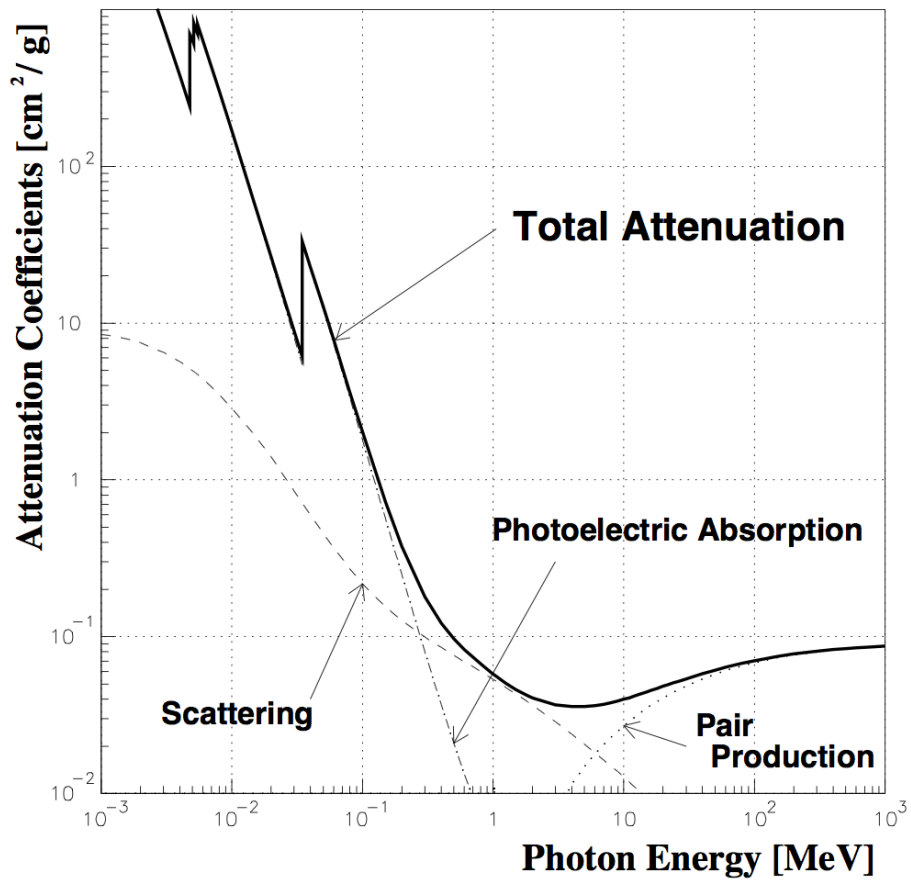


Figure 3.7: Attenuation coefficient of xenon for gamma-ray [50]

Table 3.1: Xenon properties

Property	Value	Condition
Atomic number	54[45]	
Mass number	131.29[45]	
Boil point	165.1 K[45]	1 atm
Melting point	161.4 K[45]	1 atm
Density	2.96 g/cm <sup>3</sup> [46]	161.5 K in liquid
Radiation length	2.77 cm[47]	in liquid

Table 3.2: Isotopes of Xe [43]

Xe Isotope	Natural abundance(%)	Spin	Double $\beta$ decay
<sup>124</sup> Xe	0.096	0	No
<sup>126</sup> Xe	0.090	0	No
<sup>128</sup> Xe	1.92	0	No
<sup>129</sup> Xe	26.44	1/2	No
<sup>130</sup> Xe	4.08	0	No
<sup>131</sup> Xe	21.18	1/2	No
<sup>132</sup> Xe	26.89	0	No
<sup>134</sup> Xe	10.44	0	No
<sup>136</sup> Xe	8.87	0	Yes

### 3.3.1 Isotopes of xenon

Xe has several isotopes. The abundances and spins of the stable Xe isotopes are summarized in Table 3.2. Since Xe has stable isotopes with different spin, Xe detector can search for both spin-dependent and spin-independent dark matter events. Neutron emission would generate radioactive Xe isotopes. These radioactive isotopes will decay and can be removed being kept in low-background environment for a while due to their short lifetime. The longest lifetime of radioactive Xe isotopes is 11.934 days of <sup>131m</sup>Xe.

Table 3.3: Optical characteristics of liquid xenon [43]

Property	Value	Condition	Optimization
Wavelength Peak of scintillation light	175 nm, 178 nm		
Absorption length for scintillation light(ABSL)	$\geq 100$ cm		Yes
Rayleigh scattering length	30 - 60 cm		Yes
Refractive index	$1.61 \pm 0.1$	$(177 \pm 5)$ nm	
Energy per scinti. photon	$(23.7 \pm 2.4)$ eV	electrons	
	14.2 eV	electrons	
	12.5 eV, 12.7 eV	electrons	
	$(19.6 \pm 2.0)$ eV	$\alpha$ particles	
	$(16.3 \pm 0.3)$ eV	$\alpha$ particles	
Lifetime singlet	22 ns		
Lifetime triplet	4.2 ns		
Recombination time	45 ns	Dominant for e, $\gamma$	
Relative scintillation efficiency	Fig.3.9		

### 3.3.2 Optical characteristics of liquid xenon

Optical characteristics of liquid xenon are summarized in Table 3.3. There are several parameters which are not correctly measured or affected by xenon purity. They are required to be optimized by actual detector response.

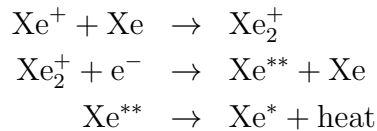
### 3.3.3 Scintillation mechanism of xenon

When xenon interact with some incident particle, it will become excited state by deposit energy then emit vacuum ultra violet(VUV). Figure 3.8 shows a schematic view of scintillation mechanism of xenon. Xenon has two processes to emit scintillation light.

- Scintillation mechanism without re-combination



- Scintillation mechanism with re-combination





One is to become excited state directly as Eq.3.1. The other one is to be ionized at first and then become excited state by recombination with ionized electron as Eq.3.2. In both of these processes, wavelength of emitted photons are same because their final situations are same. But decay constant of the scintillation light differs between two processes.

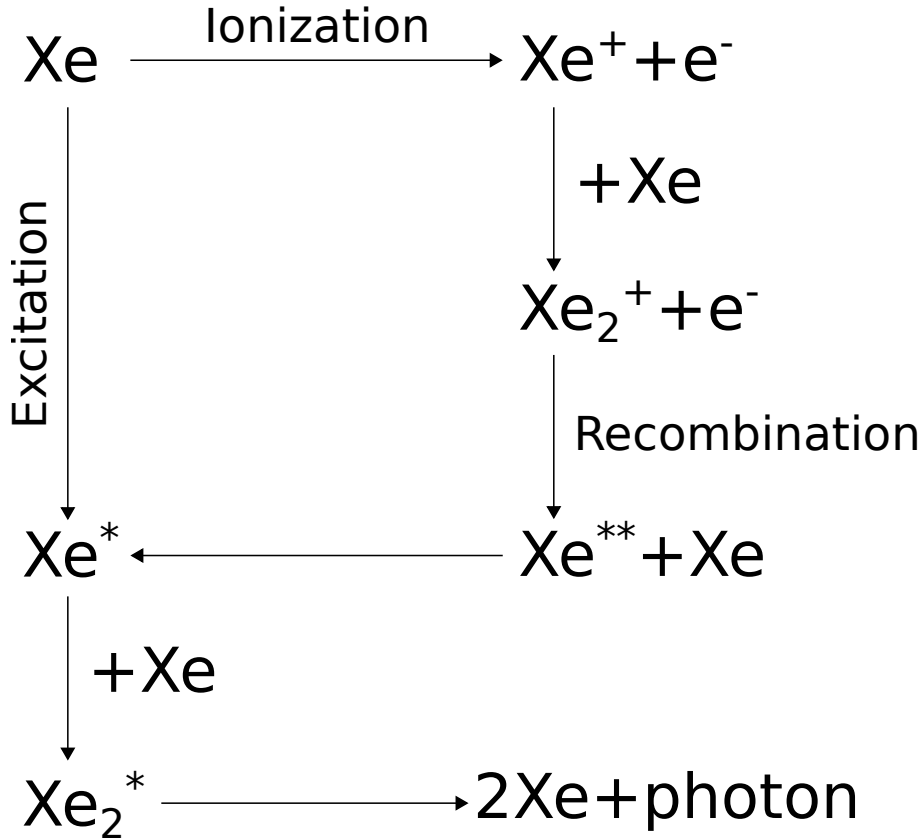


Figure 3.8: Scintillation mechanism of xenon

### Relative scintillation efficiency

There is no accurate measurement in xenon scintillation yield by nuclear recoil. Therefore, there is a large uncertainty. Figure 3.9 shows the relative scintillation efficiency of nuclear recoil ( $L_{\text{eff}}$ ). Vertical axis is the relative scintillation efficiency and it is normalized to scintillation yield of 122 keV gamma-ray from  $^{57}\text{Co}$ . Red line represents center value. Purple and light purple bands represent  $\pm 1 \sigma$  and  $\pm 2 \sigma$  bands, respectively. In order to obtain conservative result,  $-1 \sigma$  value is used to convert nuclear recoil energy into scintillation light in WIMP simulation in XMASS detector.

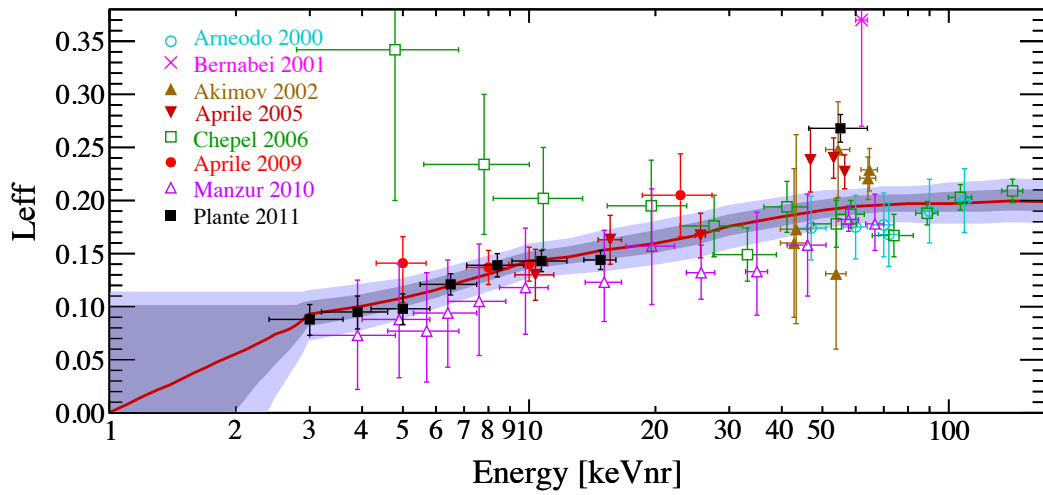


Figure 3.9: The relative scintillation efficiency of nuclear recoil ( $L_{\text{eff}}$ ) [51]. Vertical axis is the relative scintillation efficiency and normalized to scintillation yield of 122 keV gamma-ray from  $^{57}\text{Co}$ . Solid Red line represents center value. Purple and light purple bands represent  $\pm 1 \sigma$  and  $\pm 2 \sigma$  bands, respectively.

Table 3.4: Environmental background sources in Kamioka mine.

	Ground surface	Kamioka mine
Cosmic-ray muon/cm <sup>2</sup> /sec[28]	$1.1 \times 10^{-2}$	$10^{-7}$
Neutron[52][53]		
Thermal neutron/cm <sup>2</sup> /sec	$1.4 \times 10^{-3}$	$8.3 \times 10^{-5}$
Fast neutron/cm <sup>2</sup> /sec	$1.2 \times 10^{-2}$	$1.2 \times 10^{-5}$
Rn Bq/m <sup>3</sup> (summer)[28]	0~10	~2000
Rn Bq/m <sup>3</sup> (winter)[28]	0~10	40
Gamma-ray (>500keV)[54]	-	0.71/cm <sup>2</sup> /sec

## 3.4 Environmental backgrounds

In dark matter search experiments, not only XMASS, understanding of the effects in observed data by background events is necessary to identify dark matter signals. There are two types of background. One is background events due to radiations from outside of the liquid xenon, like PMTs, PMT holders, rocks around laboratory and so on. The other one is from inside of the liquid xenon, like impurities in it.

### 3.4.1 Background from outside of Xe

To achieve low-background environment for dark matter search, XMASS-I detector is located 1000 m (2700 m.w.e) underground in Kamioka mine in which Super-Kamiokande(SK)[28] detector is also located. Environmental background level in Kamioka mine are summarized in Table 3.4. Purified water tank is used as a shield against external gamma-rays and fast neutrons.

#### Cosmic-ray muon

The rock over the laboratory works as a shield for cosmic ray muons. Cosmic-ray muon flux in Kamioka underground site is  $10^{-5}$  times of that on the ground [28]. The water tank is used as a shield for fast neutrons and gamma-rays. Furthermore the water tank works as an outer detector(OD) to veto cosmic-ray muons. Cherenkov lights caused by cosmic-ray muons are detected by 20-inch PMTs in the water tank(OD PMTs). Detail background rate estimation is explained in section 6.6.1.

#### Gamma-ray

External gamma-rays are mainly produced from radioactive isotopes in mine rocks and in detector parts. To eliminate external gamma-rays, XMASS-I detector is consisted of low-background parts, and the detector is installed in a water tank shield. For example, special developed low-radioactivity PMTs R10789 are used to reduce gamma-ray background from PMTs.

## Neutron

Environmental fast neutrons are produced from outside of the detector system via following processes.

- Fission of radioisotopes in  $^{232}\text{Th}$  and  $^{238}\text{U}$  decay series included in mine rocks.
- $(n,\alpha)$  reaction from  $\alpha$  decay in  $^{232}\text{Th}$  and  $^{238}\text{U}$  decay series included in mine rocks.
- Spallation reaction by high-energy cosmic-ray muons.

These neutrons are reduced by the water tank. Detail background rate estimation is explained in section 6.6.1.

## Radon in water tank

The radioactive noble gas  $^{222}\text{Rn}$  is continuously generated in the  $^{238}\text{U}$  decay series. It has a half-life of 3.82 days and potentially dissolves into purified water and gases like xenon and air. It can be a source of serious background events. For example, in Kamioka mine, the radon concentration is about 2000 and 40 Bq/m<sup>3</sup> in summer and winter, respectively, because of the wind direction [55].

Gamma-rays from radon daughter nuclei in purified water in water tank can be background events from outside of xenon. Therefore radon concentration in purified water has to be monitored continuously.

High sensitivity radon detectors had been developed especially for underground experiments in Kamioka mine like XMASS and SK [56]. A schematic view and a picture of the radon detector is shown in Fig.3.10 and Fig.3.11 . A negative high voltage(HV) supplied to a PIN photodiode in the detector vessel. More than 90% of radon daughter nucleus (Po) tend to become positively charged [57].  $\text{Po}^+$  ions will be captured by the negative-HV-supplied PIN photodiode. Finally,  $\alpha$  decays of  $^{218}\text{Po}$  and/or  $^{214}\text{Po}$  are measured by the PIN photodiode. The count rates in the signal region will be converted to radon concentration using a calibration factor of (count/day)/(mBq/m<sup>3</sup>). To improve sensitivity, a new radon detector with hermetic parts has been developed and their performance such as HV dependence of the calibration factor were investigated [58, 59].

Using this principle, radon concentration in purified water in the tank has been monitored continuously with a special radon assay device since March 2014 [60]. Figure 3.12 shows time variation of radon concentration in XMASS purified water. Maximum  $^{222}\text{Rn}$  concentration was  $(1.4\pm 0.2) \times 10^2$  mBq/m<sup>3</sup>. It corresponds to  $(1.4\pm 0.2) \times 10^{-5}$  events/kg/day/keV in XMASS-I detector. This was caused by accidental mine air contamination in the water purification system. The problem was already fixed. Another small peak around 215 elapsed days was caused by accidental mine water supply at a power failure. Except for these troubles, no significant radon excess above the background level of the assay device was observed. The background level of the current assay device is about 10 mBq/m<sup>3</sup>. It corresponds to  $(1.4\pm 0.2) \times 10^{-6}$  events/kg/day/keV in XMASS-I detector. The absolute value of the maximum amplitude of time variation as a result of model independent

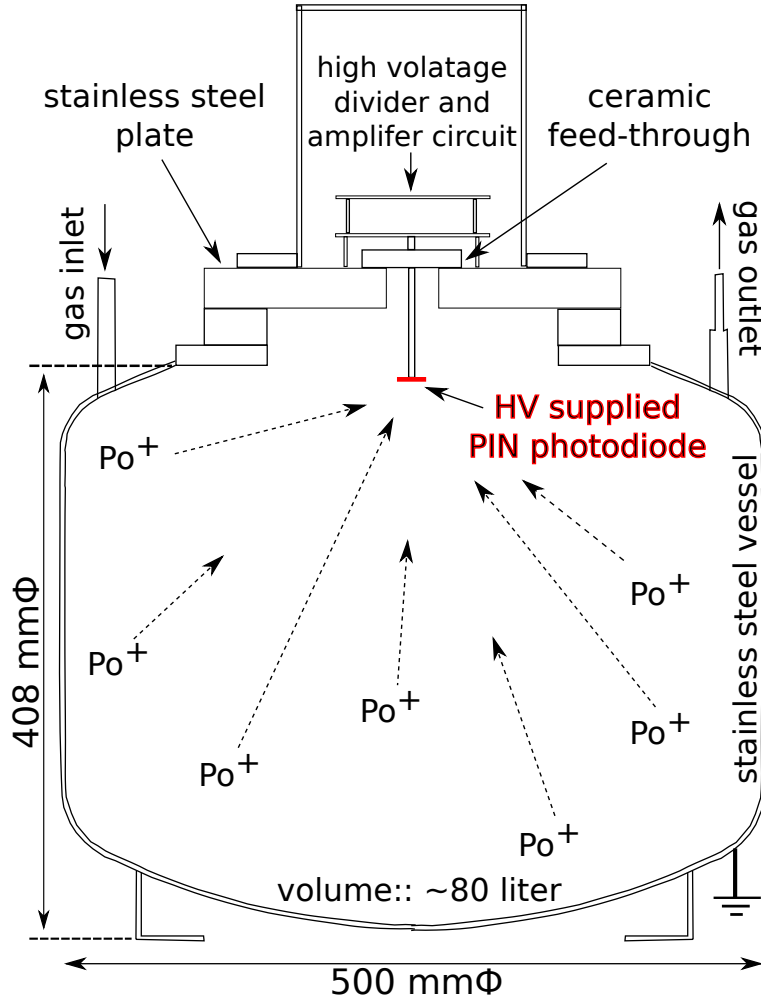


Figure 3.10: A schematic view of 80 L radon detector and its detection principle. Radon daughter nuclei polonium ions are captured to the surface of PIN photodiode by an electric field.

modulation analysis is about 0.02 events/day/kg/keV. No effect from Rn in water is expected to annual modulation analysis.

### 3.4.2 Background from inside of Xe

Since radiation from inside of xenon can not be reduced by the water tank, background sources in xenon are needed to be reduced as much as possible. Main components of background sources in xenon are  $^{222}\text{Rn}$  and  $^{85}\text{Kr}$ .

#### Radon

As described in the previous section,  $^{222}\text{Rn}$  is continuously generated from  $^{238}\text{U}$  decay series and it potentially dissolves into liquid xenon. Decay of  $^{222}\text{Rn}$  daughter nuclei dissolved in xenon can be background events. A study is explained in section 6.6.3 in detail.

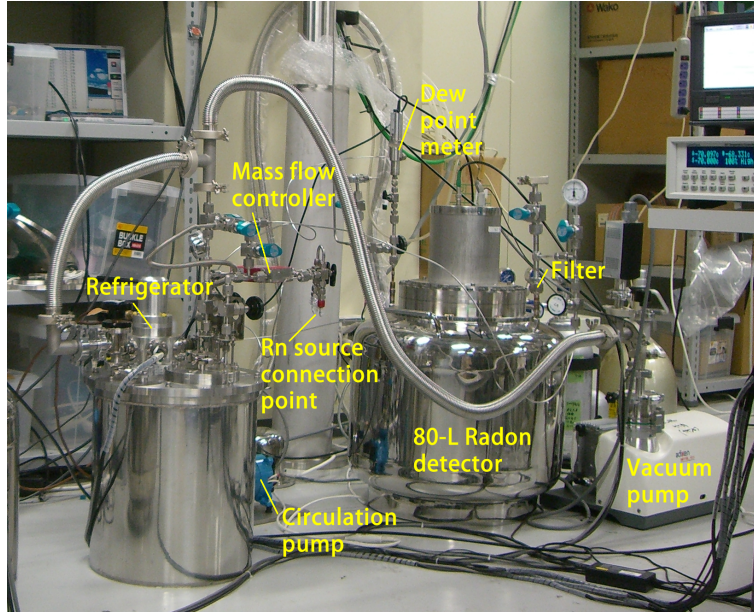


Figure 3.11: A picture of a calibration system for a radon detector in Kobe university.

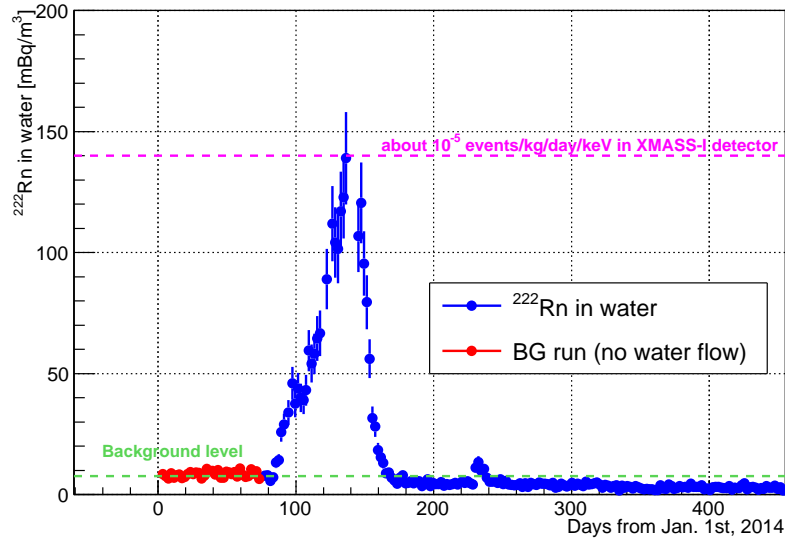


Figure 3.12: Time variation of radon concentration in the water tank.

## Krypton

Commercially available xenon contains  $\sim 10^{-7}$  mol/mol (0.1 ppm) Krypton. Half-life of  $^{85}\text{Kr}$  is 10.756 y and relatively long. Decay scheme of  $^{85}\text{Kr}$  is shown in Fig. 3.13.  $^{85}\text{Kr}$  decay has a continuous energy spectrum since its decay process is  $\beta$  decay. Therefore, it can overlap dark matter signal in low-energy region. Boiling points of

krypton and xenon are different, and then they can be separated by a distillation.

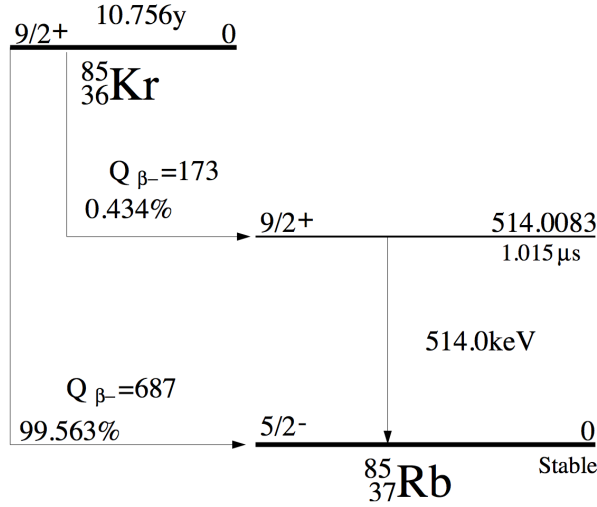


Figure 3.13:  $^{85}\text{Kr}$  decay scheme[61]

### 3.5 Background from ID surface

Dominant background events in XMASS-I detector occur due to radioactive impurities at inner detector surface. We found unexpected  $^{238}\text{U}$  and  $^{210}\text{Pb}$  radioactive impurities exist in the Aluminum sealing parts of PMTs. Figure 3.14 shows the Aluminum sealing parts of a hexagonal PMT. The Aluminum seal is used between the PMT body and its window. There is another major background source from ID surface. Cu plates are attached on the inner detector surface. Figure 3.15 shows a picture of XMASS-I detector surface during the construction.  $^{210}\text{Pb}$  deposits onto the Cu plate surface.

Scintillation light, Cherenkov light and bremsstrahlung radiation due to  $\beta$ -ray in PMT quartz windows by radioactive impurities in PMT sealing Aluminum become background events in low-energy region ( $< 10\text{keV}_{ee}$ ). Scintillation light from surface  $^{210}\text{Pb}$  becomes such event, too. Activities of these RIs had been measured using HPGe detectors in Kamioka. Using MC with the measured activities, expected energy spectra from these background events were estimated. Figure 3.16 shows a summed up expected background spectrum after event selections explained in Section 5.3. Energy spectrum of observed dataset in Fig. 5.7 can be qualitatively explained by these background MC. PMT Aluminum backgrounds are dominant components. Uncertainties of these expected backgrounds are considered in  $K_{i,j}$  explained in Section 6.1 as a part of systematic errors.

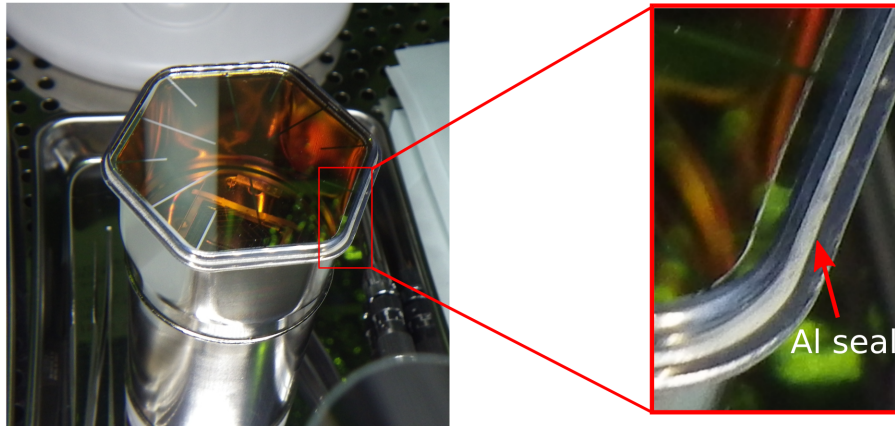


Figure 3.14: The Aluminum sealing parts of PMTs. Radioactive impurities  $^{210}\text{Pb}$  and  $^{238}\text{U}$  are found in this parts.



Figure 3.15: A picture of XMASS-I detector surface taken during the construction. Cu plates are attached on the detector surface.

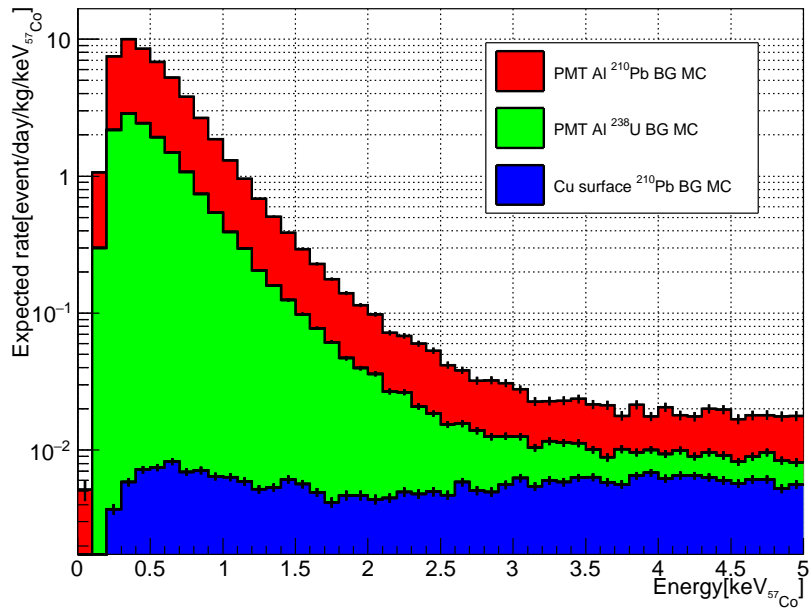


Figure 3.16: Summed up expected background spectrum in XMASS-I detector. Blue, Red and Green histograms represent Cu surface  $^{210}\text{Pb}$ ,  $^{238}\text{U}$  in PMT Aluminum and  $^{210}\text{Pb}$  in PMT Aluminum, respectively.

# Chapter 4

## Calibration

Here, an outline of XMASS-I detector calibration is described. Energy calibrations in low-energy region which are newly obtained from this study are explained in detail. See also [42] for detail.

### 4.1 LED calibration

One p.e. gain table for each PMT is created by a LED calibration. Eight blue-light LEDs are installed in the PMT holders. The LED calibration has been operated in parallel with physics data taking. When LEDs are flashed, a LED trigger is issued. Therefore LED events are rejected by a trigger cut.

### 4.2 Inner calibration system

Energy response of the liquid xenon is calibrated using radioisotope sources. XMASS-I detector has an inner calibration system. Figure 4.1 shows a schematic view of the inner calibration system. After taking top PMT off, oxygen-free copper rod is inserted into the liquid xenon. A source rod is attached at the tip of the copper rod and inserted into the detector directory. There are several source rods in which radiation sources are sealed. The sealed sources are  $^{57}\text{Co}$ ,  $^{241}\text{Am}$ ,  $^{55}\text{Fe}$ ,  $^{109}\text{Cd}$  and  $^{137}\text{Cs}$ . The source rod is controlled by a stepping motor on the top of the inner calibration system. The source position accuracy is  $\pm 1$  mm. Figure 4.2 shows a picture of a sample of the  $^{57}\text{Co}$  source rod.

### 4.3 Energy calibration

#### 4.3.1 Non-linearity of energy scale

Scintillation yield of liquid xenon is not proportional to the energy of the initial particles. Therefore, the non-linearity of energy scaling needs to be studied. Figure 4.3 shows the relative scintillation efficiency of electron events divided by electron energy in XMASS MC. This energy non-linearity of the liquid xenon was introduced to XMASS-I detector simulation referring [62]. However, it is not sufficient. The

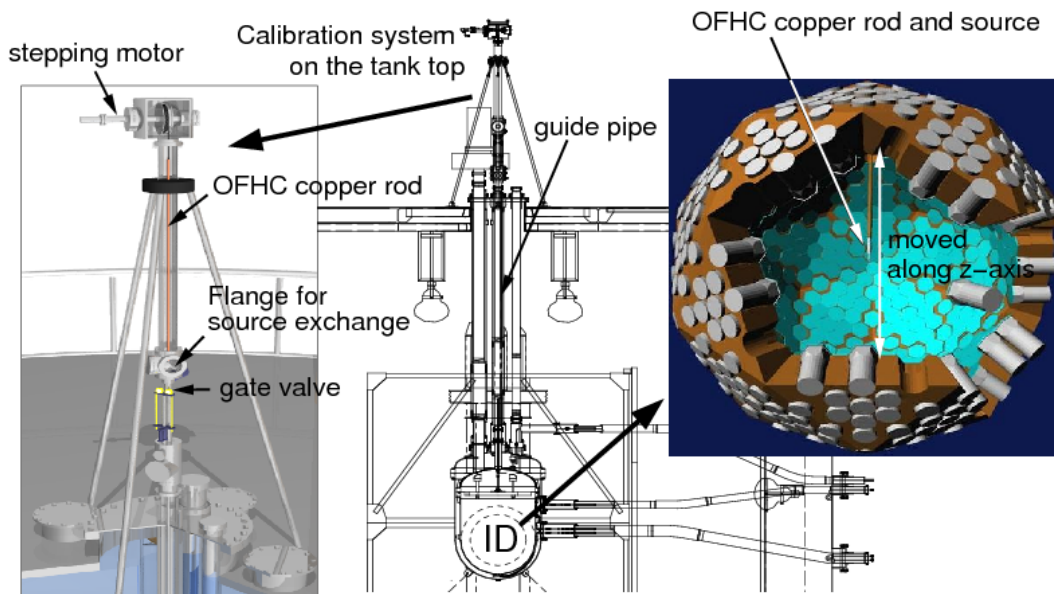


Figure 4.1: Inner calibration system for XMASS-I detector.

detector MC simulation can not reproduce energy response of the XMASS-I detector sufficiently. An extra energy scaling was applied to optimize the energy response in the simulation.

### 4.3.2 5.9 keV

There are two types of  $^{55}\text{Fe}$  calibration sources. Figure 4.4 and 4.5 show the photos of the older one and the new one. Surface roughness of the older one is  $\sim 20\mu\text{m}$  and it is larger than  $\sim 5\mu\text{m}$  which is absorption length of xenon for 5.9 keV gamma-rays. New one's surface roughness was controlled to be less than  $1\mu\text{m}$ . The new source has a flat surface structure. In order to reduce its surface roughness, buffing was applied.

Figure 4.6 shows the results of the energy calibration. Black points are before the new  $^{55}\text{Fe}$  source calibration. Error bar at 5.9 keV was very large. This was due to systematic uncertainty of reflectivity on the old  $^{55}\text{Fe}$  source surface. The value of error was  $\sim 18.6\%$ .

New  $^{55}\text{Fe}$  source was made to reduce the systematic error. To study surface reflectivity,  $^{241}\text{Am}$  source was made with the same geometry and surface roughness. XMASS-I detector calibration data had been taken using these sources and energy calibration at 5.9keV had been done again. Comparing light yield at 60 keV peak from needle (like Figure 4.2) and new flat  $^{241}\text{Am}$  sources, the reflectivity of source surface was estimated. And then, 5.9 keV calibration with new  $^{55}\text{Fe}$  source was done using the estimated reflectivity. Red points in Fig. 4.6 are the result of energy calibration at 5.9 keV using new sources. Thanks to the flat structure sources, the uncertainty at 5.9 keV became small. The new uncertainty is -2.0, +1.1%. Table 4.1 shows the systematic error list of the energy scaling at 5.9 keV with that at 1.65



Figure 4.2: A picture of a sample of a calibration rod.  $^{57}\text{Co}$  and  $^{241}\text{Am}$  calibration sources have this shape.

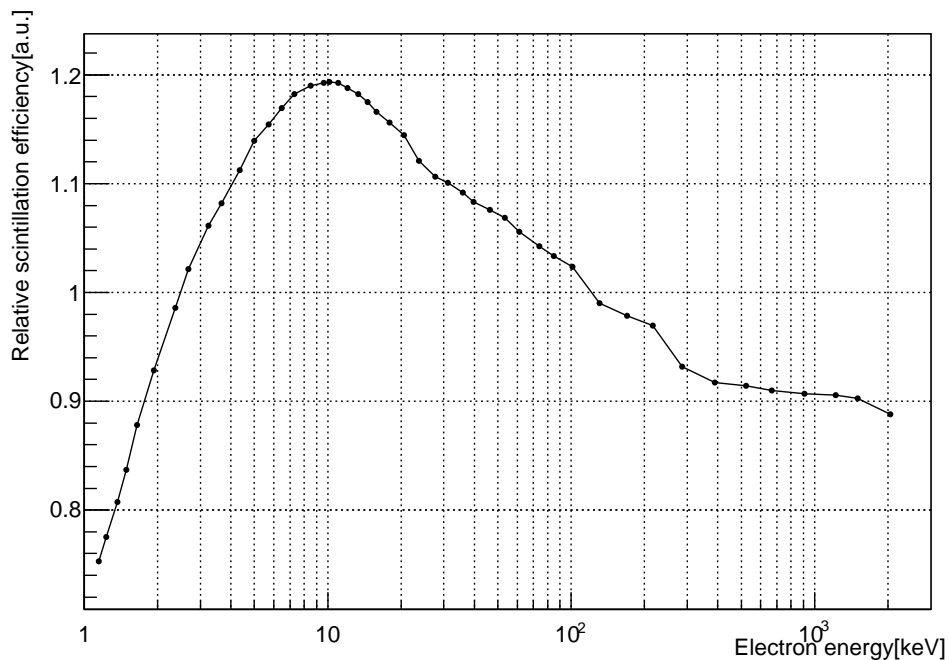


Figure 4.3: Non-linearity of the liquid xenon light yield introduced in XMASS MC referring [62]. Horizontal axis represents electron's energy. Vertical axis represents relative scintillation efficiency divided by electron energy.

keV. These results are newly obtained from this study.

### 4.3.3 1.5 and 1.8 keV

Not only the 5.9 keV (main peak), but also an escape peak by 1.5 and 1.8 keV can be obtained in the  $^{55}\text{Fe}$  calibration. Blue points in Figure 4.7 show observed P.E. distribution in the  $^{55}\text{Fe}$  calibration. A main peak and an escape peak can be seen.

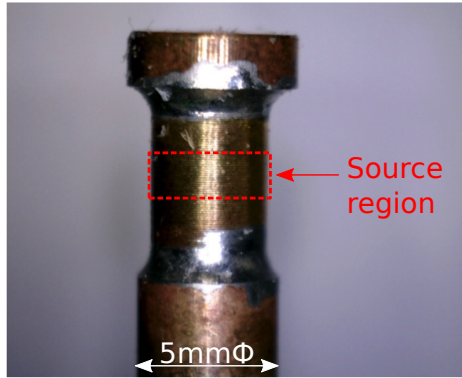


Figure 4.4: Picture of the old  $^{55}\text{Fe}$  calibration source. Its surface roughness is larger than absorption length of xenon for 5.9 keV gamma-ray.



Figure 4.5: Pictures of a sample of the new  $^{55}\text{Fe}$  and  $^{241}\text{Am}$  calibration sources. Surface of the sources has a flat structure and its roughness is controlled to be less than  $1\mu\text{m}$  by buffing.

Figure 4.8 shows the principle of the escape peak events. When Xenon's characteristic X-ray ( $L_{\alpha 1}$ : 4.1 keV or  $L_{\beta 1}$ : 4.4 keV) escapes into source geometry from 5.9 keV X-ray interaction, effectively 1.5 or 1.8 keV X-ray event can be observed. Comparing this escape peak in calibration data and MC, energy scaling at 1.65 keV was done. Because fluorescence yield of 1.5 and 1.8 keV is close, the mean value of them 1.65 keV was selected to be tuned.

The 1.65 keV peak in the calibration data was fitted by escape MC in the  $^{55}\text{Fe}$  calibration and single Gaussian function for 5.9 keV main peak. Figure 4.7 shows the escape peak in  $^{55}\text{Fe}$  calibration data, that in MC and fitting Gaussian function. Blue, magenta points and green line represent calibration data, escape MC after energy scaling and single Gaussian for main peak, respectively. Red points represent summed up escape MC and single Gaussian. The escape peak is well reproduced by XMASS-I detector MC after energy scaling. The first energy calibration below 5.9 keV was conducted in this study.

In Table 4.1, the systematic errors at 1.65 keV are summarized with that at 5.9 keV. By shell's effect, attenuation length for 4.1 and 4.4 keV X-rays are longer than that for 5.9 keV. The 1.5 and 1.8 keV events will have the same position distribution

Table 4.1: Systematic uncertainties of energy scale determination at 1.65 keV and 5.9 keV.

Items	Relative uncertainty[%]	
	5.9keV	1.65keV
Source position uncertainty	<0.02	
Sagging on 2pi source surface	- 0.2, +0	
Secular change of surface condition	<0.04	
2pi source surface roughness	-0.10, +0.34	
4pi $^{241}\text{Am}$ energy scaling error	-1.7, +0.9	
Fitting error	$\pm 0.5$	$\pm 1.3$
P.E. yield variation	-1.0, +0	- 5.3, +0
Uncertainty of fluorescence yield of Xe characteristic X-ray		$\pm 11.8$
Total	-2.0, +1.1	-13.1, +11.9

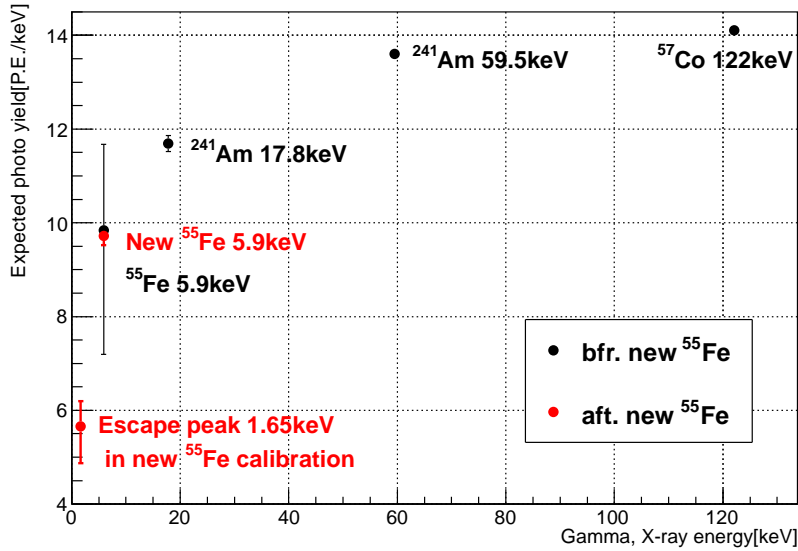


Figure 4.6: Expected photo yield[P.E./keV] when gamma-rays at each energy are generated at the detector center(without calibration source and rod). After new  $^{55}\text{Fe}$  calibration in this study, the error bar at 5.9 keV became small and 1.65 keV point was newly added.

as 5.9 keV events. Therefore, geometry effect for escape peak can be treated same as main peak and relative systematic errors for escape peak by geometry effect have same values as the main peak. Xenon fluorescence yield has about factor two difference between XMASS MC(based on Geant4) and Table of Isotopes [61]. Two fitting methods were used. One is the method to use XMASS MC output value as 1.65 keV peak and 5.9 keV peak height ratio. The other one is the method to treat

the height ratio as a fitting parameter. Mean value and uncertainty of energy scale at 1.65 keV are determined to be averaged value and the difference of these two results, respectively. This uncertainty is dominant at 1.65 keV. A new calibration source introduced in Section 4.5 emits 1.5 keV mono-energy X-ray, therefore, uncertainty from this origin would disappear.

These uncertainties in Table 4.1 are considered in Section 6.2.

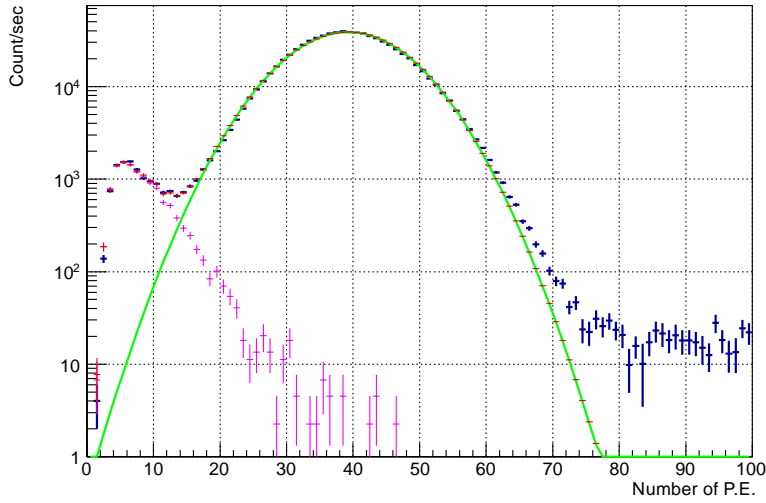


Figure 4.7: Observed P.E. distribution in the  $^{55}\text{Fe}$  calibration and MC and fitting Gaussian function. Blue, magenta points and green line represent calibration data, escape MC after energy scaling and single Gaussian for main peak, respectively. Red points represent summed up spectrum of the escape MC and single Gaussian.

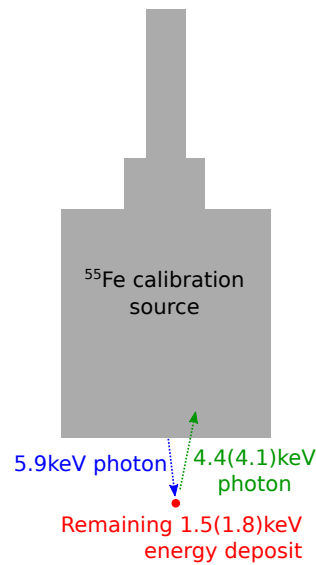


Figure 4.8: Principle of 1.5 and 1.8 keV escape peaks in the  $^{55}\text{Fe}$  calibration.

## 4.4 Energy scale

Two types of energy scales are used in this analysis.

### 4.4.1 $\text{keV}_{57\text{Co}}$

$\text{keV}_{57\text{Co}}$  is an energy scaling method obtained by dividing number of observed photo electrons(P.E.) by the P.E./keV at 122 keV from  $^{57}\text{Co}$  calibrations done in weekly.

$$\text{keV}_{57\text{Co}} = \frac{\text{observed P.E.}}{\text{P.E./keV at 122 keV}} \quad (4.1)$$

In this method, P.E. yield variation(See Section 4.6) is taken into account. Figure 4.12(a) shows a time variation of P.E. yield measured by the weekly  $^{57}\text{Co}$  calibrations.

$\text{keV}_{57\text{Co}}$  is special parameter of XMASS-I detector. However, WIMP modulation search is conducted by comparing observed dataset and WIMP modulation MC, and then the result is obtained as a WIMP–nucleon cross section. Therefore, the result can be compared with other experiments' results. WIMP model dependent analysis had been conducted with this energy scale.

### 4.4.2 $\text{keV}_{\text{ee}}$

$\text{keV}_{\text{ee}}$  is electron equivalent energy in keV obtained from gamma-ray calibrations. Usual model independent results are described by event rate [events/day/kg/ $\text{keV}_{\text{ee}}$ ]. When our result is compared with other experiments' results, the special parameter of XMASS-I detector  $\text{keV}_{57\text{Co}}$  can not be used. To compare different experiments' results, common parameter  $\text{keV}_{\text{ee}}$  should be used.

In order to convert  $\text{keV}_{57\text{Co}}$  to  $\text{keV}_{\text{ee}}$ , a conversion table was produced using optimized XMASS MC with calibration result. Figure 4.9 shows the conversion function from  $\text{keV}_{57\text{Co}}$  to  $\text{keV}_{\text{ee}}$ . In XMASS-I detector MC, 1.0, 1.65, 5.9 and 10 keV (=keV<sub>ee</sub>) gamma-rays were generated at detector center. The mean  $\text{keV}_{57\text{Co}}$  value of each energy gamma-ray event was observed and the relation between  $\text{keV}_{57\text{Co}}$  and  $\text{keV}_{\text{ee}}$  was obtained. Points at 5.9 and 1.65 keV<sub>ee</sub> represent the calibration points. Black line and light blue band represent the interpolated line and error band of the energy scale. In low-energy region less than 2 keV<sub>ee</sub>, there is a difference of about factor two between  $\text{keV}_{\text{ee}}$  and  $\text{keV}_{57\text{Co}}$  energy scales.

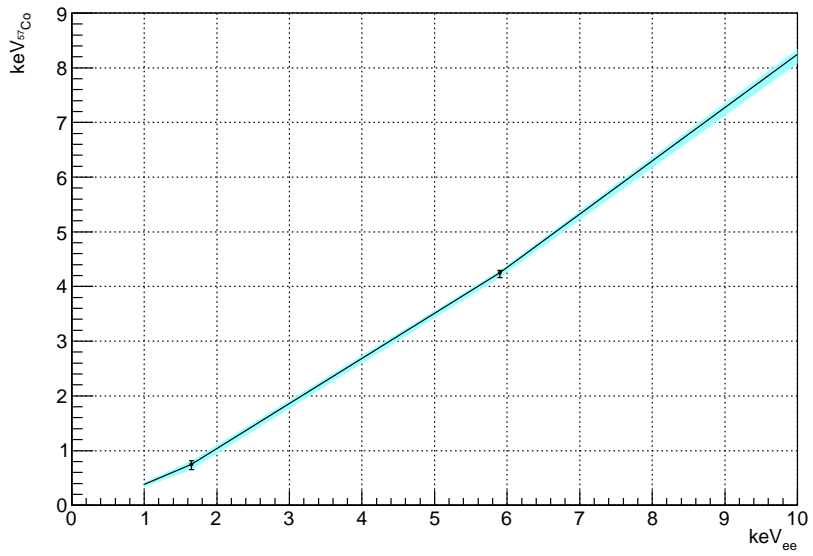


Figure 4.9: The conversion function from  $\text{keV}_{57\text{Co}}$  to  $\text{keV}_{\text{ee}}$ . Points at 5.9 and 1.65  $\text{keV}_{\text{ee}}$  represent calibration points. Black line and light blue band represent the interpolated line and error band of energy scale, respectively.

## 4.5 Development of a low-energy X-ray source

For more accurate energy calibration in low-energy region below 5.9 keV, a lower energy calibration source is required in future. There is an idea to obtain low-energy X-ray using characteristic X-rays. To generate characteristic X-rays, some types of radiations can be emitted to targets. Pure aluminum is used as a target. Aluminum emits 1.5keV characteristic X-ray. As a radioactive source,  $^{241}\text{Am}$  alpha-ray source is used. Using alpha-ray whose  $dE/dx$  is large, a thin aluminum target will be excited effectively. Figure 4.10 shows a principle of this source. This characteristic X-ray source gives independent 1.5 keV peak from other relatively higher-energy X-ray peaks. Therefore, the systematic error from the uncertainty of fluorescence yield which is dominant in 1.65 keV energy scale would disappear at 1.5 keV with this source.

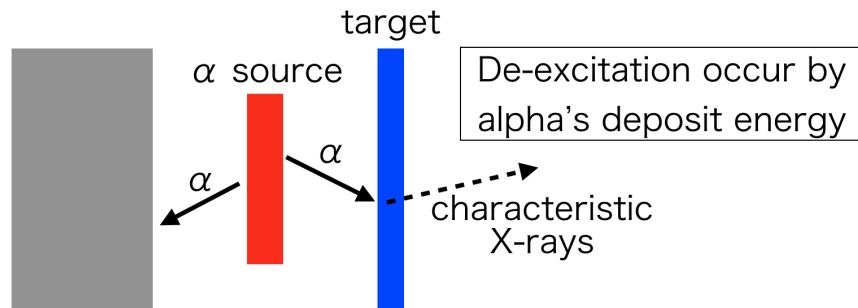


Figure 4.10: Principle of low-energy X-ray sources using alpha-ray source and characteristic X-ray.

In this study, a simple Monte Carlo simulation using Geant4 was made to confirm the feasibility of the low-energy characteristic X-ray sources. As a result, sufficient yield ( $\geq 10^{-4}$ ) and signal to background value were obtained.

A feasibility check experiment had been carried out. A  $25\mu\text{m}$  thickness pure aluminum film and a  $^{241}\text{Am}$  source were used as a target and an  $\alpha$ -ray source, respectively. Silicon detector XR-100CR was used to observe 1.5 keV X-rays. It consists of  $6\text{mm}^2 \times 500\mu\text{m}$  silicon and  $12.7\mu\text{m}$  thickness Be window. Top and bottom plots in Fig. 4.11 are energy spectra of observed data using  $^{241}\text{Am}$  only and  $^{241}\text{Am}$  with aluminum film, respectively. As a result, 1.5 keV characteristic X-ray peak had been observed in  $^{241}\text{Am}$  with aluminum film data. An unexpected peak around 2.2 keV was found in the top plot. This is thought to be due to the  $^{241}\text{Am}$  source housing, and it was disappeared with an existence of the Aluminum film. No effect was seen in the bottom plot.

Design of the source housing, leak check and pressure test using dummy source had been done. Now an actual source is being prepared. After making and safety check, XMASS-I detector calibration will be done with the source.

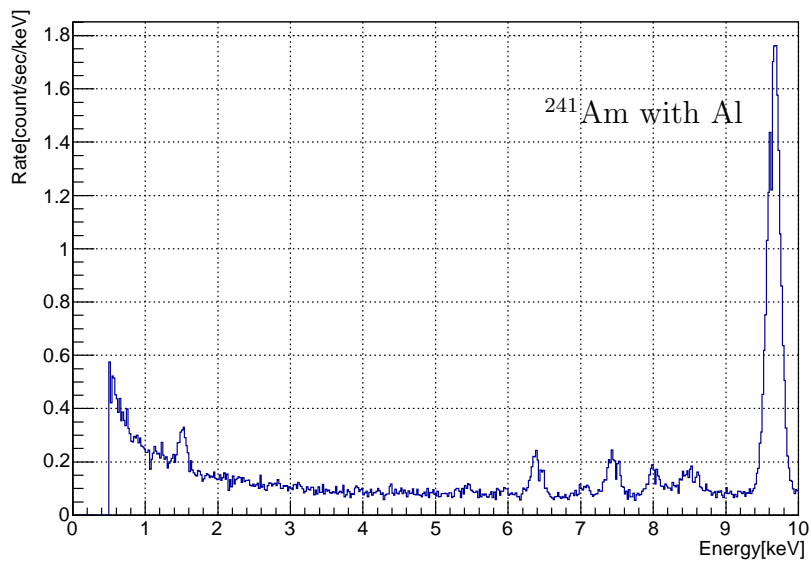
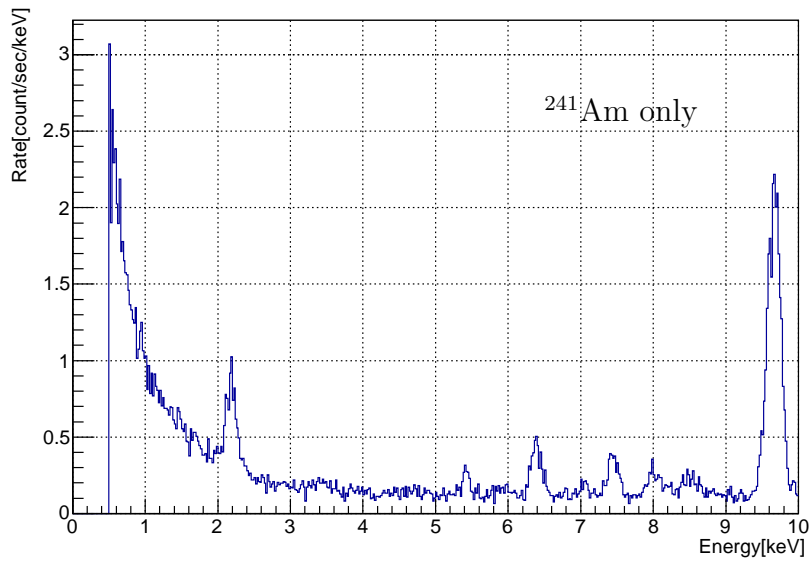


Figure 4.11: Energy spectrum of only  $^{241}\text{Am}$  (top). Energy spectrum of Al with  $^{241}\text{Am}$  measured with XR-100CR (bottom). A 1.5 keV peak can be seen in the bottom plot.

## 4.6 Xe absorption length

Xe absorption length(ABSL) largely affects to the energy response of the detector. Photo electron (P.E.) yield P.E./keV of the detector is obtained from 122 keV peak in  $^{57}\text{Co}$  calibration data. We carried out  $^{57}\text{Co}$  calibration weekly with inner calibration system to monitor P.E. yield of the detector. Figure 4.12(a) shows the time variation of the P.E. yield of  $^{57}\text{Co}$ . The P.E. yield had changed as a function of time. A sudden drop was observed around 230 days. An unexpected power failure had occurred at that time. According to study using the MC simulation, the P.E. yield changes are described by changing xenon ABSL parameter. This reason would be explained by impurities in xenon. The P.E. yield had recovered after xenon purification in gas phase (around 360days). Now xenon gas is continuously circulated with purification. Time variation of ABSL is shown in Fig. 4.12(b). Fig. 4.12(a) and 4.12(b) are correlated well. Fig. 4.12(c) shows time variation of relative scintillation light yield considering ABSL variation. The intrinsic light yield is stable within  $\pm 2\%$  when ABSL change was considered. In modulation analysis, this residual P.E. yield variation in Fig. 4.12(c) is taken into account as a systematic error.

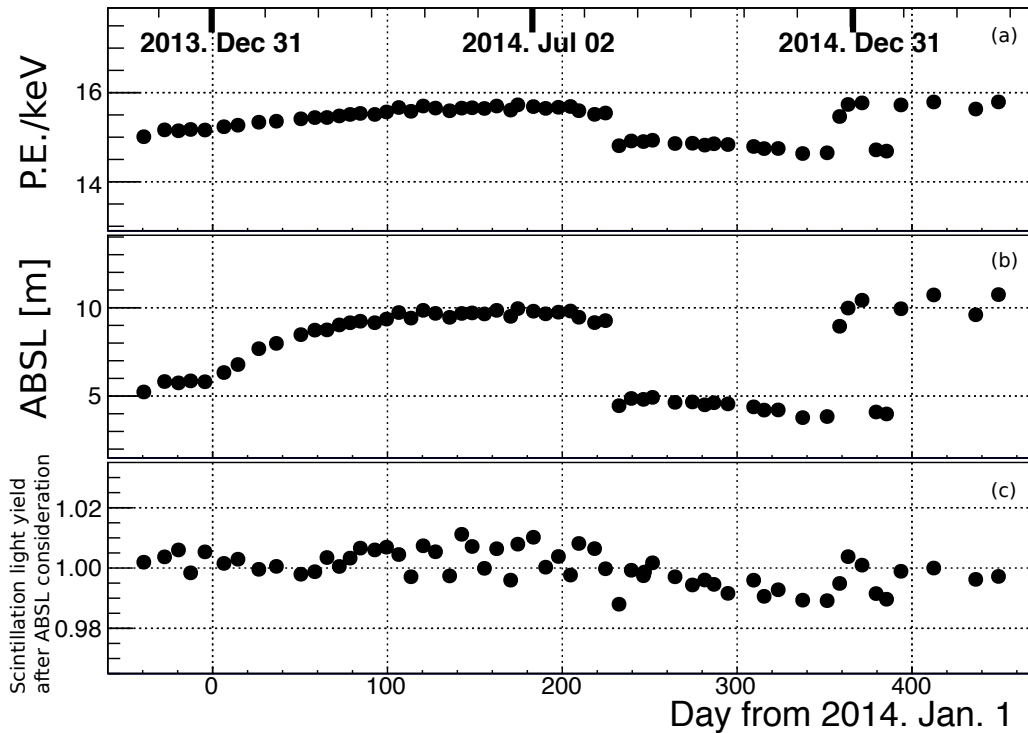


Figure 4.12: Photo electron yield variation.

# Chapter 5

## Dataset and event selection

### 5.1 Dataset

Continuous data taking had been carried out since November 2013. Data taken during 504.2 calendar days (Nov. 11<sup>th</sup> 2013 - Mar. 29<sup>th</sup> 2015) were used for this analysis. Figure 5.1 shows a cumulative livetime from the start of the data taking. Blue dashed line shows cumulative calendar days and black solid line shows cumulative livetime. X-ray, gamma-ray, neutron, LED and regular  $^{57}\text{Co}$  calibration data were taken in this period. These calibration data and data during 10 days after the neutron calibrations are not used in analysis. Also, the data periods with large PMT noise, unstable condition of data acquisition system (abnormal power supply etc.) and abnormal trigger rate are removed from the dataset. The total livetime is 359.2 days. We use 832 kg liquid xenon as the target volume. The total exposure is 0.82 ton-year.

### 5.2 WIMP signal simulation

Assuming a Maximilian dark matter velocity ( $v$ ) distribution with typical speed  $v_0 = 220$  km/s described in Equation (5.1), MC simulation data for WIMP signal in XMASS-I detector following [33] were prepared.

$$f(v, v_E) = e^{-(v+v_E)^2/v_0^2} \quad (5.1)$$

The simulated WIMP properties and detector conditions are listed in Table 5.1. Uniformly distributed WIMP- $^{132}\text{Xe}$  nuclear scattering is assumed. The Earth's velocity relative to our galaxy  $v_E$  is selected to be  $232 + 15 \sin 2\pi(t - t_0)/T$  km/s taking annual modulation effect into account. Here,  $t$ ,  $t_0 = 152.5$  and  $T = 365.24$  represents time, phase and period, respectively. Two escape velocities of our galaxy  $v_{esc} = 650$  and  $544$  km/s are prepared and  $v_{esc} = 650$  km/s is basically used. A local dark matter density  $\rho(r) = 0.3$  GeV/cm<sup>3</sup> is used.  $L_{eff}$  which is explained in Section 3.3.3 selected to be mean value and  $\pm 1\sigma$ . To obtain conservative limit,  $-1\sigma$  of  $L_{eff}$  in Fig. 3.9 was used.

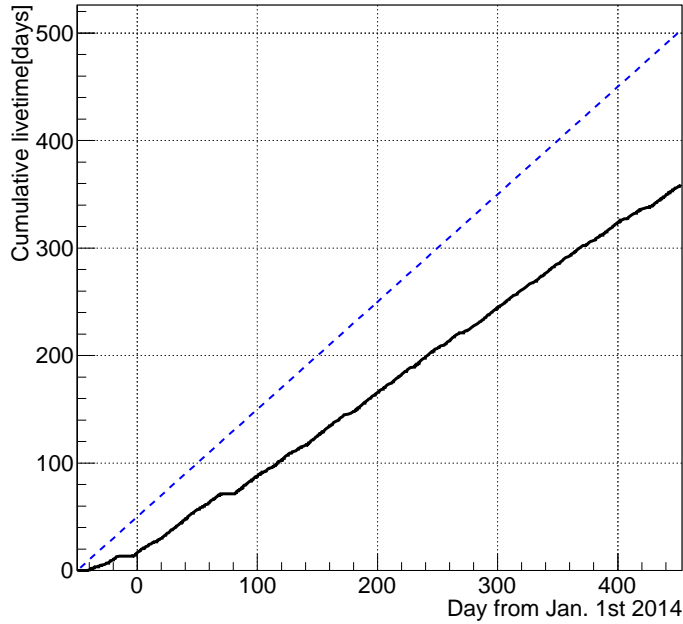


Figure 5.1: Cumulative livetime. Blue dashed and black solid lines represent cumulative calendar days and cumulative livetime, respectively.

### 5.3 Event selection

The following event selections are applied to the observed data in order to reduce background events. The same selection were applied to the simulated WIMP signals in order to evaluate the selection efficiency.

#### Trigger cut

In addition to ID, XMASS-I detector has OD to observe Cherenkov events in the water tank occurred by cosmic-ray muons. In order to reject events caused by cosmic-ray muons, events triggered with OD PMTs are rejected.

#### Nhit cut

Events triggered by less than 4 ID PMT hits(Nhit) are rejected to remove electronic noise events. 4 ID hit corresponds to about 0.3 keV<sub>57Co</sub> and 0.8 keV<sub>ee</sub>. Figure 5.2 shows Nhit distribution as a function of energy after the Trigger cut.

#### $\Delta T$ cut

To remove the events caused by the after pulses of PMTs, the time difference between an event and the previous event ( $\Delta T$ ) is used for this selection. The events with small  $\Delta T$  (<10ms) are rejected. Figure 5.3 shows  $\Delta T$  distribution of observed data after Nhit cut.

#### Time RMS cut

This cut removes further electronic noise events. Events which has large RMS

Table 5.1: WIMP properties and detector condition in MC simulation.

Interaction	WIMP- <sup>132</sup> Xe nuclear recoil
Mass[GeV]	6, 7, 8, 9, 10, 11, 12, 13, 14, 18 and 20
Season	Jun. 2 <sup>nd</sup> , Dec. 4 <sup>th</sup> and Average
$v_0$	220 [km/s]
$v_{esc}$	650 and 544 [km/s]
$\rho(r)$	0.3 [GeV/cm <sup>3</sup> ]
$L_{eff}$	mean, $\pm 1\sigma$
Xe absorption length	500 – 1100 cm
Xe scattering length	52 cm

of hit timing of each PMT hit ( $>100\text{ns}$ ) are rejected. Figure 5.4 shows the timing RMS distribution as a function of energy after  $\Delta T$  cut.

### Cherenkov cut

This cut removes events occurred by Cherenkov light generated in the PMT windows. Those satisfy Equation (5.2) are selected.

$$\frac{\text{number of PMT hits in the first 20 ns}}{\text{number of PMT hits in whole time range (Nhit)}} \leq 0.6 \quad (5.2)$$

Cherenkov lights are emitted immediately unlike scintillation lights. Therefore the events with high ratio of number of PMT hits in the first 20 ns to that total PMT hits are rejected. Events with this parameter  $\leq 0.6$  are selected. Figure 5.5 shows the Cherenkov cut parameter distribution as a function of energy.

### Maxpe/totalpe cut

”Maxpe” is defined as the number of P.E. of a PMT which had obtained maximum P.E. value in an event. On the other hand, ”totalpe” is defined as sum of the number of P.E. of all the hit PMTs in an event. ”Maxpe” / ”totalpe” ratio will be large when the events occurred in front of a PMT window. Such events will be removed by cutting high ”Maxpe/totalpe” events. The cut criterion was designed to keep 50% of uniform 20 GeV WIMP signal MC events. Figure 5.6 shows the ”Maxpe/totalpe” distribution as a function of energy.

Figure 5.7 and 5.8 show the observed energy spectra after each event selection and remaining ratio relative to the original dataset in  $\text{keV}_{57\text{Co}}$  and  $\text{keV}_{\text{ee}}$ . After these event selections, the final sample is made. Table 5.2 shows the remaining event rates after each cut of observed dataset and the relative rate of the remaining events to the original dataset. Figure 5.9, 5.10 and 5.11 represent the spectra and remaining ratio after each cut for 6, 10 and 20 GeV WIMP events, respectively.

Table 5.2: Integrated remaining event rate in 0.5–5 keV<sub>57Co</sub> after each cut of observed dataset and the rate of remaining ratio after cuts relative to the original dataset. Expected relative rates from WIMP MC events are also shown.

Cut criteria	Remaining event rate of observed dataset [events/day/kg /0.5–5keV <sub>57Co</sub> ]	Relative rate of remaining events to event rate after Trigger cut. (0.5–5keV <sub>57Co</sub> )			
		Observed dataset	6 GeV WIMP	10 GeV WIMP	20 GeV WIMP
Trigger and Nhit cut	1077.8	1.0	1.0	1.0	1.0
$\Delta T$ cut	940.8	0.87	1.0	1.0	1.0
Time RMS cut	901.1	0.84	1.0	1.0	1.0
Cherenkov cut	51.2	0.048	0.55	0.59	0.66
Final sample (Maxpe/totalpe cut)	10.98	0.010	0.18	0.28	0.35

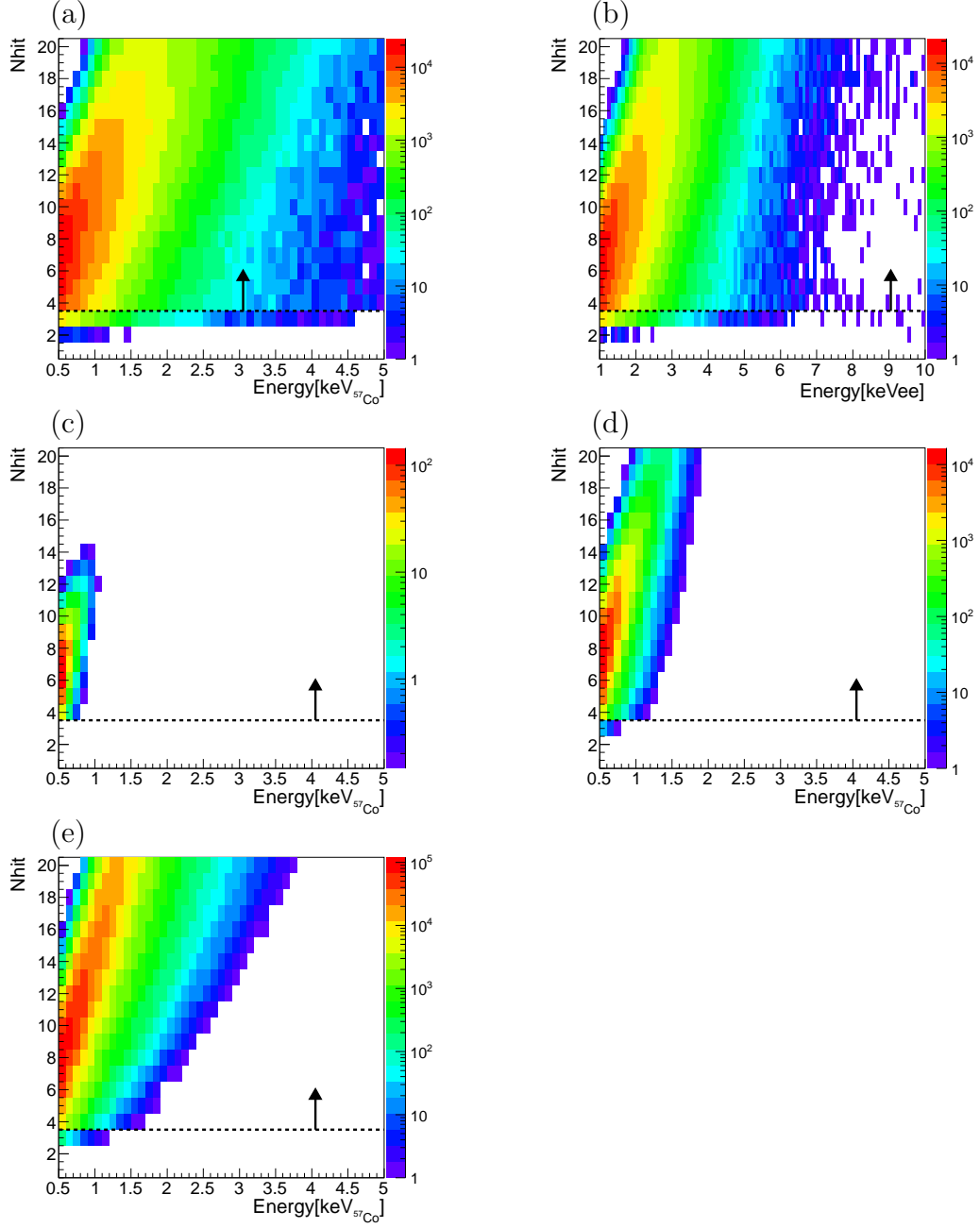


Figure 5.2:  $N_{hit}$  vs energy distribution after ID trigger cut. (a), (b), (c), (d) and (e) are observed data in  $\text{keV}_{57\text{Co}}$  and  $\text{keV}_{ee}$  and 6, 10, 20 GeV WIMP MC in  $\text{keV}_{57\text{Co}}$ , respectively. Black line shows the cut point.

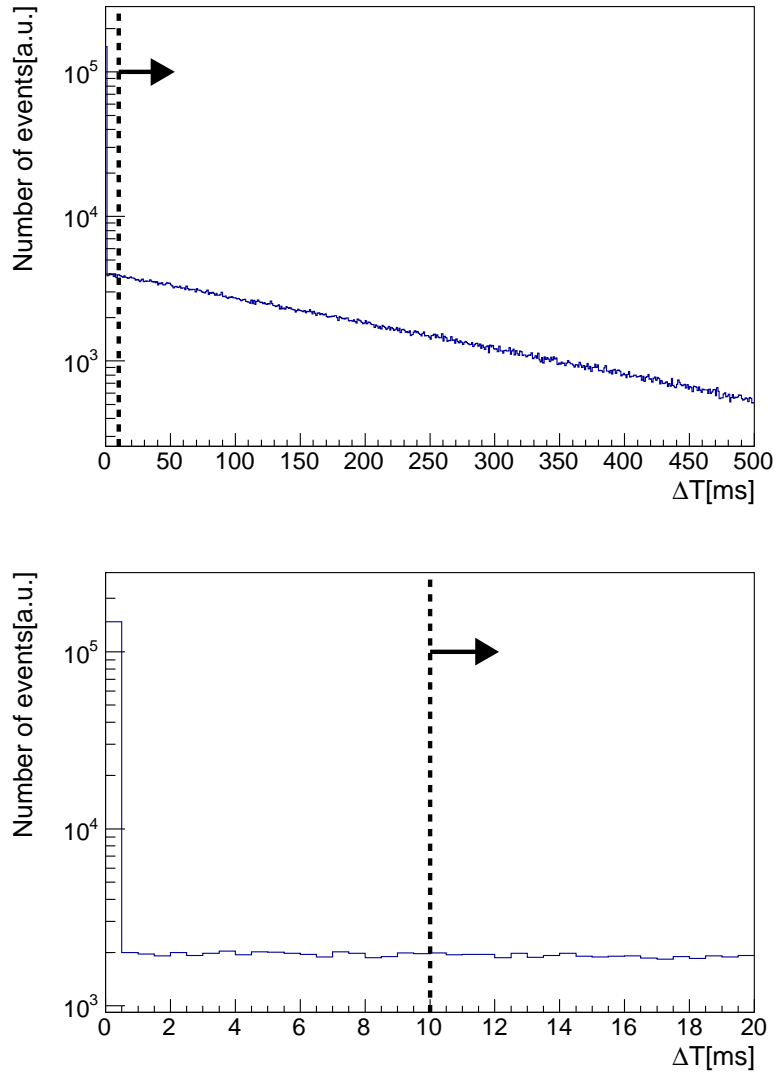


Figure 5.3:  $\Delta T$  distribution after  $N_{hit}$  cut. Black line shows the cut point. The events with  $\Delta T < 10$ ms are rejected. Bottom figure is zoomed up one. This distribution is same for both  $keV_{e_e}$  and  $keV_{^{57}Co}$  energy scale.

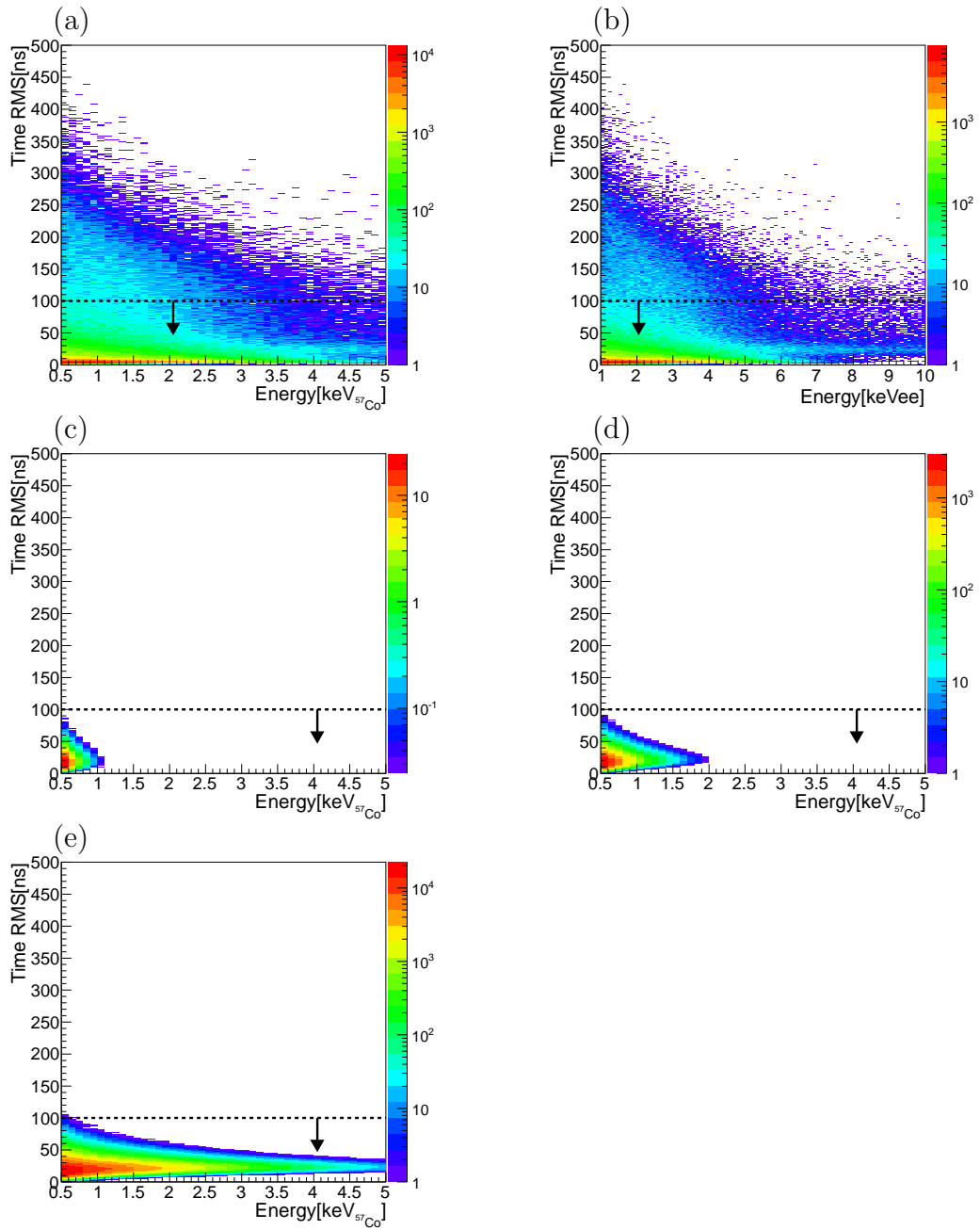


Figure 5.4: Time RMS distribution as a function of energy after  $\Delta T$  cut. Black line is the cut point. The definitions of each plot are same as Fig. 5.2.

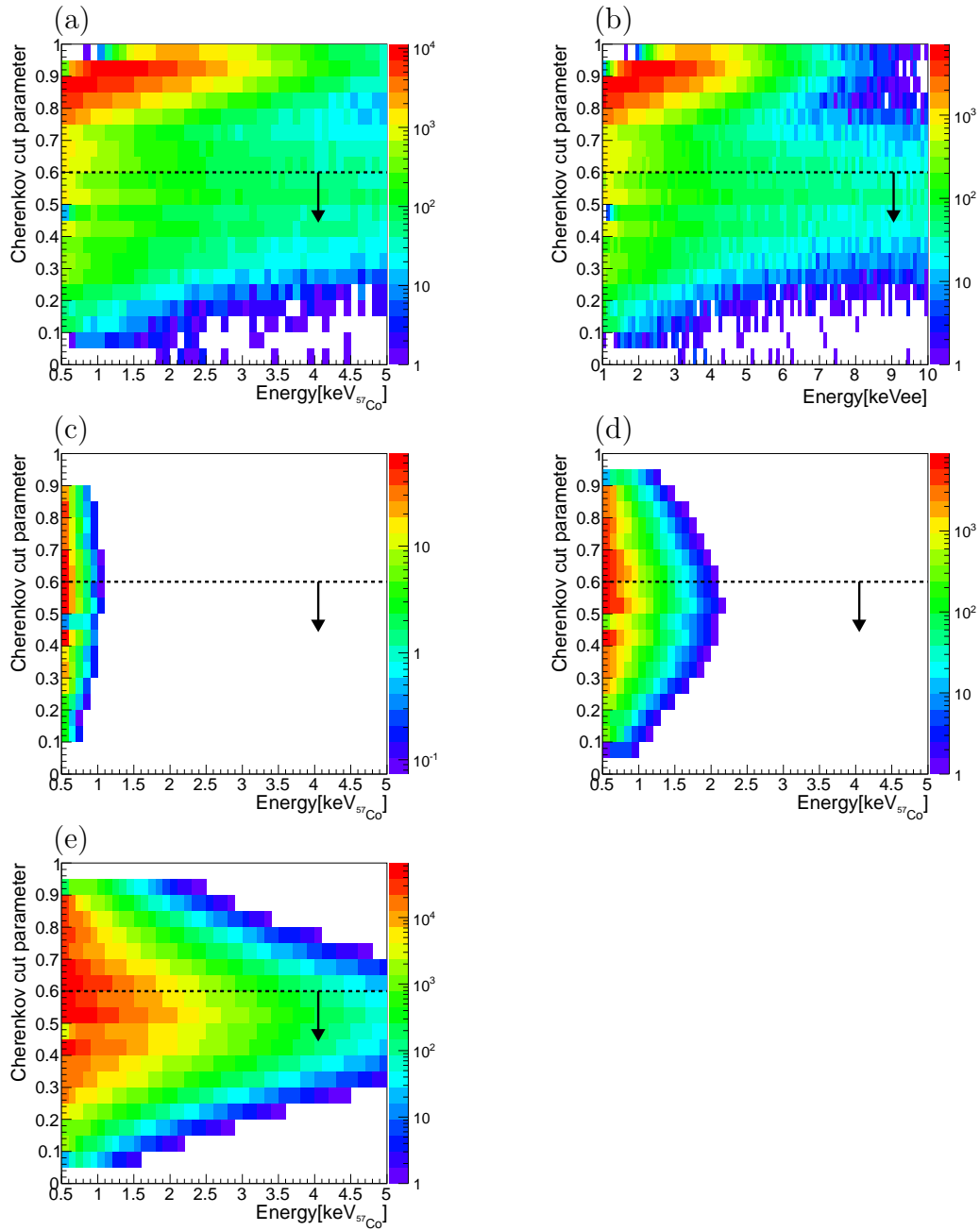


Figure 5.5: Cherenkov cut parameter distribution as a function of energy after Time RMS cut. Black line is the cut point. Allows represent the region of selected events. The definitions of each plot are same as Fig. 5.2.

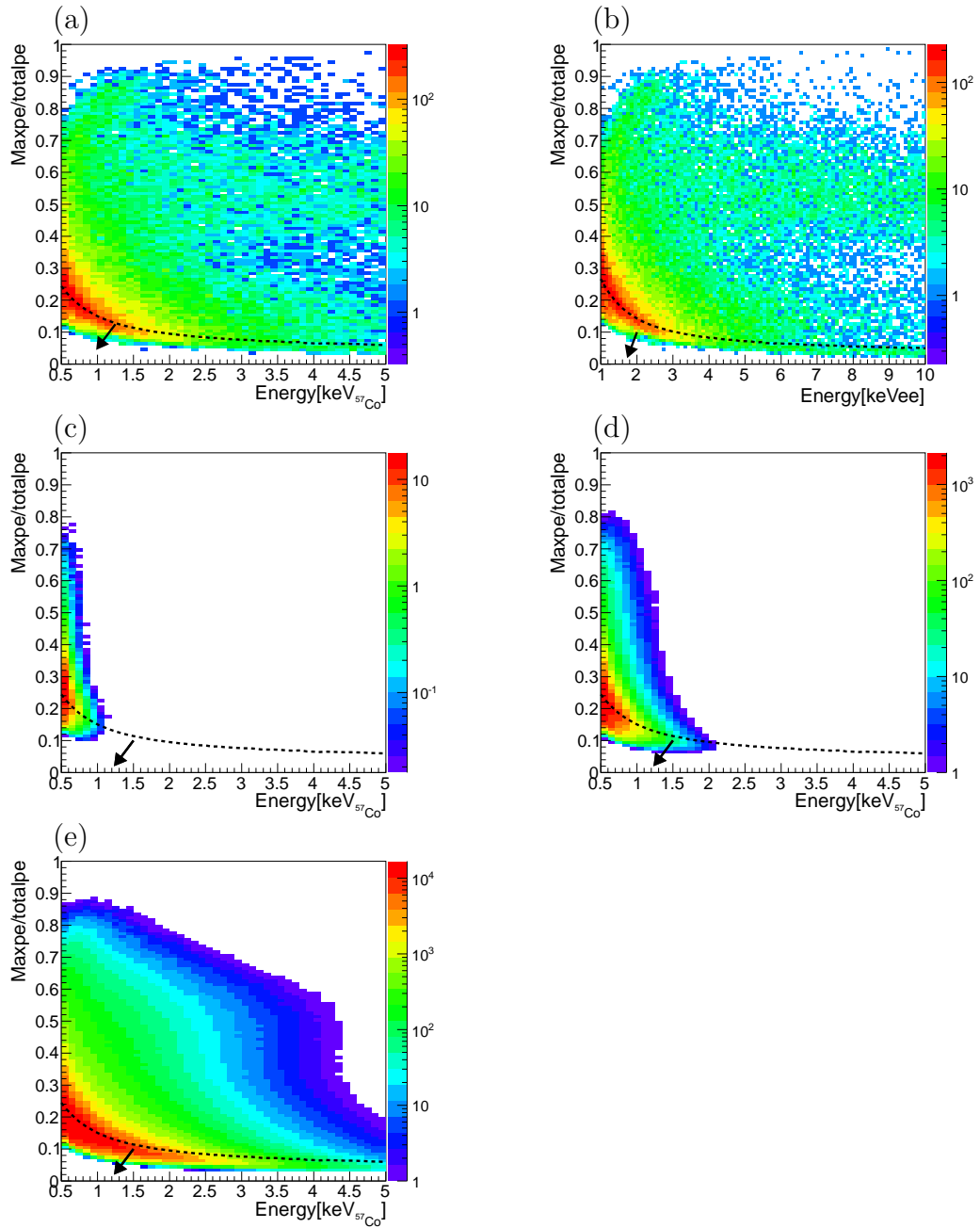


Figure 5.6: "Maxpe/totalpe" distribution as a function of energy after Cherenkov cut. Black line is the cut point. The definitions of each plot are same as Fig. 5.2.

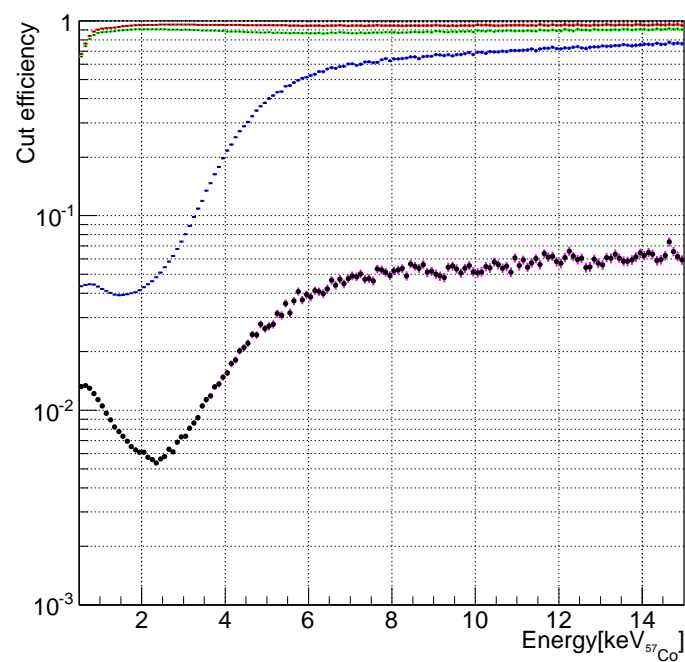
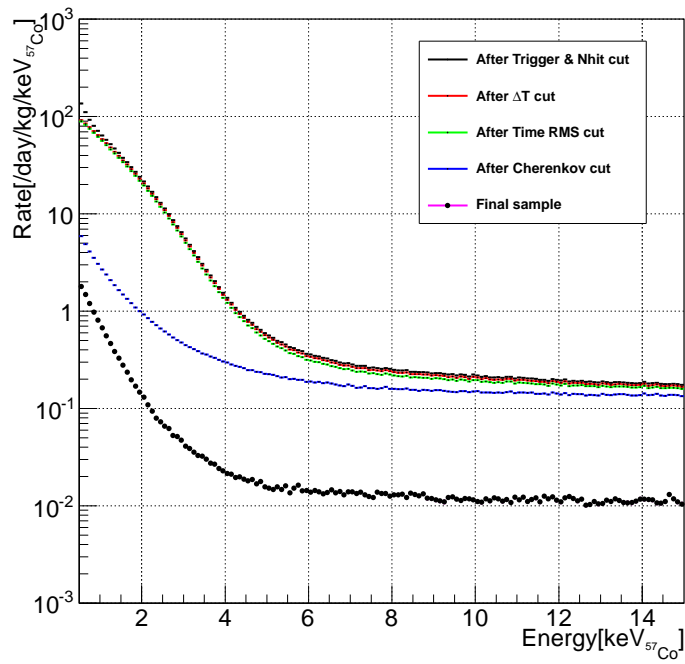


Figure 5.7: Energy spectra in  $\text{keV}_{57\text{Co}}$  after each cut (top) and remaining ratio relative to the original dataset.

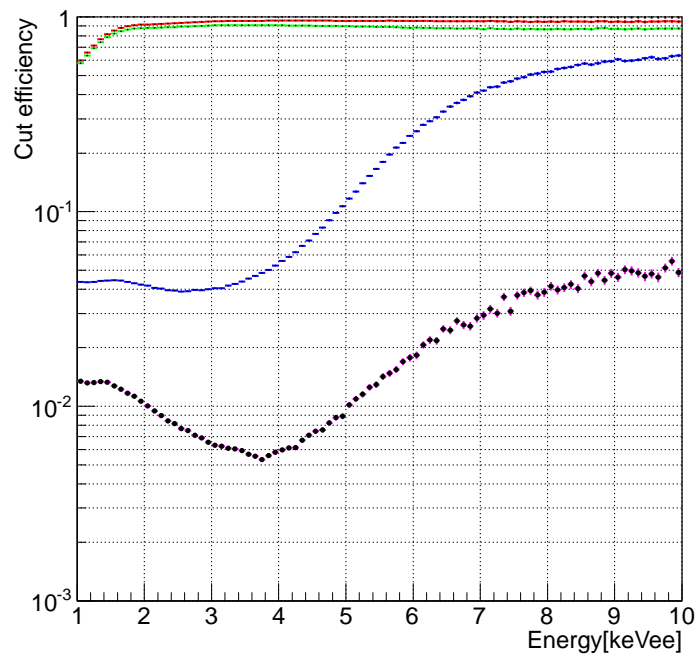
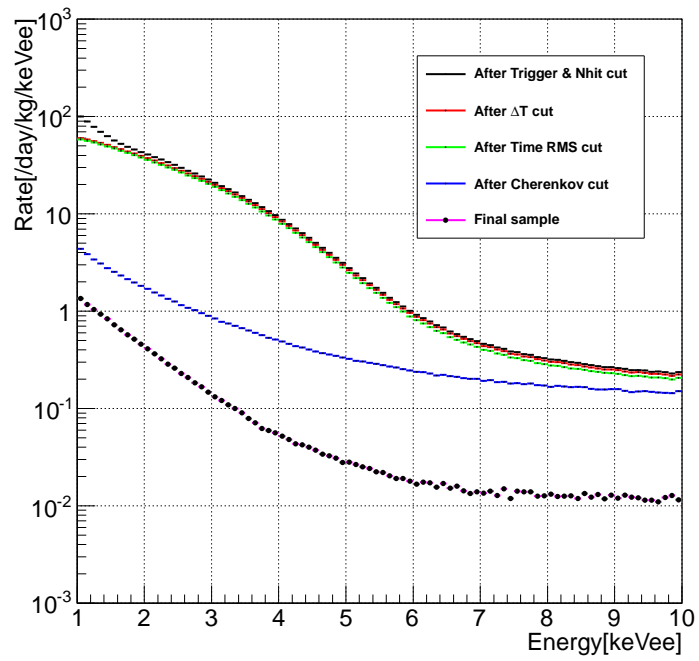


Figure 5.8: Energy spectra in  $\text{keV}_{ee}$  after each cut (top) and remaining ratio relative to the original dataset.

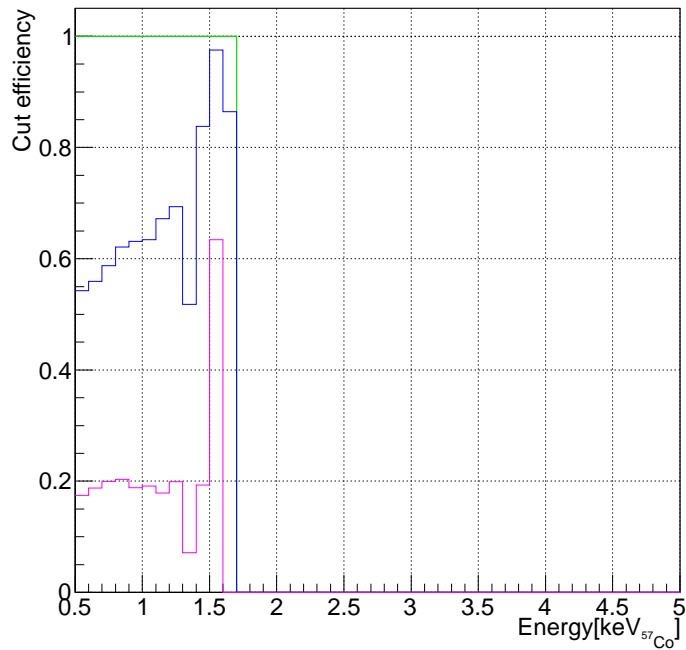
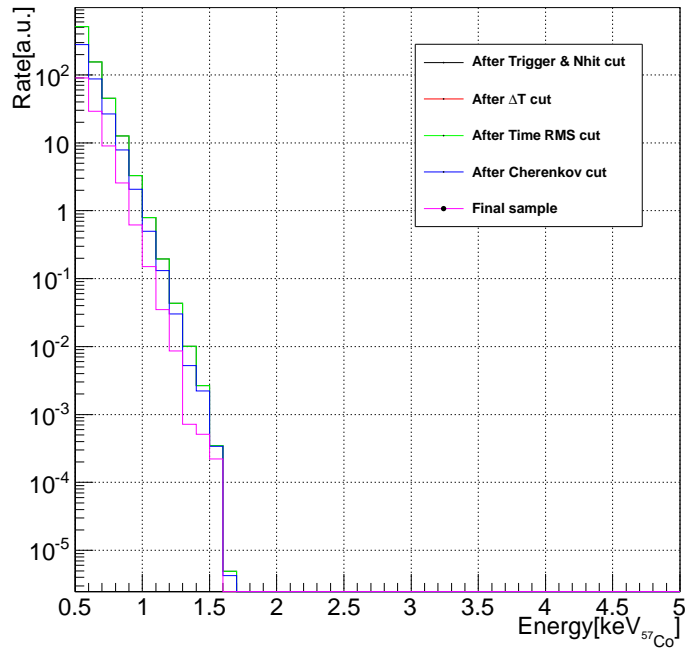


Figure 5.9: Energy spectra after each cut of 6 GeV WIMP MC and the rate of remaining ratio after cuts relative to the original samples. Here, the lines of "After Trigger and Nhit cut", "After  $\Delta t$  cut" and "After Time RMS cut" are almost overlapped.

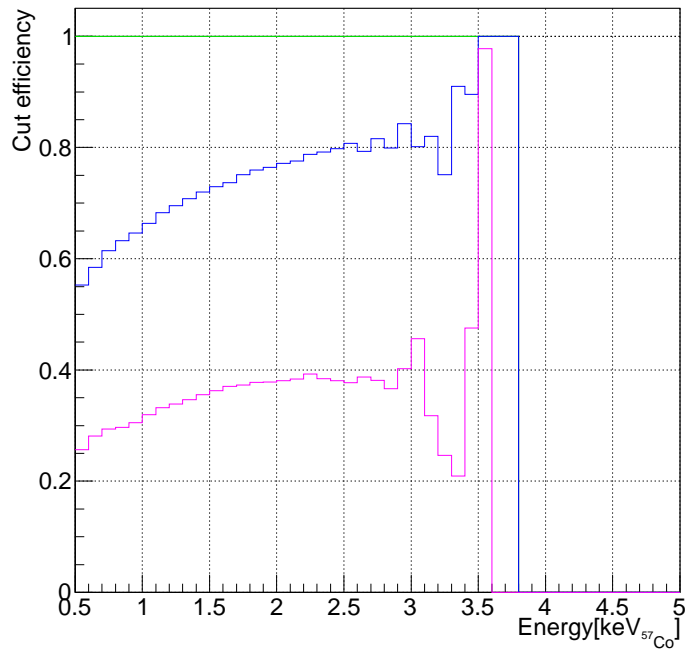
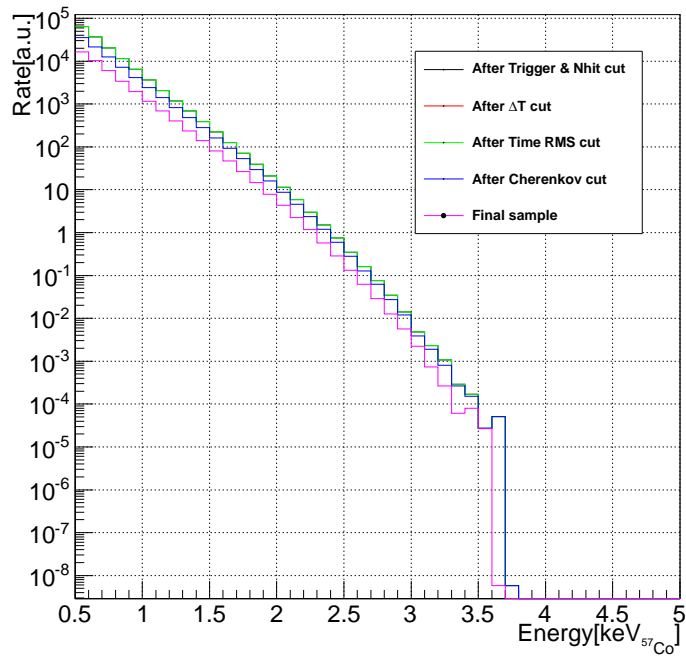


Figure 5.10: Energy spectra after each cut of 10 GeV WIMP MC and the rate of remaining ratio after cuts relative to the original samples. Here, the lines of "After Trigger and Nhit cut", "After  $\Delta t$  cut" and "After Time RMS cut" are almost overlapped.

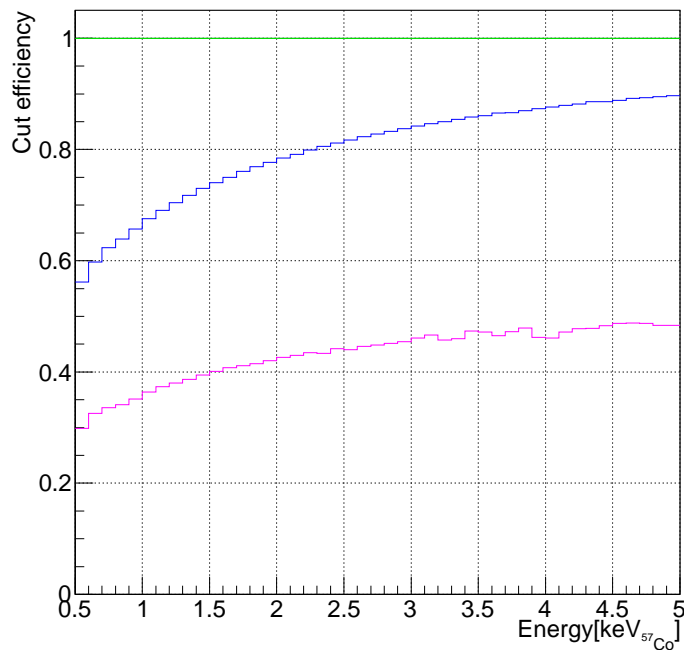
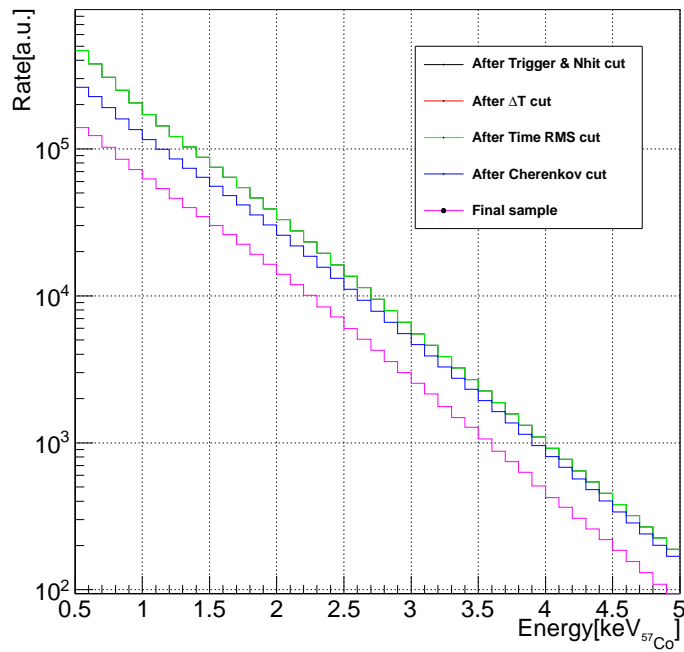


Figure 5.11: Energy spectra after each cut of 20 GeV WIMP MC and the rate of remaining ratio after cuts relative to the original samples. Here, the lines of "After Trigger and Nhit cut", "After  $\Delta t$  cut" and "After Time RMS cut" are almost overlapped.

# Chapter 6

## Systematic uncertainties

Systematic uncertainties in the modulation analysis are summarized in Table 6.1.

### 6.1 P.E. yield change

The P.E. yield(ABSL) variation affects the efficiencies of the cuts due to not only the threshold but also the position dependence of detector response and the shape of energy spectra. Those uncertainties are taken into account as a systematic error for the different energy ranges in 0.5–1.0 keV<sub>57Co</sub> (1.0–2.0 keV<sub>ee</sub>) and over 1.0 keV<sub>57Co</sub> (2.0 keV<sub>ee</sub>).

Changing ABSL, WIMP signal and dominant background MC were made to estimate the cut efficiency change. Figure 6.1 shows relative cut efficiencies to the 8 m ABSL MC. Each line represent WIMP signal and background MC. Top plot is for 0.5–1.0 keV<sub>57Co</sub>, bottom one is for over 1.0 keV<sub>57Co</sub>. Black lines in each plot represent 6 and 8 GeV WIMP MC for < 1 keV<sub>57Co</sub> and > 1 keV<sub>57Co</sub>, respectively. In the energy region of > 1 keV<sub>57Co</sub>, the statistics of 6 GeV WIMP MC was very small, and then 8 GeV WIMP MC was used. Blue, green, red and magenta lines represent 20 GeV WIMP, 100 GeV WIMP, <sup>210</sup>Pb in PMT Aluminum ring and <sup>238</sup>U in PMT Aluminum ring, respectively. The maximum and minimum values at each ABSL are treated as maximum and minimum uncertainties. Their mean value is determined as center value. The center value and maximum and minimum lines are shown in Figure 6.2 by solid and dotted lines. For keV<sub>ee</sub> analysis, plots of relative cut efficiencies for 1.0–2.0 keV<sub>ee</sub> and over 2.0 keV<sub>ee</sub> were also prepared. Instead of 8 GeV WIMP MC, 9 GeV WIMP MC was used for over 2.0 keV<sub>ee</sub> energy region to obtain sufficient statistics.

This uncertainty is the largest systematic error, and introduced as  $K_{i,j}$  into  $\chi^2$  definition in Section 7.1.

### 6.2 Uncertainty of energy scale

Uncertainty of energy scale also affects time variation plot. When energy scale is changed with maximum/minimum uncertainty in Figure 4.9, event rate of each bin will be also changed. This variation is treated as a systematic error, and introduced

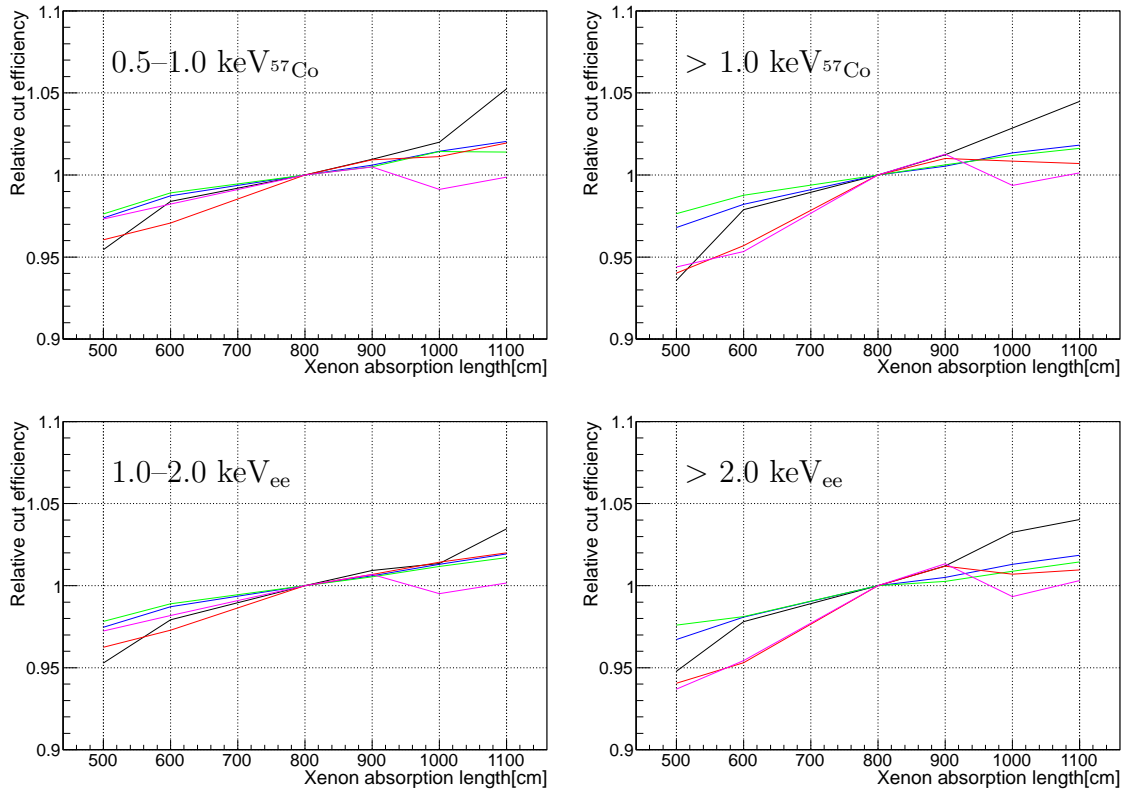


Figure 6.1: Relative cut efficiency to the absorption length=8m data for each energy region. Black, blue, green, red and magenta lines represent 6(8,9) GeV WIMP for  $< 1 \text{ keV}_{57\text{Co}}$  and  $< 2 \text{ keV}_{ee}$  ( $> 1 \text{ keV}_{57\text{Co}}$ ,  $> 2 \text{ keV}_{ee}$ ), 20 GeV WIMP, 100 GeV WIMP,  $^{210}\text{Pb}$  in PMT Aluminum seal and  $^{238}\text{U}$  in PMT Aluminum seal, respectively.

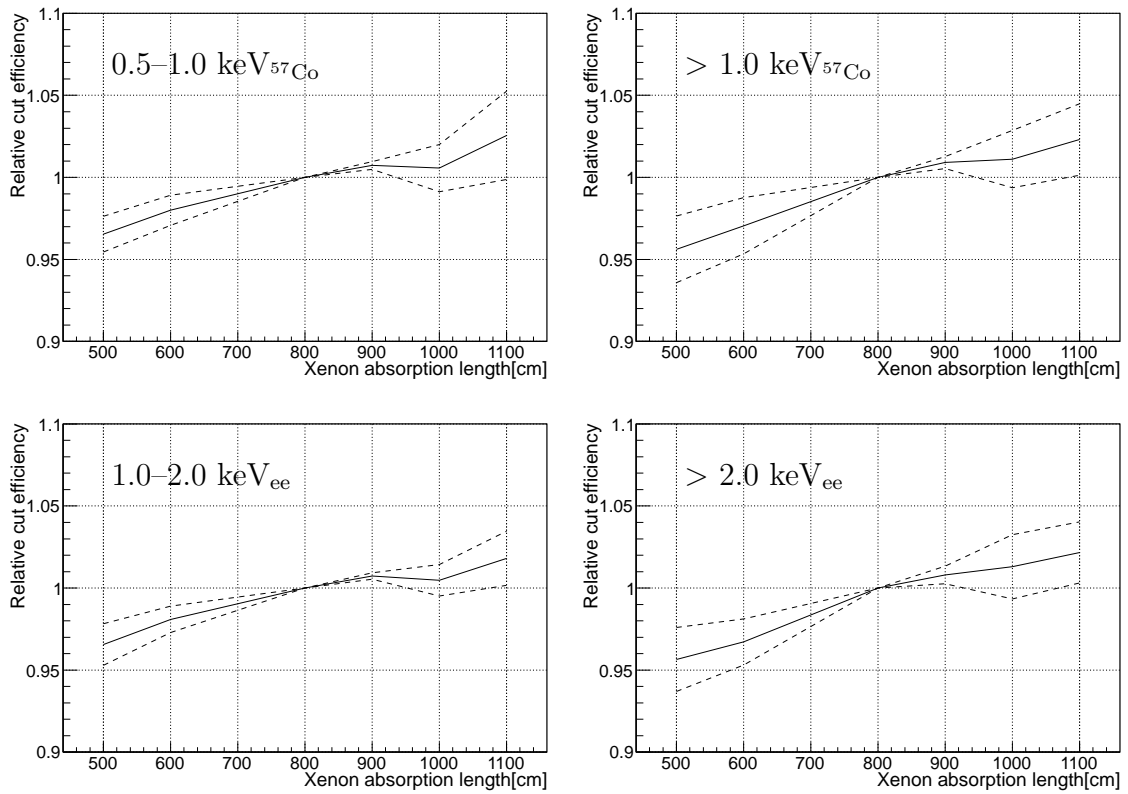


Figure 6.2: Relative cut efficiency to the absorption length=8m data for each energy region. Center, maximum and minimum values are described with solid and two dotted lines.

as  $L_{i,j}$  into  $\chi^2$  definition in Section 7.1. Unlike as  $K_{i,j}$  which has positive and negative values for each time bin,  $L_{i,j}$  values have common sign for whole bins and their absolute values are not different largely between different time bins. Therefore, effect to amplitude fitting by  $L_{i,j}$  is smaller than that of  $K_{i,j}$ . The  $L_{i,j}$  values for each time and energy bin can be seen in Figure 7.3 and 7.4.

## 6.3 FADC self calibration

The third largest contribution to the systematic uncertainty comes from the gain instability of the FADCs (CAEN V1751) which record the wave form of the PMT signals. This happened only during April 2014 and September 2014 due to the different initialization method of FADCs and it is estimated as 0.3% uncertainty in energy scale. This effect is also taken into account by adding to the statistical error in quadrature.

## 6.4 Livetime calculation

To calculate livetime of each run, two methods had been used. One is using trigger information accumulating dead time due to several vetoes. Start and end time in terms of trigger clock count were recorded. For each event, 12  $\mu\text{sec}$  length trigger vetoes were accumulated as dead time. The other one is counting GPS 1 PPS (pulse per second) trigger. GPS 1 PPS trigger was mixed into data taking. The number of 1 PPS events recorded in observed data was counted and is the livetime in the unit of second. The same vetoes as above was applied. Livetime by this method was used in this analysis. Livetime calculated by these two methods agree within a 0.2 % level.

## 6.5 External parameters

In WIMP modulation MC, two escape velocity of our galaxy  $v_{esc} = 650$  and  $544$  km/s is prepared and  $v_{esc} = 650$  km/s is basically used.

A local dark matter density  $\rho(r) = 0.3 \text{ GeV}/\text{cm}^3$  is used.  $L_{eff}$  represents the liquid xenon scintillation efficiency of nuclear recoil relative to 122 keV gamma-ray and selected to be mean and  $\pm 1\sigma$ . To obtain conservative limit,  $-1 \sigma$  of  $L_{eff}$  was used.

## 6.6 Background

### 6.6.1 Cosmic-ray muon

Muons coming into the water tank are one of possible background events caused by cosmic-ray muons. On timing background can be removed by Trigger cut. Whatever signals are generated by gamma-ray, neutron or muon decay, short delayed signals ( $\Delta t < 10\mu\text{sec}$ ) are in the same events and can be removed. Delayed signal ( $10\mu\text{sec} <$

$\Delta t$ ) made by spallation in Cu and Xe was also estimated. ID + OD trigger rate is 0.0014 Hz in XMASS-I dataset. Assuming extreme case, if all the muon passing through or stopping at the Cu or Xe makes the delayed gamma-ray or neutron events by the spallation, the event rate would be 0.0014 Hz. 0.0014 Hz corresponds to 0.14 events/day/kg (not /keV but /detector) and sufficiently smaller than  $\sim 1$  events/day/kg/keV<sub>ee</sub> in this analysis.

Neutrons from mine rock made by muons also have possibility to be background. Referring [63], neutron flux at Yangyang laboratory (1800 m w.e.) which is shallower than Kamioka observatory (2700 m w.e.) are  $10^{-8}$  and  $10^{-9}$  neutrons/cm<sup>2</sup>/sec for  $E < 10$  MeV and  $E > 10$  MeV, respectively. As an extreme case, here we assume the neutron flux around XMASS detector is  $10^{-8}$  neutrons/cm<sup>2</sup>/sec. The XMASS water tank surface area is  $\sim 4.5 \times 10^6$  cm<sup>2</sup>. Therefore,  $10^{-8} \times (4.5 \times 10^6) \times 86400 = \sim 3.9 \times 10^3$  neutrons/day/tank is expected. From MC simulation, 2m water reduce neutrons( $E < 10$  MeV) to be less than  $10^{-7}$ , and then  $(3.9 \times 10^3) \times 10^{-7} / 832\text{kg} = 4.7 \times 10^{-7}$  events/day/kg neutrons are expected.  $10^{-9}$  neutrons( $E > 10$  MeV)/cm<sup>2</sup>/sec corresponds to 39 neutrons/day/watertank. Assuming extreme case, if all these neutrons makes events triggered in ID only, the event rate would be  $39/832\text{kg} = 0.05$  events/day/kg (not /keV buy /detector) and it is negligible comparing with the event rate of the final sample.

## 6.6.2 Rn in water

Using radon detector for watertank described in section 3.4.1, radon concentration in purified water in the tank has been monitored continuously with a special radon assay device since March 2014 [60]. Figure 3.12 shows time variation of radon concentration in XMASS purified water. Maximum <sup>222</sup>Rn concentration was  $(1.4 \pm 0.2) \times 10^2$  mBq/m<sup>3</sup>. It corresponds to  $(1.4 \pm 0.2) \times 10^{-5}$  events/kg/day/keV in XMASS-I detector. The background level of the current assay device is about 10 mBq/m<sup>3</sup>. It corresponds to  $(1.4 \pm 0.2) \times 10^{-6}$  events/kg/day/keV in XMASS-I detector. The absolute value of the maximum amplitude of time variation as a result of model independent modulation analysis is about 0.02 events/day/kg/keV. No effect from Rn in water is expected to annual modulation analysis.

## 6.6.3 Rn in LXe

<sup>222</sup>Rn is emanated from detector materials and distributed in LXe. The signal from decay of radon daughter (<sup>214</sup>Pb) may become the mimic of DM signal in several keV energy region. The concentration of radon in LXe is estimated by radon daughter <sup>214</sup>Bi-<sup>214</sup>Po signal coincidence analysis. Figure 6.3 shows the long term monitor of radon concentration in LXe from 2013 Nov. to 2015 March. The radon concentration in LXe is stable as 7.7 mBq before March 2015. The signal expected in energy region less than 10 keV from radon daughter <sup>214</sup>Pb is about  $10^{-4}$  events/day/kg/keV. This value is enough smaller than the one of analyzed dataset in less than 10 keV. Xenon gas was circulated since March 2015. After this circulation, radon concentration is increased to about 11 mBq. This amount of change for radon concentration is negligible for annual modulation analysis.

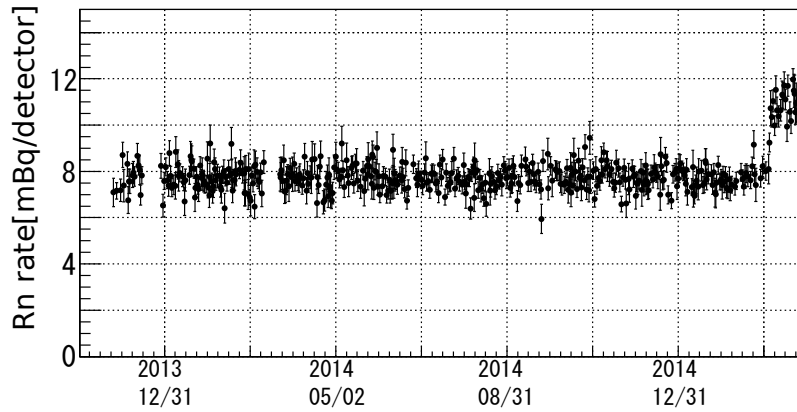


Figure 6.3: The long term monitor of radon concentration in LXe from November 2013 to March 2015. Black point indicates the radon concentration in LXe of detector. The change in March 2015 is caused by the xenon gas circulation.

## 6.7 Other systematic errors

Uncertainty of PMT gain table obtained from LED calibration is less than 0.3%. The effect from trigger stability is within 0.022 % in event rate in 0.5–0.6 keV<sub>57Co</sub> and it is much less than other systematic error sources.  $\Delta T$  offset calibration is also much less than others. These effects are found to be negligible.

Table 6.1: Systematic uncertainties in modulation analysis.

Items	Relative uncertainty
P.E. yield change	Correlated error for cut efficiency $\sim \pm 2.5$ % Introduced as $K_{i,j}$ into $\chi^2$
Uncertainty of energy scale	Correlated error for energy spectra in keV <sub>ee</sub> $\sim \pm 10$ % for event rate in each bin Introduced as $L_{i,j}$ into $\chi^2$
FADC reset	P.E./keV yield at 122 keV $\pm 0.3$ % Introduced as $\sigma_{(syst)i,j}$ into $\chi^2$
Livetime calculation	$\pm 0.2$ % for final result
$v_{esc}$ (544/650 km/s)	$\sigma_{\chi-n} + 10$ % at 8 GeV $\sigma_{\chi-n} + 5$ % at 20 GeV
$L_{eff}$	$\sigma_{\chi-n} \pm 30$ % at 10 GeV
Cosmic-ray muon	$\ll 1$ % of total count rate
Rn in water	$1.4 \times 10^{-5}$ event/day/kg/keV at maximum
Rn in LXe	1 % of amplitude

# Chapter 7

## Result

A search for dark matter by annual modulation analysis is conducted using XMASS-I data. For this analysis, the data observed between November 2013 and March 2015 are used. The livetime is 359.2 days. Target mass in the active region is 832 kg. 0.82 kg-year exposure is achieved. The observed data were divided into 18(145) energy  $\times$  40 time bins. Used energy region is 1–10 keV<sub>ee</sub> and 0.5–15 keV<sub>57Co</sub>, and the energy bin width is 0.5 keV<sub>ee</sub> and 0.1 keV<sub>57Co</sub> for model independent and WIMP model dependent analysis, respectively. The time bin width is about 10 days.

### 7.1 Definition of $\chi^2$

In order to obtain an amplitude of possible annual modulation of dark matter and a constant of event rate in each energy bin, a  $\chi^2$  test with equation 7.1 is carried out.

$$\chi^2 = \sum_i^{E\text{-bins}} \left\{ \sum_j^{t\text{-bins}} \frac{(R_{i,j}^{obs} - \alpha K_{i,j} - \beta L_{i,j} - R_{i,j}^{pred})^2}{\sigma_{(stat)i,j}^2 + \sigma_{(syst)i,j}^2} \right\} + \alpha^2 \quad (7.1)$$

$$\text{Model independent : } R_{i,j}^{Pred} = C_i + A_i \cos \frac{2\pi(t_j - t_0)}{T} \quad (7.2)$$

$$\text{WIMP-model : } R_{i,j}^{Pred} = C_i + \sigma_{\chi-n} \times A_i(m_\chi) \cos \frac{2\pi(t_j - t_0)}{T} \quad (7.3)$$

Here,  $R_{i,j}^{obs}$  represents observed event rate in each energy–time bin.  $R_{i,j}^{obs}$  is divided by center value of relative cut efficiency which is explained in Section 6.1 corresponding to each time bin.  $K_{i,j}$  and  $L_{i,j}$  are introduced as maximum/minimum systematic errors due to variation of xenon absorption length which is explained in Section 6.1 and systematic error of energy scaling in Figure 4.9 with a nuisance parameter "pull term"  $\alpha$  and  $\beta$  [64].  $\alpha$  and  $\beta$  are common parameters in whole energy and time bins.  $K_{i,j}$  is determined for each energy and time bin using relative cut efficiency in Fig. 6.2 and time variation of LXe absorption length in Fig. 4.12(b).  $K_{i,j}$  is determined to be mean value of differences between  $R_{i,j}^{obs}$  with maximum/minimum relative cut efficiency and  $R_{i,j}^{obs}$  with center of that. Figure 7.1 and 7.2 show  $K_{i,j}$

distribution as a function of time.  $K_{i,j}$  can have both of positive and negative value. It has negative (positive) value with high (low) ABSL of LXe.  $L_{i,j}$  is determined for each energy and time bin using error band of energy scale in Fig. 4.9.  $L_{i,j}$  is determined to be mean value of differences between  $R_{i,j}^{obs}$  with energy scaling with maximum/minimum systematic error and  $R_{i,j}^{obs}$  with center of that. Figure 7.3 and 7.4 show  $L_{i,j}$  distribution as a function of time.  $\sigma_{(stat)i,j}^2$  represents statistical error.  $\sigma_{(syst)i,j}^2$  represents systematic error and includes systematic error by FADC initialization method described in Section 6.3. Systematic error by energy scale ( $L_{i,j}$ ) is applied only in model independent analysis. Equation 7.2 and 7.3 represent  $R_{i,j}^{pred}$  in model independent and WIMP model dependent cases, respectively.  $C_i$  and  $A_i$  represent constant and amplitude of time variation plots in each energy-bin.  $\sigma_{\chi-n}$  and  $A_i(m_\chi)$  represent WIMP-nucleon cross-section and amplitude of each energy-bin as a function of WIMP mass  $m_\chi$ .  $T$  and  $t_0$  are period and phase of modulation and they are fixed to 365.24 days and 152.5 days. Assuming this phase, the days with maximum and minimum dark matter rates occur on Jun. 2<sup>nd</sup> and Dec. 4<sup>th</sup>, respectively. All energy and time bins are fitted simultaneously.

## 7.2 Model-independent modulation search

By using  $\chi^2$  in Section.7.1, the dataset were fitted.  $R_{i,j}^{pred}$  in equation 7.2 was used for model-independent analysis.  $C_i$ ,  $A_i$  and  $\alpha$  are treated as fitting parameters. Modulation's period  $T$  and phase  $t_0$  are fixed to be 365.24 days and 152.5 days. Figure 7.5, 7.6, 7.7, and 7.10 show time variation plots in each energy bin. Energy range and fitted amplitude ( $A_i$ ) are described in each plot. Fitted  $\alpha$  and  $\beta$  values were  $0.64 \pm 0.15$  and  $0.12 \pm 0.08$ . Minimum  $\chi^2$  was 714.4. There are 18 of energy bins and 40 of time bins in fitted dataset. Fitting parameters are 18  $A_i$ , 18  $C_i$  for each energy bin and a common  $\alpha$ . Therefore,  $\text{ndf}(\text{number of degrees of freedom})$  is 682 ( $18 \times 40 - 38$ ).

### 7.2.1 Dummy samples

In order to estimate p-value [5], 10000 of dummy samples were produced with the following methods:

1. Applying linear fitting for time variation plot of each energy bin, the average event rates ( $R_{mean,i}$  [/day/kg]) are obtained.
2. Random parameters  $\alpha_{tmp}$  and  $\beta_{tmp}$  are determined from Gaussian distribution with mean=0 and sigma=1. Since the systematic errors from relative cut efficiency and energy scale are determined by maximum and minimum values,  $\alpha_{tmp}$  and  $\beta_{tmp}$  are limited to be  $-1 < \alpha_{tmp} < 1$  and  $-1 < \beta_{tmp} < 1$ . They are common parameters for whole time and energy bins of a dummy sample.
3.  $N_{i,j}^{mean}$  is defined for each time and energy bin as following equation.

$$N_{i,j}^{mean} = (R_i^{mean} + \alpha_{tmp} \times K_{i,j} + \beta_{tmp} \times L_{i,j}) \times \text{livetime}_j \times 832.\text{kg} \quad (7.4)$$

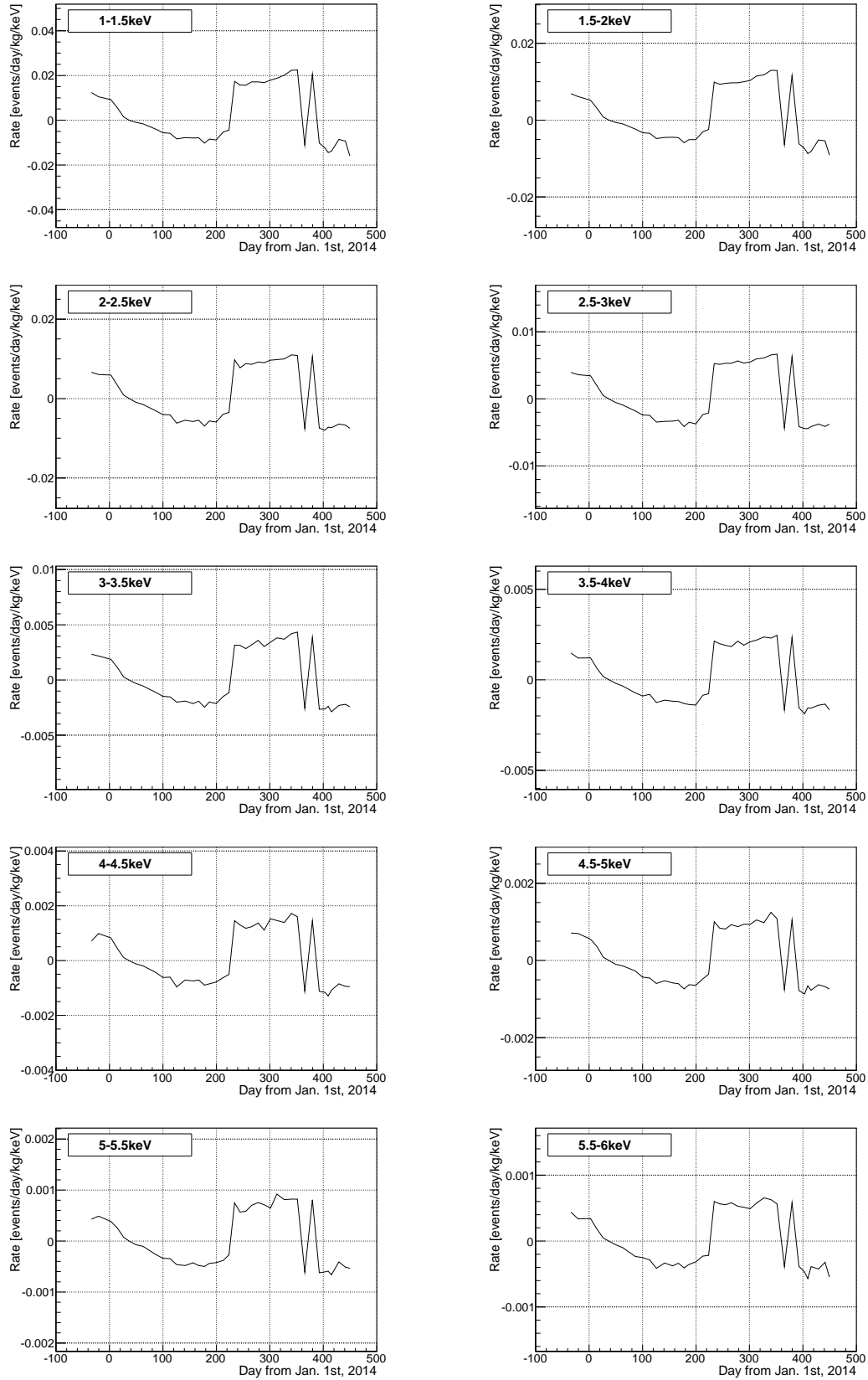


Figure 7.1:  $K_{i,j}$  distribution in each energy and time bin.

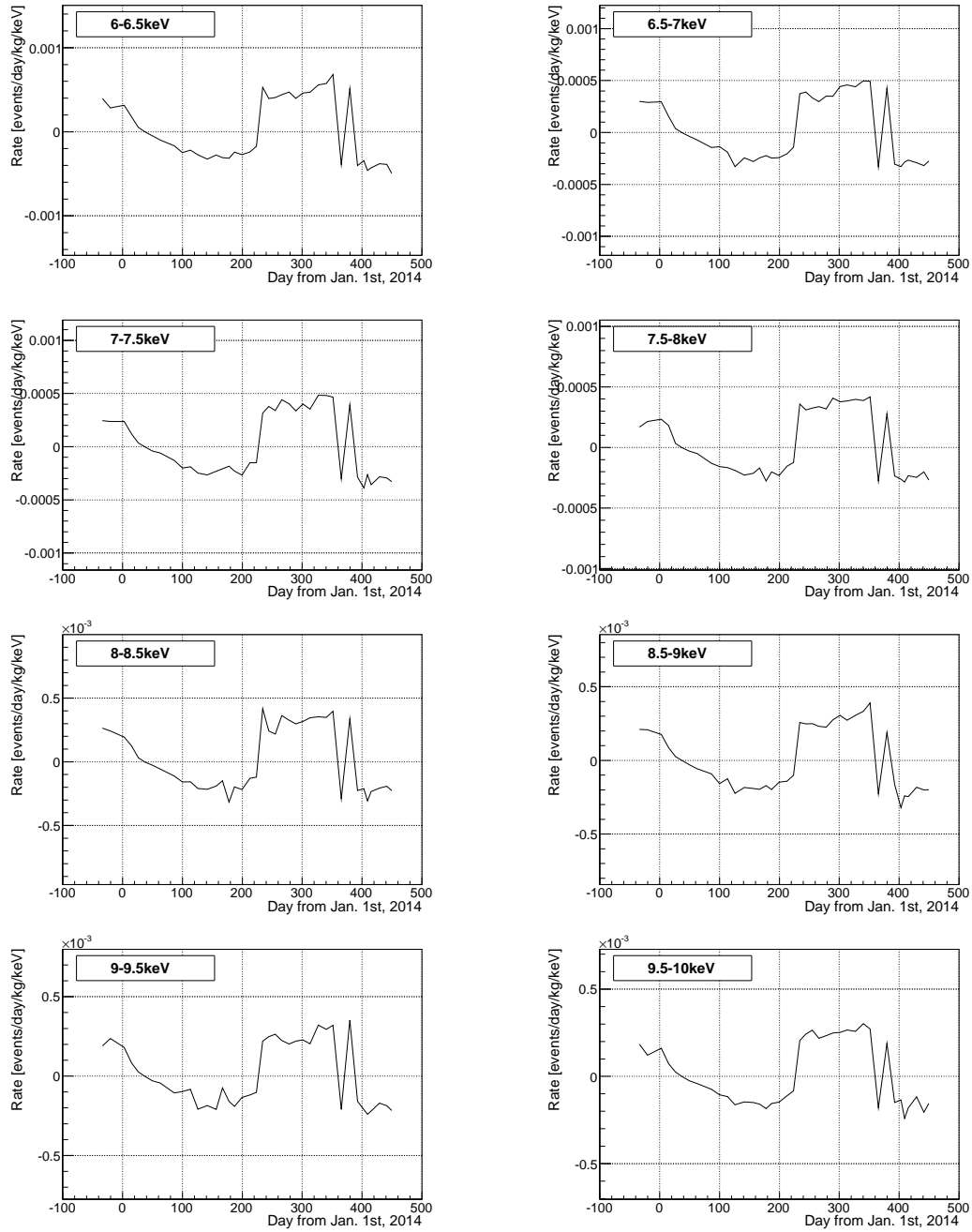


Figure 7.2:  $K_{i,j}$  distribution in each energy and time bin.

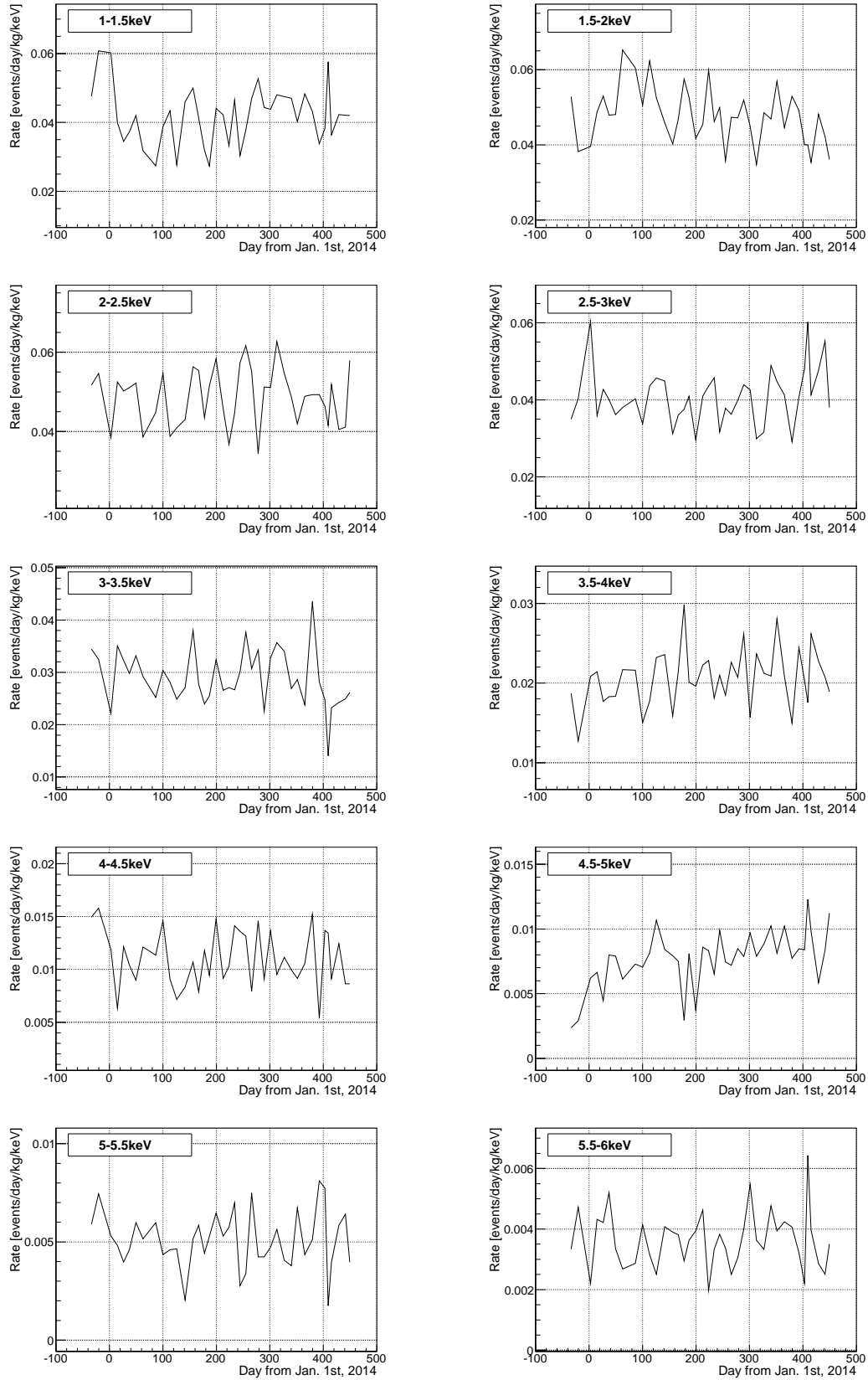


Figure 7.3:  $L_{i,j}$  distribution in each energy and time bin.

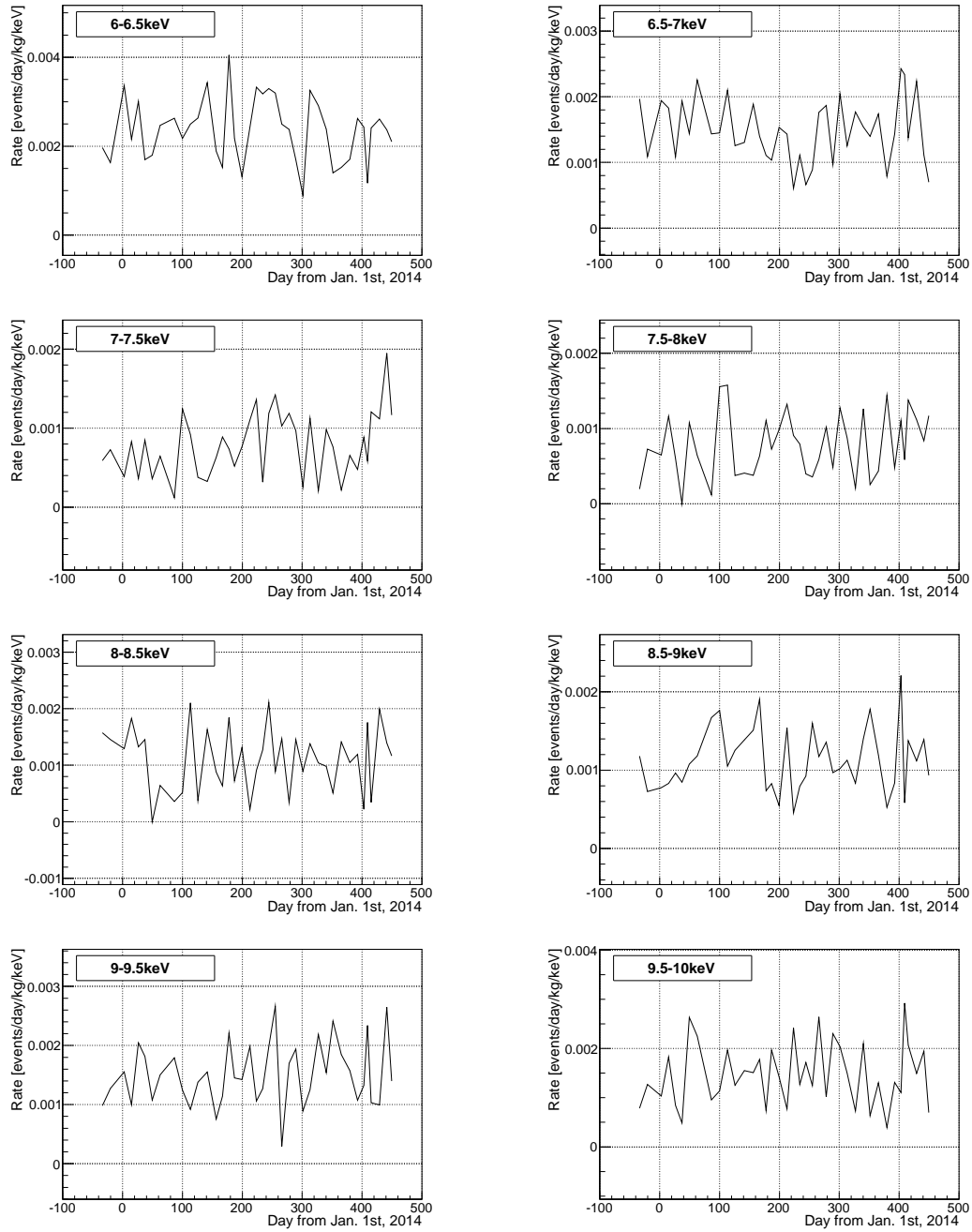


Figure 7.4:  $L_{i,j}$  distribution in each energy and time bin.

4.  $N_{i,j}$  is randomly determined from Poisson distribution with mean= $N_{i,j}^{mean}$ .  
 $R_{i,j}^{dummy}$  are obtained in each energy and time bin from  $N_{i,j}$ , as follows.

$$N_{i,j} = Pois(N_{i,j}^{mean}) \quad (7.5)$$

$$R_{i,j}^{dummy} = \frac{N_{i,j} \pm \sqrt{N_{i,j}}}{livetime_j \times 832 \text{ kg}} \quad (7.6)$$

5. Apply the same analysis as observed dataset by replacing  $R_{i,j}^{obs}$  with  $R_{i,j}^{dummy}$  in Eq. 7.1. Then obtain  $A_i$ ,  $C_i$  and  $\alpha$  for the dummy sample.
6. These processes were repeated 10000 times. 10000 of dummy samples were produced.

## 7.2.2 Result

Figure 7.11 shows the fitting result of amplitude after correcting the detection efficiency for gamma-ray. Black points with red error bars are fitted amplitude by the observed dataset. Cyan band represent distribution of fitted amplitude for each dummy sample. Cyan and light cyan band represent  $\pm 1\sigma$  and  $\pm 2\sigma$ , respectively. Black line represent the 90% C.L. upper limit for positive and negative amplitude. The 90% C.L. upper limit lines were calculated with the following equations.

$$\frac{\int_0^{a_{up}^{pos}} G(A_i, \sigma_{A_i}) da}{\int_0^{\infty} G(A_i, \sigma_{A_i}) da} = 0.9 \text{ (positive amplitude)} \quad (7.7)$$

$$\frac{\int_{a_{up}^{neg}}^0 G(A_i, \sigma_{A_i}) da}{\int_{-\infty}^0 G(A_i, \sigma_{A_i}) da} = 0.9 \text{ (negative amplitude)} \quad (7.8)$$

Here,  $G(A_i, \sigma_{A_i})$  represents Gaussian distribution with mean  $A_i$  and variance  $\sigma_{A_i}$ .  $a$ ,  $a_{up}^{pos}$  and  $a_{up}^{neg}$  represent the amplitude and its 90 % C.L. points of positive and negative amplitude, respectively. The detection efficiency was estimated from MC with uniformly distributed mono-energy gamma-ray in LXe volume. Figure 7.12 shows the the efficiency. In Table 7.1, the results from independent analysis are summarized.

## 7.2.3 p-value

To calculate p-value, the same analysis was applied to the observed dataset and 10000 of the dummy samples explained in section 7.2.1. When  $A_i$  are fixed to zero, the  $\chi^2$  value for the dataset was 739.1 . The minimum  $\chi^2$  is 714.4 with free amplitude analysis, as described in Section 7.2. Therefore, the difference of the  $\chi^2$  values ( $\Delta\chi^2$ ) becomes 24.7 .  $\Delta\chi^2$  of each dummy sample was calculated with the same method, then make a  $\Delta\chi^2$  distribution from 10000 of dummy samples. Figure

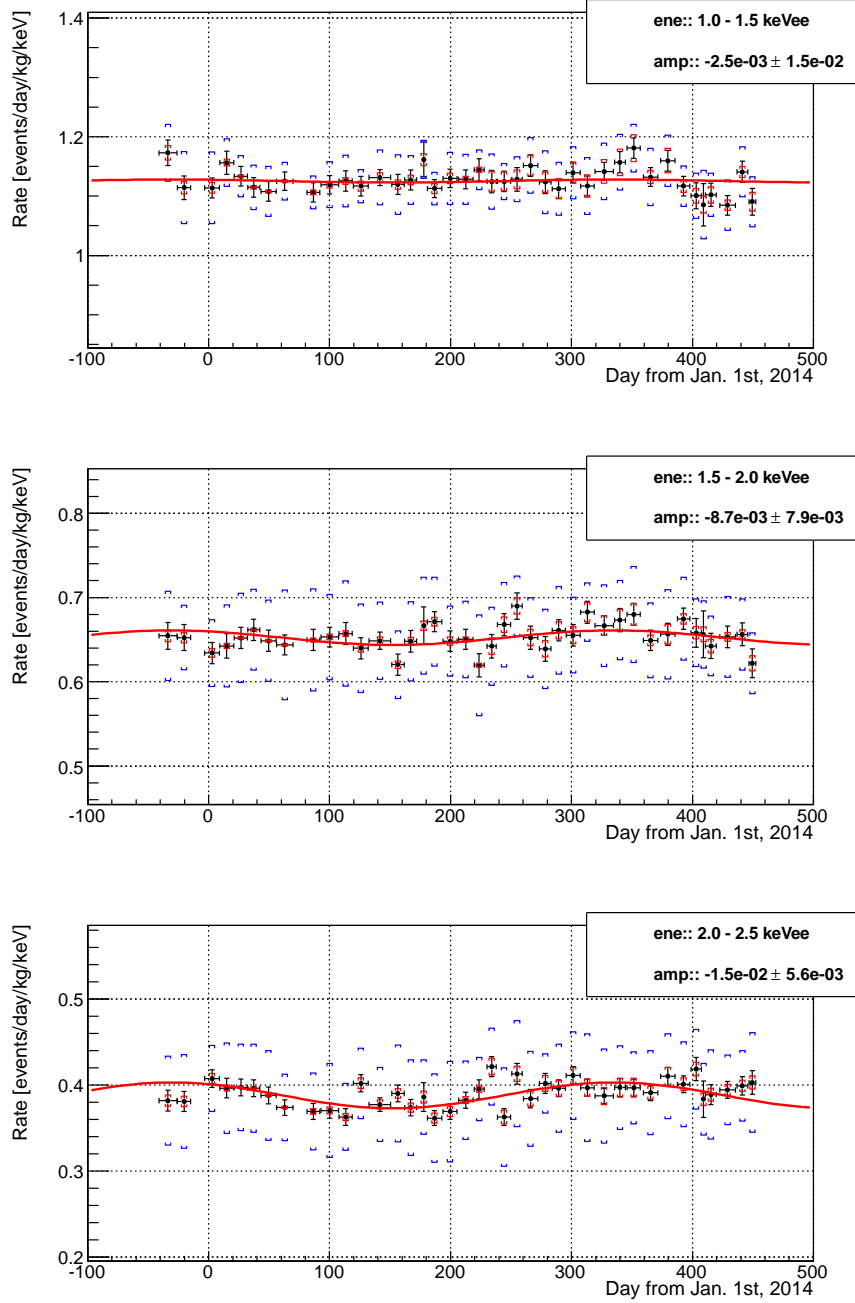


Figure 7.5: Time variation plot in each energy bin. Black points, red brackets, blue brackets and red lines represent  $R_{i,j}^{obs}$ ,  $K_{i,j}$ ,  $L_{i,j}$  and  $R_{i,j}^{pred}$ , respectively.

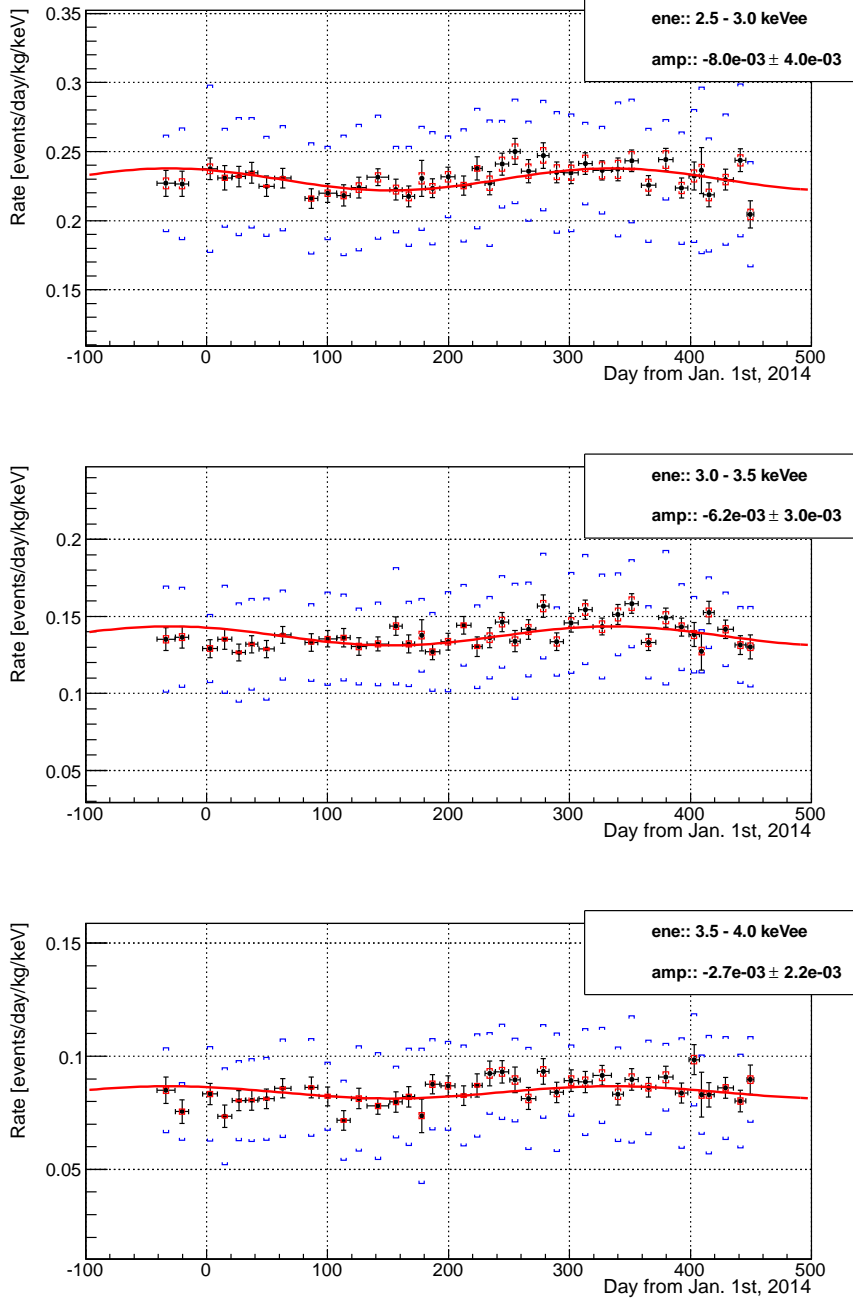


Figure 7.6: Time variation plot in each energy bin. Black points, red brackets, blue brackets and red lines represent  $R_{i,j}^{obs}$ ,  $K_{i,j}$ ,  $L_{i,j}$  and  $R_{i,j}^{pred}$ , respectively.

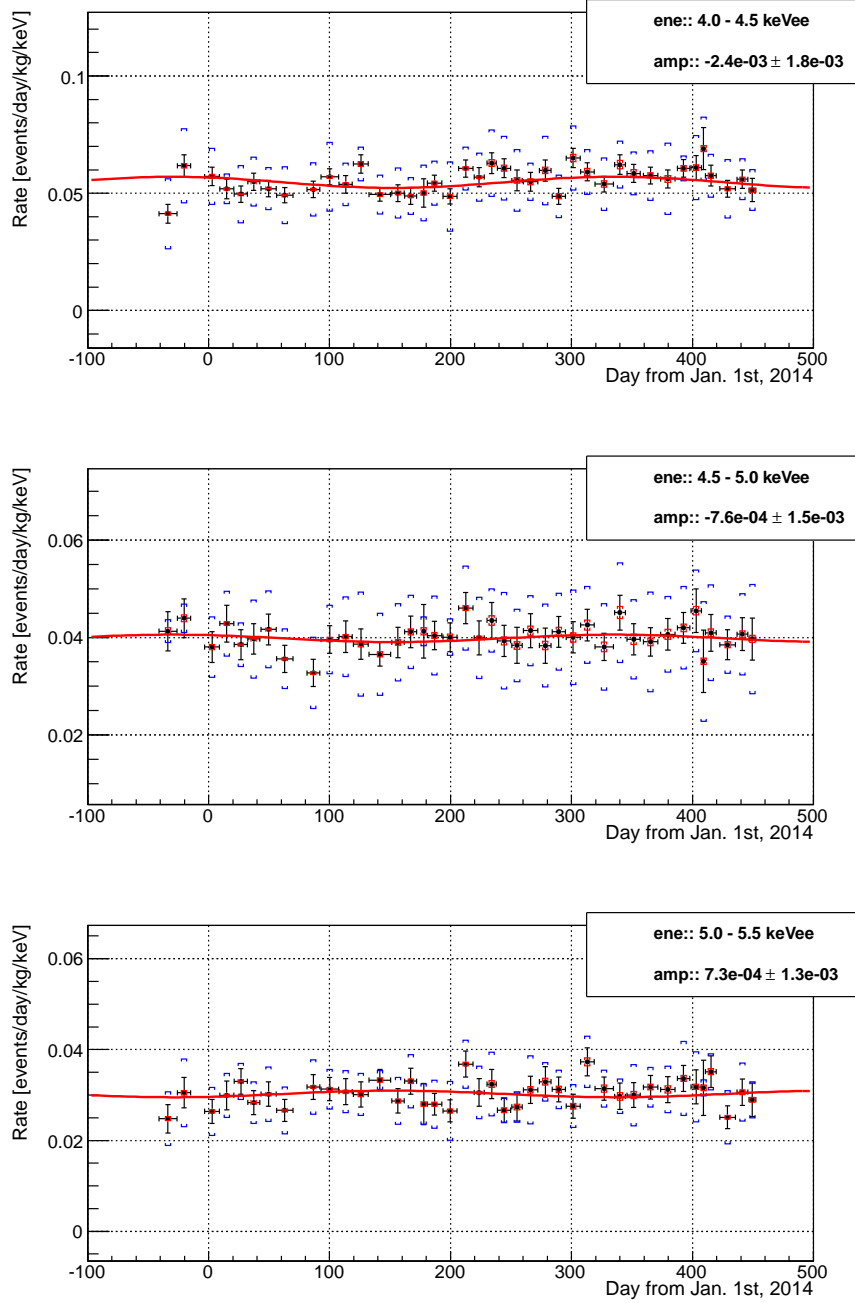


Figure 7.7: Time variation plot in each energy bin. Black points, red brackets, blue brackets and red lines represent  $R_{i,j}^{obs}$ ,  $K_{i,j}$ ,  $L_{i,j}$  and  $R_{i,j}^{pred}$ , respectively.

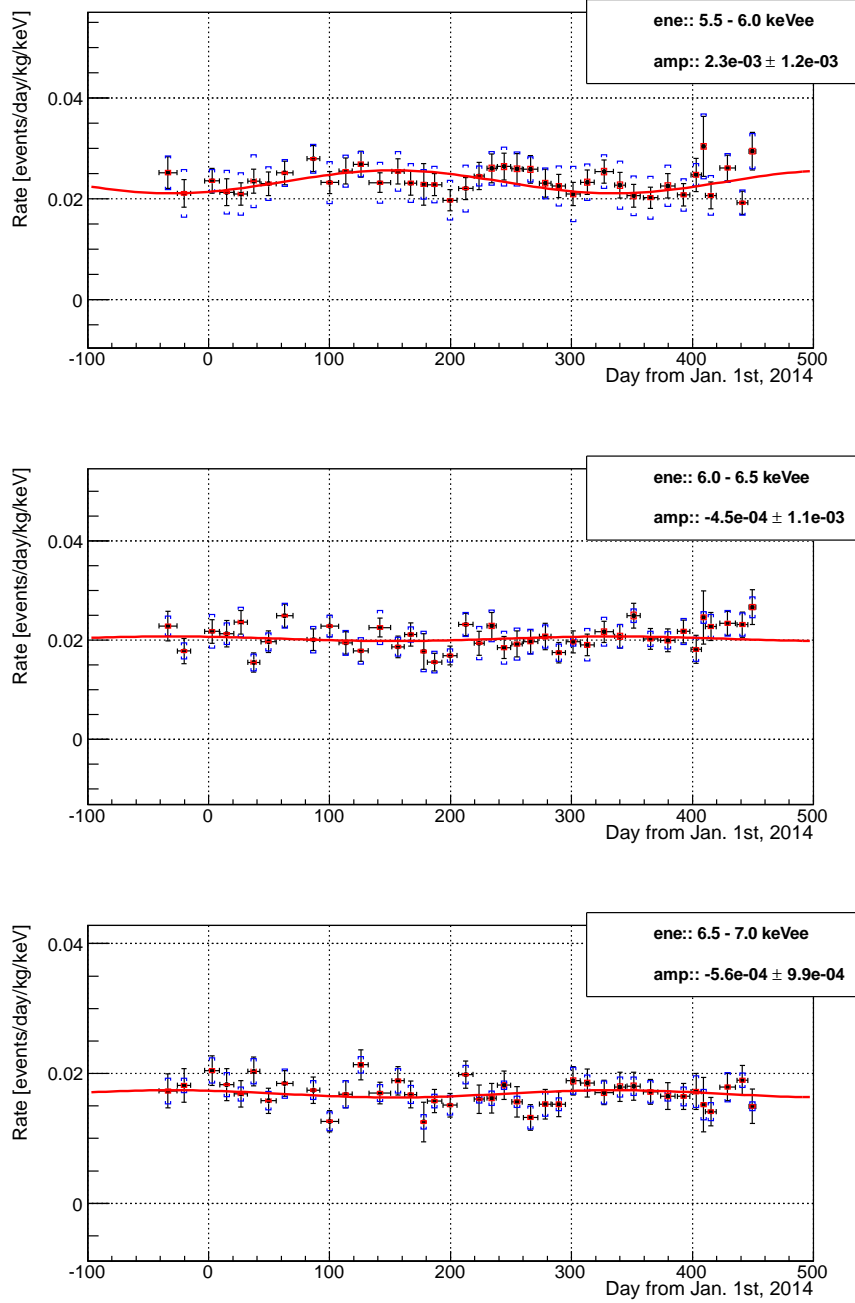


Figure 7.8: Time variation plot in each energy bin. Black points, red brackets, blue brackets and red lines represent  $R_{i,j}^{obs}$ ,  $K_{i,j}$ ,  $L_{i,j}$  and  $R_{i,j}^{pred}$ , respectively.

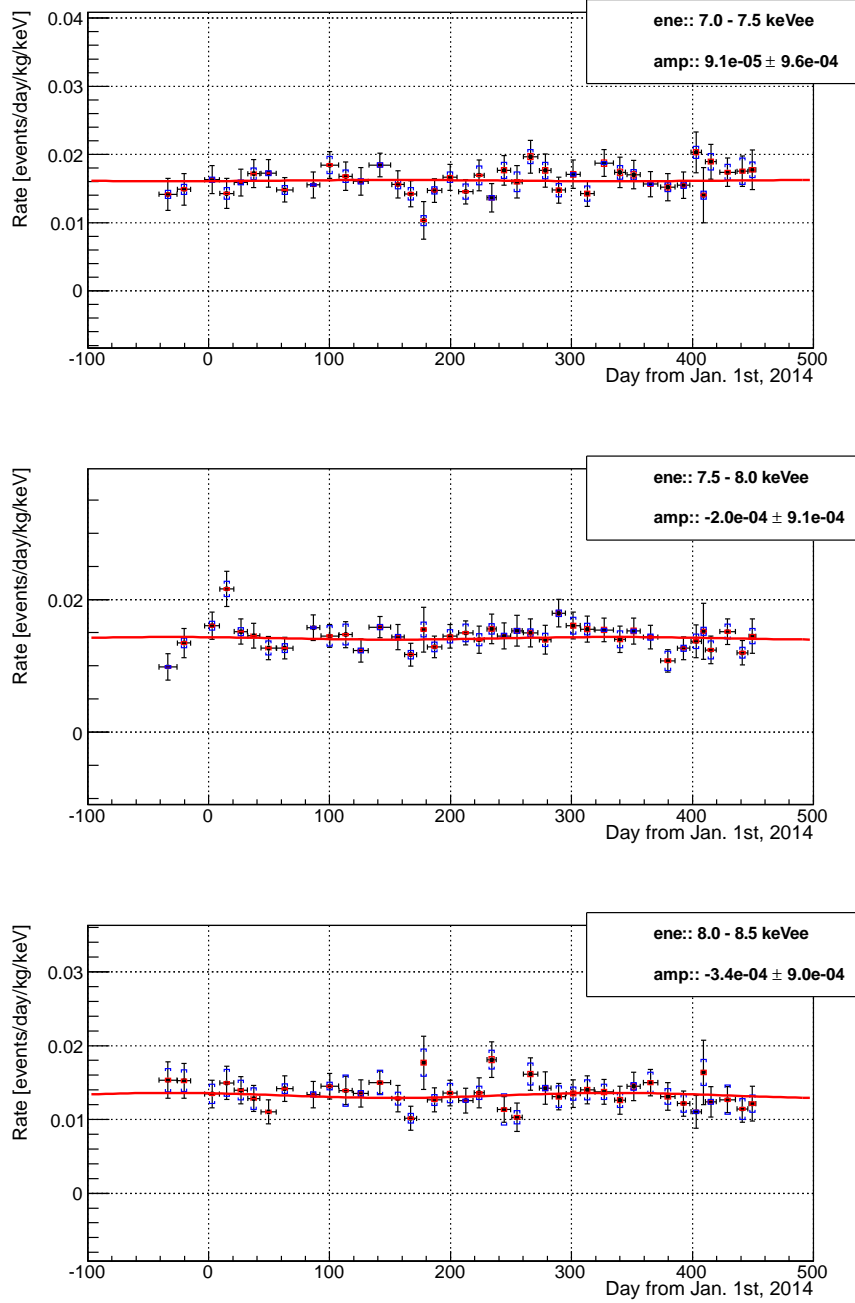


Figure 7.9: Time variation plot in each energy bin. Black points, red brackets, blue brackets and red lines represent  $R_{i,j}^{obs}$ ,  $K_{i,j}$ ,  $L_{i,j}$  and  $R_{i,j}^{pred}$ , respectively.

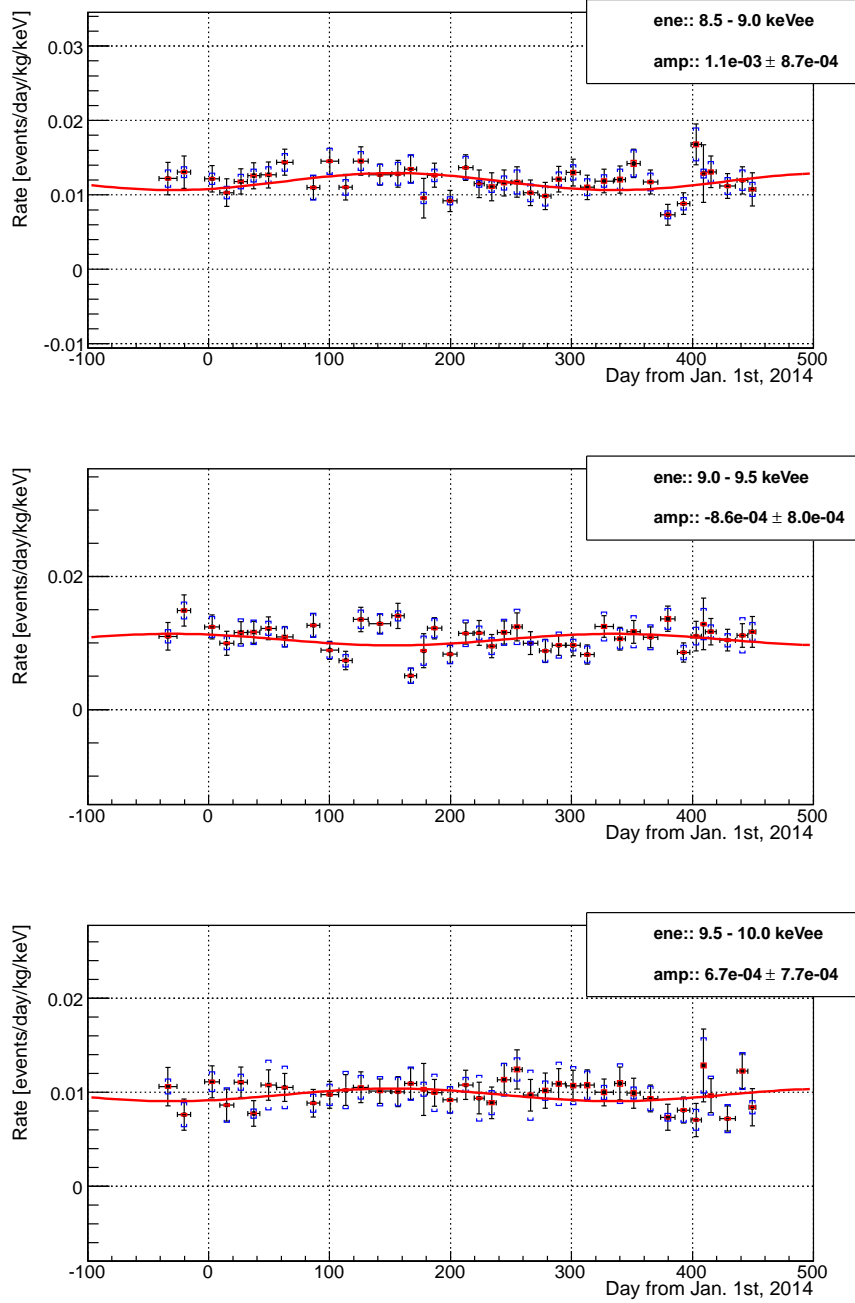


Figure 7.10: Time variation plot in each energy bin. Black points, red brackets, blue brackets and red lines represent  $R_{i,j}^{obs}$ ,  $K_{i,j}$ ,  $L_{i,j}$  and  $R_{i,j}^{pred}$ , respectively.

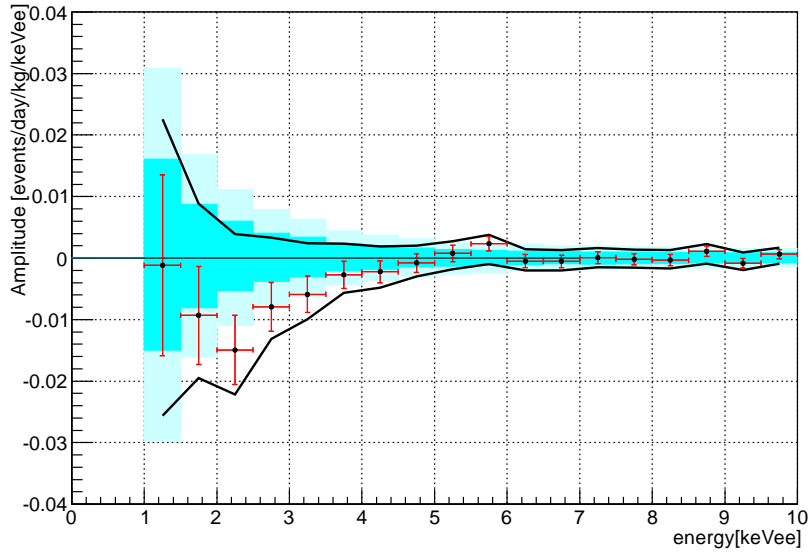


Figure 7.11: Modulation amplitude resulted from model independent analysis as a function of energy [keV<sub>ee</sub>]. Plot with error bar is the observed amplitude. Cyan and light cyan bands are  $\pm 1 \sigma$  and  $\pm 2 \sigma$  expected amplitude from dummy samples.

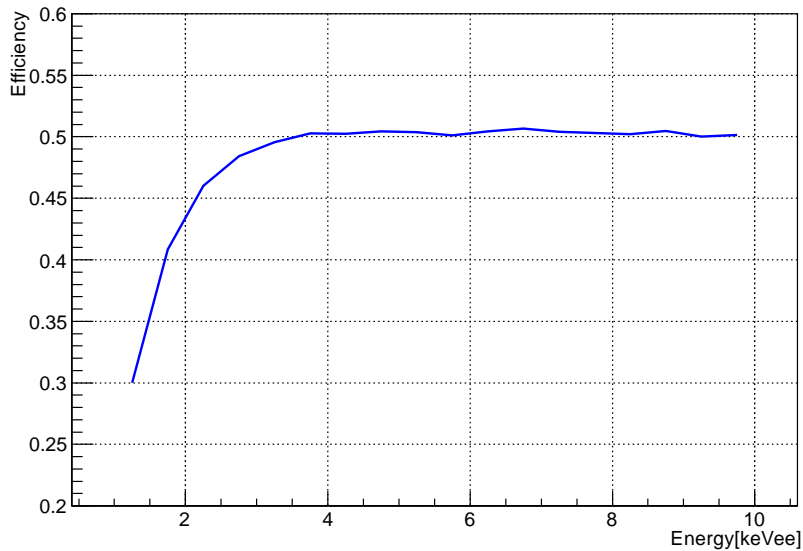


Figure 7.12: The detection efficiency estimated from MC with uniformly distributed mono-energy gamma-ray in LXe volume.

Table 7.1: Model independent analysis results.  $C_i$  and  $A_i$  are listed with their errors. 90 % C.L. positive and negative upper limits  $a_{up}^{pos}$  and  $a_{up}^{neg}$  are also shown.

Energy [keV <sub>ee</sub> ]	$C_i$	$\sigma_{C_i}$	$A_i$	$\sigma_{A_i}$	$a_{up}^{pos}$	$a_{up}^{neg}$
1.0–1.5	1.120	0.004	-0.001	0.015	0.023	-0.026
1.5–2.0	0.646	0.004	-0.009	0.008	0.0088	-0.019
2.0–2.5	0.382	0.004	-0.015	0.006	0.0039	-0.022
2.5–3.0	0.225	0.003	-0.008	0.004	0.0033	-0.013
3.0–3.5	0.134	0.002	-0.006	0.003	0.0024	-0.0099
3.5–4.0	0.0816	0.0017	-0.003	0.002	0.0024	-0.0057
4.0–4.5	0.0534	0.0010	-0.002	0.002	0.0019	-0.0048
4.5–5.0	0.0389	0.0008	-0.0008	0.0015	0.0020	-0.0030
5.0–5.5	0.0296	0.0006	0.0008	0.0013	0.0027	-0.0018
5.5–6.0	0.0229	0.0005	0.0023	0.0012	0.0038	-0.00099
6.0–6.5	0.0200	0.0004	-0.0005	0.0011	0.0015	-0.0020
6.5–7.0	0.0167	0.0004	-0.0005	0.0010	0.0013	-0.0020
7.0–7.5	0.0161	0.0003	0.00007	0.0010	0.0016	-0.0015
7.5–8.0	0.0141	0.0003	-0.0002	0.0009	0.0013	-0.0016
8.0–8.5	0.0131	0.0003	-0.0003	0.0009	0.0013	-0.0017
8.5–9.0	0.0117	0.0003	0.0011	0.0009	0.0023	-0.00089
9.0–9.5	0.0103	0.0003	-0.0008	0.0008	0.00089	-0.0020
9.5–10.0	0.0096	0.0003	0.0006	0.0008	0.0017	-0.00091

7.13 shows the  $\chi^2$  distributions of the dummy sample analyses. Blue solid line and red dotted line show  $\chi^2$  distribution from the analyses with free amplitude and zero-fixed amplitude, respectively. Figure 7.14 shows the  $\Delta\chi^2$  distribution. Red dotted line shows the  $\Delta\chi^2$  value of observed dataset. The p-value is 17.7 % and is higher than 5 %. Therefore, the model-independent amplitude in this analysis is found to be consistent with background fluctuations.

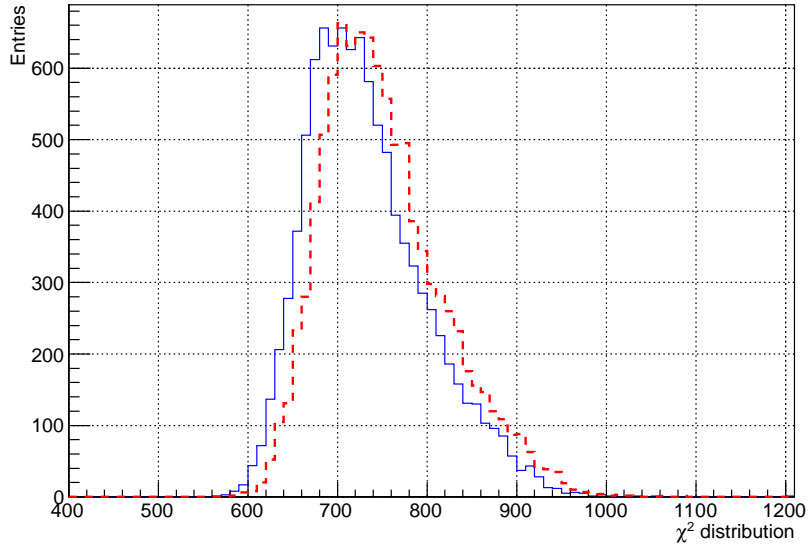


Figure 7.13:  $\chi^2$  distribution of dummy sample analyses. Blue solid and red dotted line represent distribution from the analyses with free amplitude and zero-fixed amplitude.

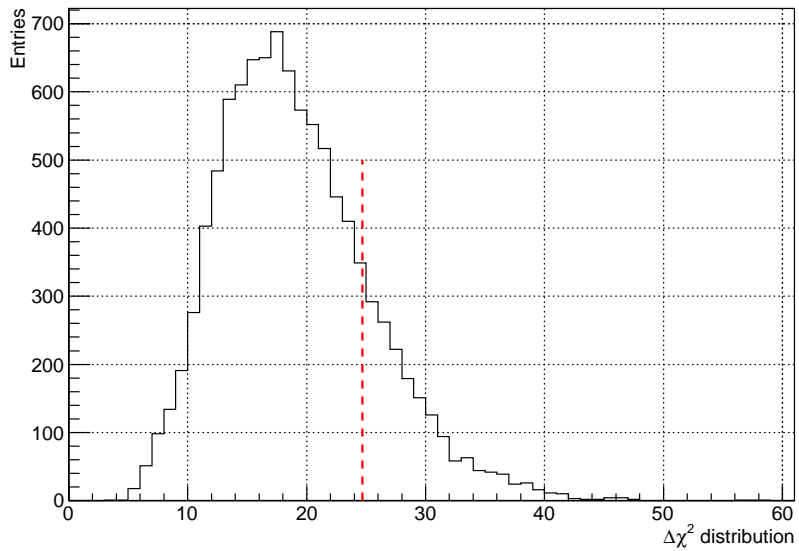


Figure 7.14: Solid black line shows  $\Delta\chi^2$  distribution of dummy sample analyses. Red dotted line represents the  $\Delta\chi^2$  value from the analysis with observed dataset. The p-value resulted from this plot is 17.7 %.

### 7.3 WIMP model dependent search

A WIMP model dependent search was done with a  $\text{keV}_{57\text{Co}}$  base analysis. Energy range  $0.5\text{--}15.0 \text{ keV}_{57\text{Co}}$  was used in this analysis and it is separated into  $0.1 \text{ keV}_{57\text{Co}}$  energy bins. The observed dataset separated into  $145 \text{ energy} \times 40 \text{ time}$  bins are fitted with the  $\chi^2$  test in Eq. 7.1 and Eq. 7.3. Same as model independent case, modulation's period  $T$  and phase  $t_0$  are fixed to be  $365.24$  days and  $152.5$  days. Also, constant values of time variation plots in each energy bin are treated as fitting parameters. Expected WIMP amplitude for each WIMP mass  $A_i(m_\chi)$  is determined by WIMP–nucleon recoil MC simulation.  $\sigma_{\chi-n}$  represents WIMP–nucleon cross section and it is a fitting parameter.

For  $6\text{--}20 \text{ GeV}$  WIMPs, the  $\chi^2$  test was carried out. In Table 7.3, the fitting results of the WIMP search are summarized. From fitted  $\sigma_{\chi-n}$ 's mean and error,  $90\%$  C.L. upper limit of WIMP–nucleon cross section [ $\text{cm}^{-2}$ ] was obtained with Eq. 7.7.  $\chi^2$ , ndf and fitted  $\alpha$  values are also shown. Figure 7.15 shows the WIMP annual modulation search result in XMASS–I dataset. Horizontal axis and vertical axis is WIMP mass [ $\text{GeV}$ ] and  $\sigma_{\chi-n}$  [ $\text{cm}^{-2}$ ], respectively. Solid black line represents the  $90\%$  C.L. upper limit. Like model independent analysis, same analysis as observed dataset was applied to the  $10000$  dummy samples.  $\pm 1\sigma$  and  $\pm 2\sigma$  bands represents the expected region obtained from the dummy sample analysis. No significant signal was found in this analysis.

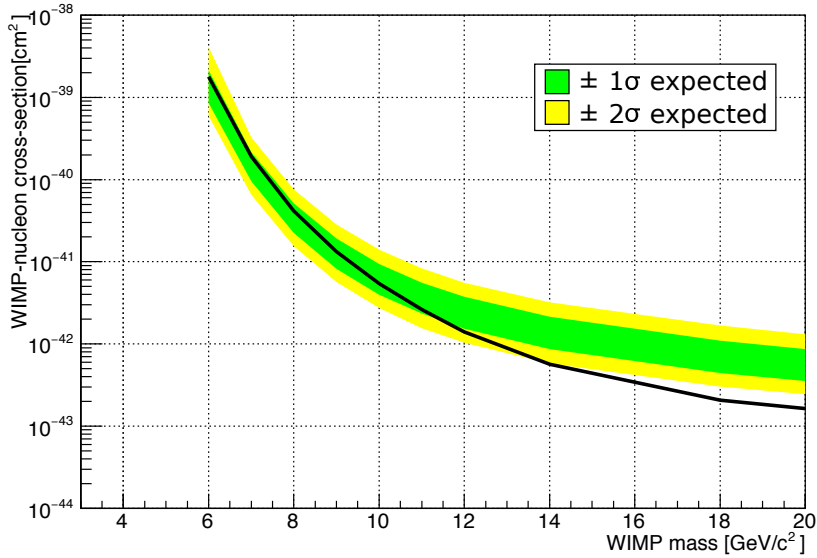


Figure 7.15: The WIMP annual modulation search result in XMASS–I dataset. Solid black line represents the  $90\%$  C.L. upper limit.  $\pm 1\sigma$  and  $\pm 2\sigma$  bands represents the expected region obtained from the dummy sample analysis.

Table 7.2: WIMP fitting result for each WIMP mass. Mean and error of  $\sigma_{\chi-n}$  are shown. 90% C.L. upper limit of WIMP–nucleon cross section was obtained with Eq. 7.7. Also,  $\chi^2$ , ndf and  $\alpha$  values are shown.

WIMP mass[GeV]	$\sigma_{\chi-n}$	$\sigma_{\chi-n}$ fitting error	90% C.L.	$\chi^2$	ndf	$\alpha$
6	$5.9 \times 10^{-40}$	$8.3 \times 10^{-40}$	$1.8 \times 10^{-39}$	2701.43	2533	0.55
7	$5.4 \times 10^{-41}$	$9.3 \times 10^{-41}$	$1.9 \times 10^{-40}$	2701.60	2533	0.55
8	$7 \times 10^{-42}$	$22 \times 10^{-42}$	$4.1 \times 10^{-41}$	2701.83	2533	0.55
9	$-5 \times 10^{-43}$	$83 \times 10^{-43}$	$1.3 \times 10^{-41}$	2701.93	2533	0.54
10	$-2.3 \times 10^{-42}$	$4.0 \times 10^{-42}$	$5.4 \times 10^{-42}$	2701.62	2533	0.53
11	$-2.7 \times 10^{-42}$	$2.4 \times 10^{-42}$	$2.6 \times 10^{-42}$	2700.62	2533	0.51
12	$-2.8 \times 10^{-42}$	$1.6 \times 10^{-42}$	$1.4 \times 10^{-42}$	2698.71	2533	0.49
14	$-2.8 \times 10^{-42}$	$0.9 \times 10^{-42}$	$5.7 \times 10^{-43}$	2692.21	2533	0.44
18	$-2.3 \times 10^{-42}$	$0.5 \times 10^{-42}$	$2.1 \times 10^{-43}$	2678.31	2533	0.34
20	$-1.9 \times 10^{-42}$	$0.4 \times 10^{-42}$	$1.6 \times 10^{-43}$	2676.71	2533	0.33

# Chapter 8

## Discussion

### 8.1 WIMP search result

The WIMP annual modulation search in XMASS-I data was carried out and explained in Section 7.3. 90 % C.L. upper limit by this study is described as black solid line and compared with other experiments' results in Figure 8.1.

The lines and filled regions represent 90 % C.L. upper limits and allowed regions by other experiments, respectively. Orange solid line represents the result from XMASS-I dataset before refurbishment [34]. Red lines are 90 % C.L. upper limits by XENON experiments, dotted one is obtained from nuclear recoil search using

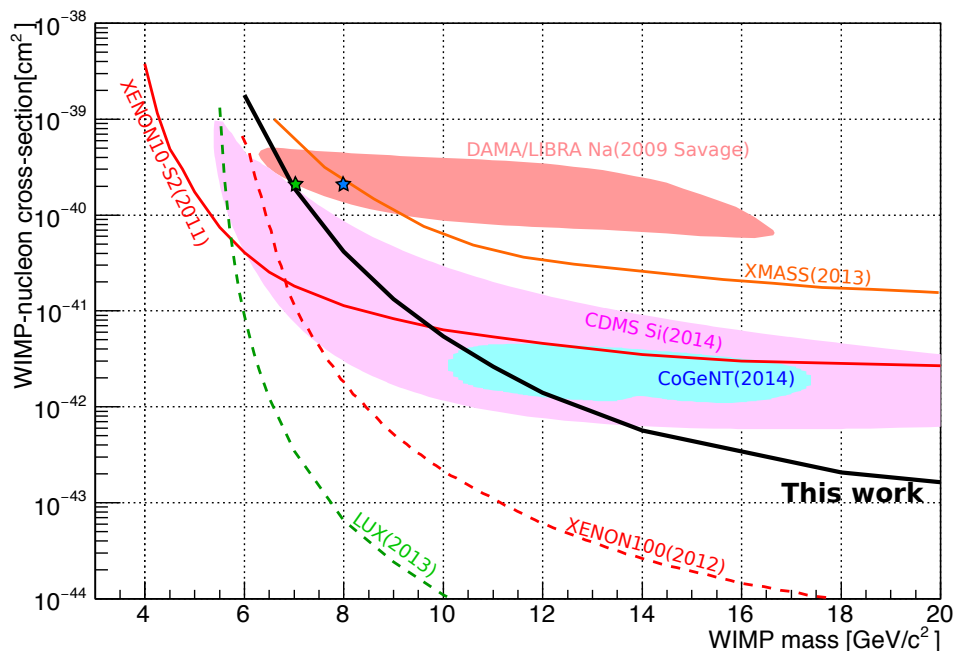


Figure 8.1: The WIMP modulation search result in XMASS-I dataset is compared with other experiments' results [34, 22, 35, 21, 36, 13, 14].

both scintillation and ionization[22] and solid one is obtained from electron recoil search using only ionized electron signal [35]. Dotted Green line represents 90 % C.L. upper limits from LUX experiment [21]. Light red, magenta and light blue filled regions are allowed region by DAMA(Na target)[36], CDMS(Si target)[13] and CoGeNT[14] experiments, respectively. Total exposure of this analysis is 0.82 ton-year. That of DAMA experiment is 1.33 ton-year [16]. The result by this study exclude DAMA's allowed region in higher WIMP mass range then 8 [GeV] using comparable statistics and annual modulation. This is the first extensive search probing this region with an exposure comparable to DAMA's.

Figure 8.2 shows the time variation in 0.5–1.0 keV $_{57\text{Co}}$  in XMASS-I dataset and expected WIMP event rates in XMASS-I detector with a WIMP–nucleon cross section of  $2 \times 10^{-40} \text{ cm}^2$  which is in the favored region by DAMA. Dotted blue and green lines are 8 and 7 GeV WIMP spectrum expected by DAMA's result. WIMP–nucleon cross sections were assumed to be values at blue and green stars in Figure 8.1. XMASS-I detector has an enough sensitivity to evaluate DAMA's result. In XMASS-I dataset, modulation signal which was expected from DAMA was not observed.

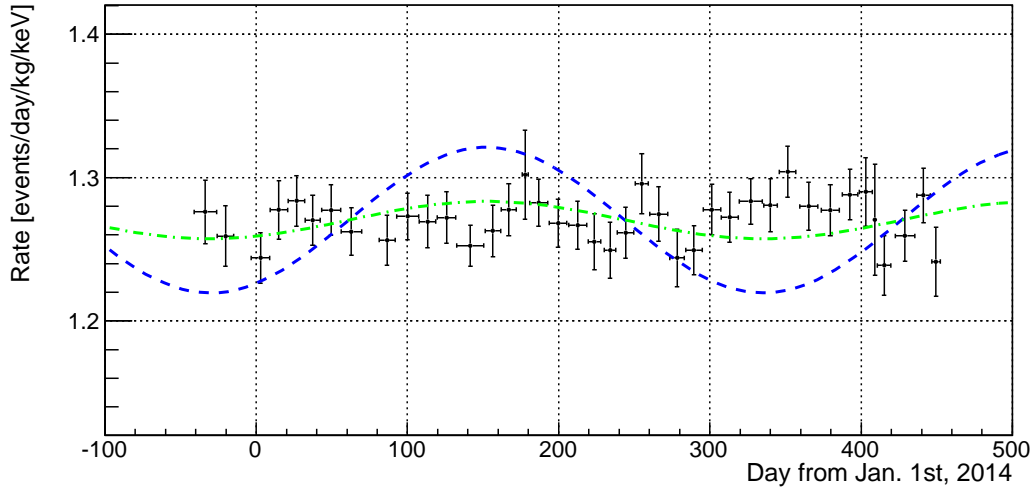


Figure 8.2: Blue(green) dashed line represents expected amplitude by DAMA for 8(7)GeV WIMP [36]. Black points represent observed time variation plot by XMASS-I detector in 0.5-1.0keV $_{57\text{Co}}$  energy region. Rates in time variation plot are corrected by  $-\alpha \times K_{i,j}$ . Here,  $\alpha$  is selected to be 0.55 obtained from Table 7.3.

## 8.2 Model independent result

The model independent modulation search in XMASS-I data was carried out and explained in Section 7.2. The  $\Delta\chi^2$  value of observed data was compared with those of dummy samples and then p-value was found to be 6.9 %. Therefore, the model-independent amplitude was found to be consistent with background fluctuations.

In Figure 8.3, time variation plots in XMASS-I dataset in 2–4, 2–5 and 2–6 keV<sub>ee</sub> are shown. Observed amplitudes by DAMA’s phase fixed analysis [16] are overlaid. XMASS-I detector has enough sensitivity to observe DAMA’s modulation. However expected modulation by DAMA’s result was not observed by model independent modulation analysis in XMASS-I dataset. Observed amplitude by DAMA is  $0.0167 \pm 0.0022$ ,  $0.0122 \pm 0.0016$  and  $0.0096 \pm 0.0013$  count/day/kg/keV in 2–4, 2–5 and 2–6 energy regions, respectively. 90 % C.L. upper limits of amplitude obtained from this study shown in Table 7.1 exclude their result.

### 8.3 Summary and future prospects

Annual modulation search in XMASS-I dataset was conducted with 832 kg Xe target and 359.2 days livetime. Result from WIMP model dependent analysis almost excludes DAMA’s allowed region. Observed amplitude in model independent analysis excludes DAMA’s amplitude. It is not significant, however, negative amplitude was observed below 5 keV<sub>ee</sub> energy region. For example, high mass WIMP signal ( $> 50$  GeV) is expected to have annual modulation with negative amplitude like observed one. Data taking is continuing with a stable and high ABSL conditions. The result would be updated with smaller systematic errors in near future.

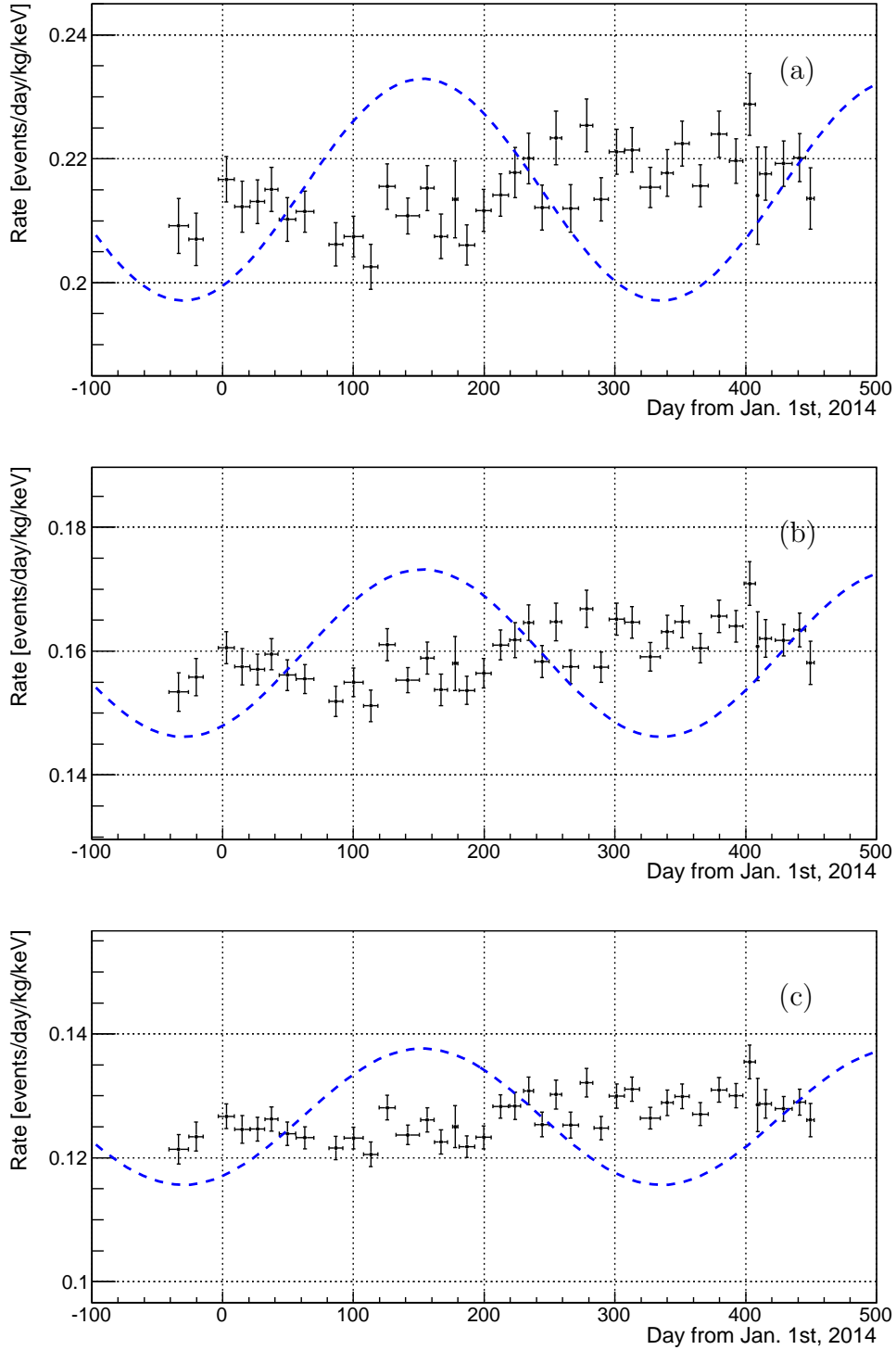


Figure 8.3: Time variation plots in (a)2–4, (b)2–5, (c)2–6 keV<sub>ee</sub> are compared with observed amplitude by DAMA’s phase fixed analysis [16]. Black points represent  $R_{i,j}^{obs}$  in XMASS-I dataset. These points are corrected by  $-\alpha \times K_{i,j}$  and  $-\beta \times L_{i,j}$ . Here,  $\alpha$  and  $\beta$  are selected to be 0.64 and 0.12 obtained from Section 7.2. Blue lines represent observed amplitude by DAMA’s phase and period fixed analysis.

# Acknowledgment

本研究を行うにあたり、多くの方々からご指導・お力添えを賜りました。誠にありがとうございます。

指導教官である竹内康雄教授は XMASS 実験に関わる機会を与えてくださり、そのおかげで完全に失っていた物理への熱を取り戻す事ができました。また、研究室に入ってから六年間丁寧に指導していただきました。身内賢太郎准教授には、本研究を進める上で重要な確かな指導を多くいただきました。

XMASS 共同研究者の皆様には、多くを学ばせていただきました。XMASS グループで研究できた事を誇りに思います。実験代表者である鈴木洋一郎教授には、ミーティングで厳しくも重要なコメントを頂きました。森山茂栄准教授には、ミーティングで最も多くのコメントやアドバイスを頂き、物理に対する真摯な姿勢や厳しさを学びました。山下雅樹准教授、平出克樹助教とは季節変動解析を共に進めさせていただきました。竹田敦助教には、特にアルミニウム線源の開発の際にお世話になりました。線源の完成を楽しみにしています。I would also like to thank to Nam Young Kim and Yong Hamb Kim who cooperate on the Aluminum source development. ヤン・ビョンス先生には、エネルギー較正を共に進めていただきました。田阪茂樹先生、関谷洋之准教授にはラドン検出器性能評価の際にご指導いただきました。

神岡の先輩方、共に学んだ同期や友人、後輩たちのおかげで神岡生活は非常に充実していました。戸村友宣助教、飯田崇史助教、上島孝太助教、高知尾理君、瀧谷寛樹君、中野佑樹君、岡直哉君、岩本康之介君、小林雅俊君、織井安里さん、阿久津良輔君、藤田黎君、毛笠莉沙子さんたちとの交流は、研究を充実させるエネルギー源となりました。森俊彰君、また飲みましょう。

劣等生であった私を博士にまで育ててくださった神戸大学粒子物理学研究室の皆様には、感謝の念に堪えません。藏重久弥教授には、Geant4 に深く関わる機会を与えていただき、丁寧にシミュレーション技術を教えていただきました。原俊雄先生、発達科学部の青木茂樹教授、鈴木州助教、矢野孝臣助教には、ニュートリノミーティングで多くを学ばせていただきました。横山有美さんには、粒子物理学研究室の秘書として研究活動をサポートしていただきました。研究室の後輩である林央樹君には卒業以降もお世話になっています。これからも遊んでください。

最後に、これまでの研究生活を支えてくれた妻と家族に深く感謝します。

# References

- [1] Steven Weinberg. A model of leptons. *Phys. Rev. Lett.*, 19:1264, 1967.
- [2] ATLAS Collaboration. *Phys. Lett. B*, 716:1–29, 2012.
- [3] CMS Collaboration. *Phys. Lett. B*, 716:30–61, 2012.
- [4] M. Honda et. al. *Prog. Theor. Phys. Suppl.*, 123:483–490, 1996.
- [5] K.A. Olive et al. (Particle Data Group). *Chin. Phys. C*, 38:090001, 2014.
- [6] Planck Collaboration. *A&A*, 571:A1, 2014.
- [7] R. D. Pecci and H. R. Quinn. *Phys. Rev. Lett.*, 38:1440, 1977.
- [8] G. Jungman et. al. *Phys. Rep.*, 267:195–373, 1996.
- [9] Maxim Pospelov et. al. *Phys Rev. D*, 78:115012, 2008.
- [10] R. Foot. *International Journal of Modern Physics D*, 13:2161–2192, 2004.
- [11] G. Angloher et. al. *Eur. Phys. J. C*, 74:3184, 2014.
- [12] A. Aguilar-Arevalo et. al. *ICRC2015 proceedings*, 2015.
- [13] R. Agnese et. al. *Phys. Rev. Lett.*, 111:251301, 2013.
- [14] D. Hooper and C. Kelso. *Phys Rev. D*, 84:083001, 2011.
- [15] D. S. Akerib et al. *Phys. Rev. Lett.*, 96:011302, 2006.
- [16] R. Bernabei et. al. *Eur. Phys. J. C*, 73:2648, 2013.
- [17] S. C. Kim et. al. *Phys. Rev. Lett.*, 108:181301, 2012.
- [18] K. Fushimi et. al. *Journal of Physics: Conference Series*, 469:012011, 2013.
- [19] K. Abe et. al. *Nucl. Instr. Meth. A*, 716:78–85, 2013.
- [20] M. Kuzniak (DEAP Collaboration). *Nuclear Physics B Proceedings Supplement*, pages 1–7, 2015.
- [21] D. S. Akerib et. al. *Phys. Rev. Lett.*, 112:091303, 2014.
- [22] E. Aprile et. al. *Phys. Rev. Lett.*, 109:181301, 2012.

- [23] P. Agnes et. al. *Phys. Lett. B*, 743:456–466, 2015.
- [24] M. Tanaka. *Journal of Physics: Conference Series*, 469:012012, 2013.
- [25] K. Miuchi et. al. *Physics Letters B*, 686:11–17, 2010.
- [26] E. Daw et. al. *Astroparticle Physics* 35, 35:397–401, 2012.
- [27] T.Katsuragawa et. al. *Journal of Physics: Conference Series*, 469:012004, 2013.
- [28] The Super-Kamiokande Collaboration. *Phys. Lett.*, 452:418, 1999.
- [29] M. G. Aartsen et. al. *Eur. Phys. J. C*, 75:492, 2015.
- [30] <https://atlas.web.cern.ch/atlas/groups/physics/confnotes/atlas-conf-2015-081/>.
- [31] <http://cms-results.web.cern.ch/cms-results/public-results/preliminary-results/exo-15-004/>.
- [32] J. Caldwell and J.P.Ostrinker. *Astro. phys. J*, 251:61, 1981.
- [33] J. D. Lewin and P. F. Smith. *Astropart. Phys.*, 6:87–112, 1996.
- [34] K. Abe et. al. *Phys. Lett. B*, 719:78–82, 2013.
- [35] E. Aprile et. al. Search for event rate modulation in xenon100 electronic recoil data. *Phys. Rev. Lett.*, 115:091302, 2015.
- [36] C. Savage et. al. *JCAP*, page 10, 2009.
- [37] H. Uchida et. al. *Prog. Theor. Exp. Phys.*, page 63C01, 2014.
- [38] XMASS Collaboration. *Phys. Lett. B*, 724:46–50, 2013.
- [39] K. Abe et. al. *Phys. Rev. Lett.*, 113:121301, 2014.
- [40] S. Fukuda et. al. *Nucl. Instr. and Meth. A*, 501:418–462, 2003.
- [41] S. Agostinelli et al. *Nucl. Instr. and Meth. A*, j506:250–303, 2003.
- [42] N. Y. Kim et. al. *Nucl. Instr. and Meth. A*, 784:499–503, 2015.
- [43] et al. A. Baldini. *IEEE Trans. Dielectr. Electr. Insul.*, 13:547, 2006.
- [44] M. Szydagis et. al. *JINST*, C10003:0–9, 2013.
- [45] The Chemical Rubber Company. *The Handbook of Chemistry and Physics*.
- [46] A. C. Sinnock and B. L. Smith. *Phys. Rev.*, 181:1297, 1969.
- [47] et. al. Particle Data Group: S. Eidelman. *Phys. Lett. B*, 592:1, 2004.

- [48] Hollis Hallett A.C. in *Argon, Helium and the Rare Gases: The Elements of the Helium Group. Vol. 1, History Occurrences and Properties*, edited by G. A. Cook *Inter- science, New York, Chap. IX.*, 1961.
- [49] E. Aprile and T. Doke. *Rev. of Mod. Phys.*, 82:2053–2097, 2010.
- [50] Photon Cross Sections Database. <http://www.nist.gov/pml/data/xcom/>.
- [51] E. Aprile et. al. *Phys. Rev. Lett.*, 107:131302, 2011.
- [52] W. Otani. master thesis. *University of Tokyo, Japan*, 1994.
- [53] A.Minamino. master thesis. *University of Tokyo*, 2004.
- [54] M. Ishitsuka. master thesis. *University of Tokyo*, 2001.
- [55] S. Fukuda et. al. *Nucl. Instrum. Meth. A*, 501:418, 2003.
- [56] Y. Takeuchi et. al. *Nucl. Instrum. Meth. A*, 421:334, 1999.
- [57] P. Kotrappa et. al. *Health Phys.*, 46:35, 1981.
- [58] K. Hosokawa et. al. *J. Phys.: Conf. Ser.*, 469:012007, 2013.
- [59] K. Hosokawa et. al. *Prog. Theor. Exp. Phys.*, page 033H01, 2015.
- [60] Y. Onishi. master thesis. *Kobe University*, 2015.
- [61] Inc. Richard B. Firestone, published by John Wiley & Sons. Table of isotopes.
- [62] T. Doke et. al. *Proceedings of the International Workshop on Techniques and Applications of Xenon Detectors (Xenon01)*, 2001.
- [63] E.J. Jeon and Y.D. Kim. *Astropart. Phys.*, 73:28–33, 2016.
- [64] G. L. Fogli et. al. *Phys Rev. D*, 66:053010, 2002.